Durham E-Theses

Mineralogical Limitations for X-Ray Tomography of Crystalline Cumulate Rocks

BRETAGNE, ELOISE,MARIE

How to cite:

Use policy

Mineralogical Limitations for X-Ray Tomography of Crystalline Cumulate Rocks

Eloïse Bretagne

Masters by Research, Earth Science

Supervised by
Dr. Kate Dobson & Dr. Madeleine Humphreys

DECEMBER, 2018

Durham University, Department of Earth Sciences

Abstract

The use of x-ray computed tomography (XRCT) on igneous rocks enables the visualisation and quantification of the 3D texture of the rock and of the crystal population as opposed to a more traditional 2D vision using thin sections and 3D stereological conversions. Although still in its infancy, the application of XRCT on igneous rocks provides a 3D map of the distribution of each mineral phase, the overall dimensional metrology of crystals (size, area volume, shape, orientation and geometry) and potentially their crystallographic orientation. The precision of crystal size distributions (CSD), which are often used for describing rocks and understanding igneous processes, is enhanced by the use of the 3D analysis of crystal size. XRCT shows promising results when applied to volcanic rocks but only limited applications with intrusive igneous rocks

In this study, we compare the dimensional metrology of crystals in 2D and in 3D of a Tugtutoq peridotite sample using a thin section and 3D tomography data to investigate how different the 3D data is from the 2D to test the utility of using XRCT on a dense cumulate. The tomography data is processed in four steps: i) post-processing which includes filtering noise and correcting artefacts linked to the XRCT acquisition; ii) segmentation of the cumulus phase in the sample (in this case olivine); iii) separation of the segmented olivine into realistic and discrete crystals; and iv) the extraction of the data from the 3D-separated olivine crystals (size, location and distribution in the sample, shape, orientation, …).

The results of the tomography scan of the peridotite sample are close to the thin section data but the error associated with the tomography data is difficult to quantify. That error is likely high due to the low contrast in attenuation coefficients between the crystal populations – linked to the similar densities of the mineral phases in the sample – and the close proximity and extensive contact between the olivine crystals. When applied to cumulate rocks, the method cannot be automated to produce reproducible and objective results, but we suggest the application of this method for processing tomography data with either volcanic rocks or cumulates solidified from a more permeable mush, where there is minimal contact between the crystals of interest and the density contrast between phenocrysts and groundmass is high.

Table of contents

List of Figures

11

List of Tables

Declaration

I declare that this thesis, presented for the degree of Master by research in Earth Science at Durham University, is the result of my own original research and has not been previously submitted to Durham University or any other institution.

The copyright of this thesis rests with the author. No quotation from it should be published without the author's prior written consent and information derived from it should be acknowledged.

Acknowledgements

First and foremost, I would like to thank my supervisors Kate and Madeleine for their support in this project. Without them, it obviously could not have happened. I would also like to thank you both for your endless patience explaining concepts and ideas and answering all my questions.

I would also like to give my thanks and friendship to the best bay eva. Katherine, Lena, Pierre-Yves, Jack… I want to thank you for all the support and laughter over the past year and a half. Thanks to all the postgrads around the office for the productive and unproductive chat and tea: Kate, Ilaria, Alex, Olly, Tim, Katy, Chris, Erin, Aimée and Liz. Thanks to the French boys, Simon, Matthieu, Thomas and Guillaume. And thanks to Sean for being patient and supportive through the final stages of this project.

Thanks to my parents who gave me the opportunity to come to Durham and for your unfailing support in all my plans.

1 Introduction

The processes and emplacement environment of igneous rocks can be revealed through the careful study of the visible textures and mineralogy of the solidified product. A cumulate, defined as the product of mineral segregation in a magma chamber, exists as a crystal mush – a mix of melt and crystals – before solidification. Knowledge of the spatial distribution of crystals in a solid or mush state cumulate provides information about the emplacement, transport and source the magma or mush (e.g. Campbell, 1978; Irvine, 1987).

The spatial distribution as well as the size distribution of crystals in a mush provides valuable insight into the connectivity of interstitial liquid (e.g. Marsh, 1988; Cashman & Marsh, 1988, Higgins, 1996), has implications for the rheology, permeability and porosity of the solidifying mush (Blumenfeld *et al.*, 2005). The quantitative observation of textures of crystals has been used to interpret the kinematics of crystallisation (e.g. Lane, 1902; Marsh, 1988), igneous processes such as the arrival of new batches of magma into a chamber (Sparks *et al.*, 1977; Murphy *et al.*, 2000), magma mixing (Couch et al., 2001) and textural coarsening (Cashman & Marsh, 1988; Marsh, 1988, 1998; Armienti *et al.*, 1994; Higgins, 1996, 1998).

Traditional studies of the textures in igneous rocks, using thin sections, provide only a two-dimensional view and are based on the implicit assumption that the thin sections are representative of a whole sample, and in many cases a whole outcrop. However, cumulate textures are three-dimensional and often strongly heterogeneous. The assumption that thin sections are representative is rarely tested, and few authors attempt to quantify the representative elemental volume (REV, Bear, 1972). The inevitable bias of studying 3D textures in 2D (thin sections) is also rarely discussed and, although obtaining 3D data is not trivial, the characterisation of crystal size and cumulate textures in 3D leads to more accurate interpretations of magmatic processes (e.g. Carlson & Denison, 1992, 1997; Holness, 1997).

Many studies are now attempting to use 3D imaging methods (usually X-ray computed micro-tomography) to understand geological microstructures, but this method is not often applied to cumulate rocks (Jerram *et al.*, 2009, 2010; Pankhurst *et al.*, 2014, 2018) where understanding the textures and their distribution is essential to interpreting the underlying magmatic processes. In this

study, we apply x-ray computed micro-tomography (XRCT) to a cumulate olivine peridotite to characterise and quantify the size distribution, spatial distribution and shape of the cumulate olivine in the rock. We develop a robust visualisation and quantification methodology and validate the tomography results by comparing the size, shape and spatial distribution of the olivine crystals in the 3D data to observations obtained from traditional thin sections taken from within the same sample volume.

The aim of comparing the thin section to the tomography data is threefold: i) to evaluate the method for producing the 3D tomography data sets (data processing); ii) to determine the quality and accuracy of the 3D result and iii) to determine the pertinence of using tomography for this sample and for the characterisation of plutonic rocks.

2 Background information

2.1 X-ray Computed Micro-Tomography

Over the last 15 years, X-ray Computed micro-Tomography (usually µCT, XCT or XMT in the literature, XRCT hereafter) has become an accepted three-dimensional visualisation and measurement tool in many areas of science and has transformed into a powerful, high precision metrological tool (Maire & Withers, 2014). The transition from a visualisation technique to a quantitative analysis tool has promoted an increase in image quality, quantity and range of information provided by XRCT.

XRCT is used in a wide range of applications from medicine to material science. It is particularly useful as it allows non-destructive characterisation of micro-textures or pore space. In geology, there are many examples of application of XRCT for studying flow through porous media (e.g. Iassonov *et al.*, 2009; Leu *et al.*, 2014; Wildenschild and Sheppard 2013, Dobson et al 2017). XRCT is also used in volcanology for the quantification and characterisation of bubbles (Hughes *et al.*, 2017) and crystals (Jones *et al.*, 2016) in volcanic materials and is emerging in igneous petrology (Polacci *et al., 2017*). In petrology, it has been used to study the mineralogy and petrography of meteorites (Zolansky *et al.*, 2014), the abundance, shape and size of mineral crystals in ore deposits (e.g. Godel *et al.*,2013; Godel, 2013) and characterising mineralisation micro-textures (*e.g.* Anenburg *et al.*, 2018).

The method shows promise across a much wider range of magmatic and volcanic rocks. Characterisation and analysis of magmatic textures are primarily done on thin sections, which provide information on the spatial distribution of features in two dimensions and are assumed to be representative of whole samples and often outcrops. The use of XRCT on intrusive igneous rocks, including cumulates, enables the visualisation, characterisation and distribution of 3D spatial textures which are often strongly heterogeneous and critical to understanding and interpreting emplacement processes. The quantification of the accuracy of XRCT has seen limited study on porous media (Kerckhofs *et al.*, 2008) but the limitations and capabilities of the method on igneous samples are however untested.

2.2 Understanding and interpreting textures in cumulate rocks

In this section, the methods for quantitatively describing the texture of the rock are introduced. Size and spatial distributions of crystals in a volume are commonly used to interpret the kinematic evolution

of the olivine crystals in the peridotite. In this study, we were not able to interpret the distribution data but use it as a tool to visualise and compare 2D and 3D data. Working with 2D data obtained from thin section does not completely represent natural samples, but corrections can be applied to simulate 3D data.

2.2.1   Crystal Size Distributions

CSD theory was developed in the 1960s to predict crystallisation processes in industrial materials (Randolph and Larson, 1971). The first application to geology was used to estimate crystal nucleation and growth rate in various magmatic and metamorphic settings (Cashman, 1988; Marsh, 1988a; Cashman and Marsh, 1988; Cashman and Ferry, 1988). Crystal size distributions (CSDs) quantitatively describe the cumulate texture using a single parameter: crystal length, size or area. The shape of CSD plots provides information about the growth rate of crystals in precipitating solutions (Wagner, 1961; Baronnet; 1982; Eberl *et al.*, 1988).

Examination of final textures in the solidified rock provides information about its cooling and crystallisation history, but a CSD approach is sensitive to records of intermediate textures that help elucidate the history of the rock (Higgins & Roberge, 2003). CSDs can, therefore, provide information on residence time of a magma in a volcanic conduit (Mangan, 1990) and identify mixing and contamination events in a magma chamber (Marsh, 1988; Jerram *et al.*, 2003).

Spatial and temporal changes in magmatic processes can be identified when CSDs measured for a suite of related samples are compared (using the same physical parameter). Some parameters, however, are thought to be more sensitive to different parts of the evolution: e.g. crystal size is more representative of the latest stages of crystallisation (Armienti *et al.*, 1994a, b; Taddeucci *et al.*, 2004).

Eberl (1998) suggests three basic CSD curves to describe different crystal growth processes (Figure 1). CSDs are plotted as crystal size against the natural logarithm of the number of crystals per size interval. An upward concave CSD curve relates to crystal nucleation and growth at a constant nucleation rate (Figure 1, A) and has been attributed to crystal accumulation processes mixing of crystal populations (Spillar & Dolejs, 2015); a log-normal distribution relates to a continuous nucleation and growth mechanism assuming nucleation at a decaying rate in either a closed or open system showing the

increase in crystal nucleation as the magma cools (Marsh, 1998; Figure 1, B) and a negatively skewed distribution describes crystal coarsening, such as Ostwald ripening (Figure 1, C). Curving or kinking of log-normal CSDs can be attributed to the coexistence of more than one mineral phase, accumulation or removal of crystals during crystallisation (Higgins, 1994; Marsh, 1996; Hepworth *et al.*, 2018). Physical compaction of the crystal pile will also register on a CSD (Higgins, 2002b; Boormann *et al.*, 2004).
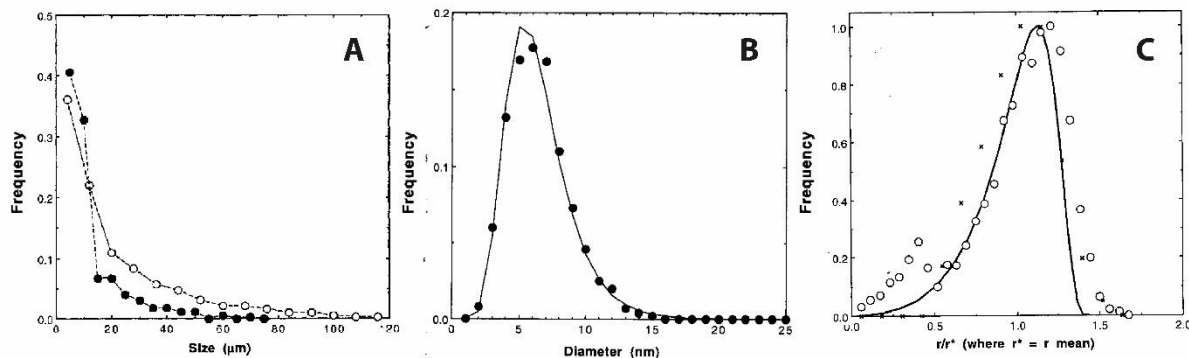
Figure 1— Graphical overview of the three CSD curve types. A: negative asymptotic curve showing crystal nucleation and growth with a constant nucleation rate; B: log-normal distribution expressing continuous nucleation and growth assuming a decaying nucleation rate; C: negative skewness relates to Ostwald ripening. Modified from Eberl (1998).

When crystal growth rate is assumed to be constant in an open magmatic system, the CSD graph can be used to calculate crystal nucleation and growth rates (e.g. Marsh 1988, Higgins, 2000). The slope of the CSD (**Error! Reference source not found.**) is used to calculate crystal growth rates with the following equation:

$$S = -\frac{1}{G\,\tau}$$

Where S is the slope of the crystal distribution and G is the growth rate and τ is time. The nucleation rate I is calculated using

$$y_0 = \frac{I}{G}$$

Where y_0 is the intercept with the y axis (see **Error! Reference source not found.**).

Assuming constant growth rate, data set B would be interpreted as having a highest nucleation rate (due to the position of the y intercept) but the slowest growth rate (growth rate being inversely proportional to slope). Data sets A or D have the gentlest slope, so are interpreted as having the highest growth rate.
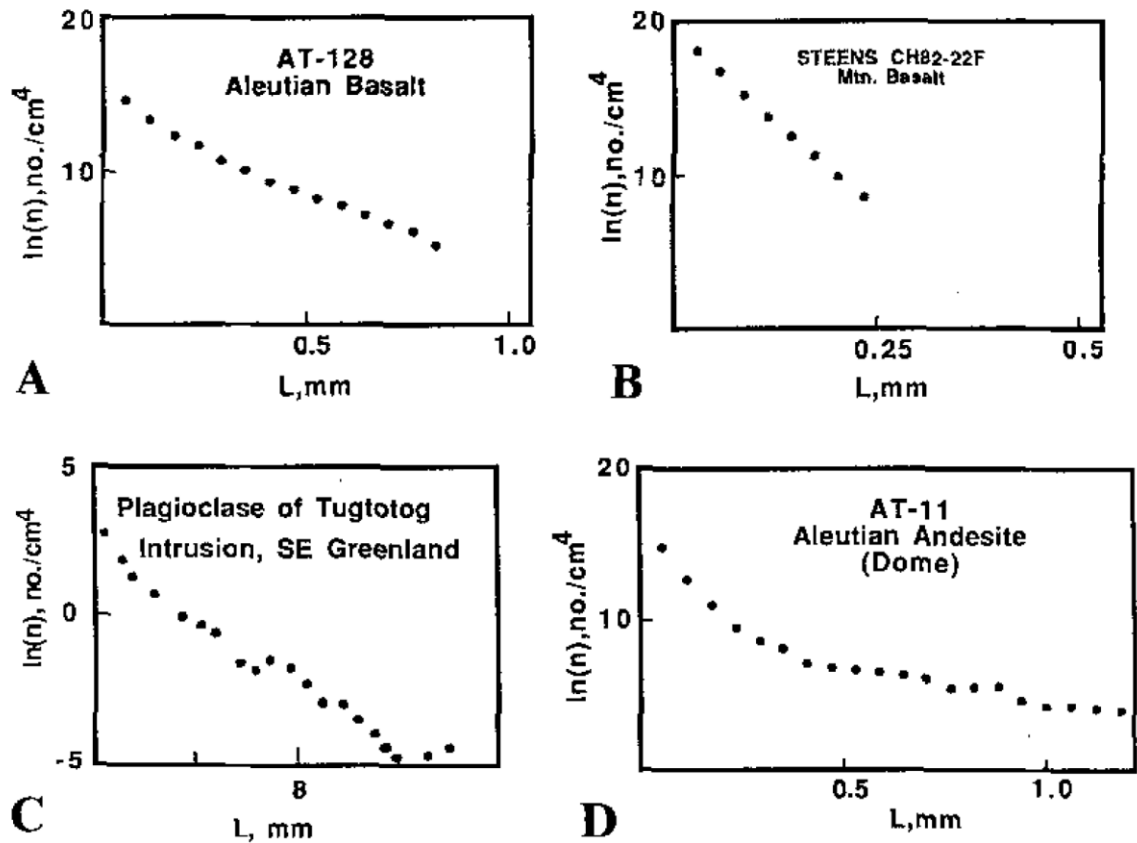
Figure 2— Example of size distributions from Mars, 1988. The slope of each data set is calculated and relates to the growth rate. The intercept of the slope reflects the nucleation rate.

The data are plotted as a histogram from crystal size data. Traditional CSDs are plotted as the size of the bins against the natural logarithm of crystal population density (ln (population density), e.g. Higgins, 2000). It is expressed as the number of crystals per size category divided by the volume of the sample, with units of $1/m^4$ (Marsh, 1988). The size bins of the histogram are sometimes non-linear: the maximum crystal size is chosen as the largest size bin, then the natural logarithm of that value is taken to produce the next smallest size bin, and so on, until the smallest size is reached, which correspond to the resolution of the data (e.g. Higgins, 2000).

In this study however, we simply use the frequency of crystals per size bin, as the 2D and 3D samples compared here have the same area and volume, respectively. The size bins on the x-axis are also linear. We chose to simplify the CSD thus because we primarily use CSDs to visualise and compare data. Therefore, we did not construct traditional CSDs as seen in published literature as we are not interpreting them in terms of crystal growth kinematics.

2.2.2 Conversion of 2D data to 3D

Obtaining accurate quantification of the size of a crystal population is not trivial (Morgan & Jerram, 2006). The crystal size is quantifiable from 2D observations (thin section). This measurement, however, represents the intersection grain size and not the true size of the 3D crystals. It is preferable to obtain the true size of the particles as they are a truer constrain on the interpretation of crystal growth kinematics, but such data are often hard to produce, especially for igneous rocks as each individual crystal would need to be separated without being broken. (e.g. Holness, 1997; Carlson & Denison, 1992, 1997, Higgins, 2000). There exist a number of proposed conversions that enable users to generate 3D data from 2D observations (e.g. Sahagian & Proussevitch, 1998; Higgins, 2000; Farr *et al.*, 2017).

Sahagian and Proussevitch (1998) suggest a formulation to generate 3D size distributions from 2D data based on the probability of distribution of the particle intersection size. The conversion was produced for bubbles, thus modelling spheres, but the formulation is applicable to almost any shape. Applying stereological principles, when a 2D plane (for example a thin section) cuts a population of spheres, they will not be systematically intersected through their centre. A probability distribution of intersecting any given sphere through its centre can be calculated analytically from the "apparent" size of the particles in the 2D plane. Applied on a unimodal population of spheres, the expected 3D size distribution can be calculated, provided the assumption that the largest "apparent" cross-section is the actual diameter of the largest sphere in the population holds true. Recalling that a polymodal population of spheres is the superposition of several unimodal systems and that the probability distribution for a sphere is known, the polymodal distribution of spheres can be divided into discreet unimodal systems and the formulation is applied iteratively to each system. This stereological conversion method can be applied to non-spherical populations because the size distribution does not depend on the particles shape, but on particle aspect ratios (Sahagian and Proussevitch, 1998). As long as the aspect ratios are similar across the population (shapes and size can vary), the stereological formulations can be applied. Thus, the formulation does not require prior knowledge of the size distribution, which, if required, can limit the use of the conversion method on bimodal distributions or complex natural distributions.

Other methods for projecting 2D size distributions into 3D include the "CSDcorrections" software developed by Higgins (2000). This also uses the 2D size distribution to generate the 3D CSD; but takes

into account information on crystal habit, roundness and the presence of foliation in the sample to perform the stereological correction.

An alternative procedure can be applied directly to the average size of particles (Farr *et al.*, 2017). The authors suggest using a moment-based particle size characterisation as a simple way of describing a population of sub-spherical to spherical particles. By multiplying the mean of the 2D size distribution by a correction factor – the value of which depends on the moment chosen and best suited for the problem – the exact mean of the 3D size population can be calculated. This however only provides one mean value to describe the size distribution of the particles and limits the interpretation of the magmatic history of the sample.

In this study, we use a numerical code produced by Dr D. Neave (Hughes *et al.*, 2017), based on the works of Sahagian and Proussevitch (1998). Conversion methods often necessitate an a priori on shape and size and can be limited to a certain size range (Taddeucci *et al.*, 2004), which could affect their accuracy. As it is not the case with the code from Hughes *et al.* (2017), as well as its simplicity prompted us to use it.

2.2.3   Mush structure

The spatial distribution of crystals in a mush reveals a lot of information about the rheology and architecture of a crystal mush (Rudge *et al.*, 2008). The quantification of the spatial distribution of component crystals is used to describe and compare different types of crystal mush.

Point pattern statistics of grain centre location are used to describe spatial structures and textures, usually on 2D data (e.g. Kretz, 1966, 1969, 2006; Carlson, 1989; Jerram *et al.*, 1996), with only a limited number of studies quantifying spatial structures in 3D (Hirsch *et al.,* 2000; Ketcham *et al.*, 2005). Point pattern analysis is a mathematical way of expressing the spatial arrangements of points in space to evaluate if a spatial distribution is random or the result of a process (Cressie and Wikle, 2011). Here we apply point patterns to determine the packing structure as well as the clustering or ordering of crystals in a mush, and the variability between the different datasets.

Ripley's K function and the pair correlation function are statistical functions that evaluate the spatial distribution of particles and quantify the packing of particles or of crystals in a mush (Stoyan and Stoyan,

1996). Ripley's K function is expressed as the expectation (E) of finding a certain number of particles within a circle of radius (r) divided by the intensity of the system (λ), the area density of the particles (Diggle, 1983; Stoyan, Kendall and Mecke, 1987).

$$K(r) = \frac{E}{\lambda}; \qquad \text{for complete randomness, } K(r) = \pi\, r^2$$

The transformed version of Ripley's K function, Ripley's L function, is often more convenient

$$L(r) = \sqrt{\frac{K(r)}{\pi}} \; ; \text{and for complete randomness, } L(r) = r.$$

Ripley's L function has a slope of 1 for complete randomness. The curve is above the slope = 1 for clustering and below for ordering of the particles (Figure 3, 1st column).
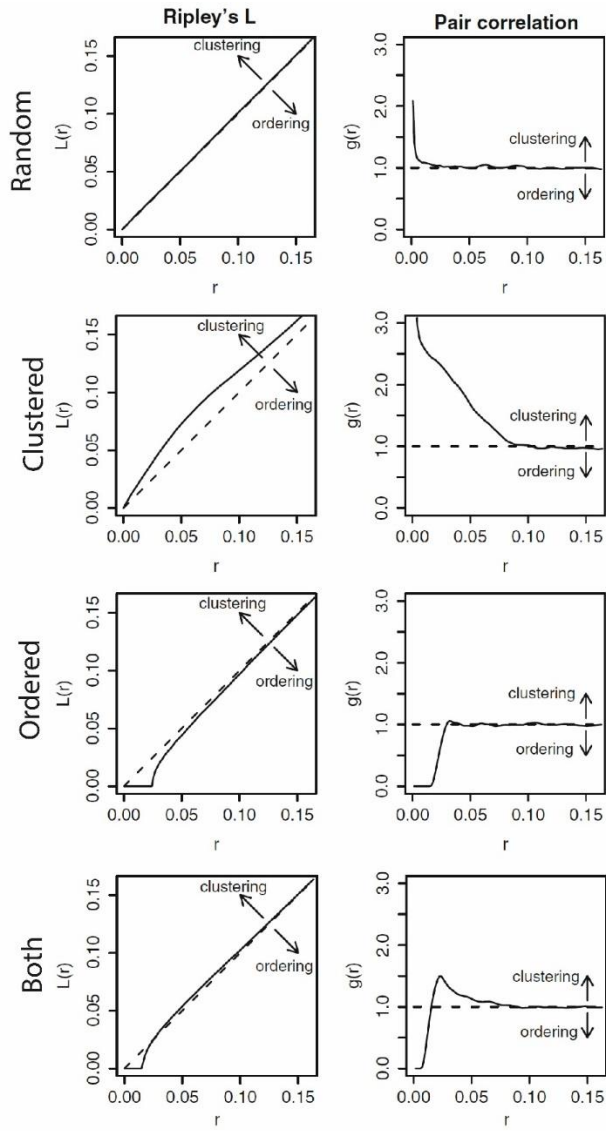
Figure 3— Four examples of L(r) and PCF for a random spatial distribution, clustering, ordering and locally clustered or ordered of particles. The dashed line represents spatial randomness. Figure modified from Rudge et al. (2008).

The pair correlation function operates in the same way as the K function but whereas Ripley's K function calculates a distribution function, the pair correlation calculates the probability of that distribution, representing the statistical probability of finding particles at distance r from any other particle (Finney *et al.*, 1994; Stoyan and Stoyan, 1996). The pair correlation function g(r) is defined by

$$g(r) = \frac{1}{2\pi r} \frac{dK(r)}{dr} \text{ ; where for complete spatial randomness, } g(r) = 1$$

The pair correlation function, like K(r), is defined by drawing a circle of radius r on a particle but instead of counting the number of particles inside the circle like Ripley's K function, the PCF draws two concentric circles and counts only the particles falling inside the ring defined by the two circles (Figure 4; Baddeley *et al.*, 2015). Graphically, both functions show if the particles in the sample are ordered, clustered or correspond to complete spatial randomness (Figure 3). The pair correlation function, g(r)=1

for complete spatial randomness. The function is above g(r) = 1 for clustering and below for ordering of the particles (Figure 3, 2nd column).

The pair correlation function graph also gives information about the length scale dimensions of potential clusters of particles. Figure 4 shows a typical example of a PCF of a particle population (Finney *et al.*, 1994). For small values of r, the PCF is zero as there is no probability of finding another particle as close as at least twice the radius of the particle for a monodisperse population of particles (cf. Figure 4, sketch of particle population on the bottom). The function then increases rapidly to reach a clear peak. The slope of g(r) before intersecting the spatial randomness line (defined as g(r) = 1) will depend on the polydispersity of the sample (Lochmann *et al.*, 2006; Figure 4, box 1): if the particles are a monodisperse distribution, the slope will be very steep (as in Figure 4), while the slope will be flatter for a polydisperse population (Stoyan & Stoyan, 1994; Lochmann *et al.*, 2006). The lateral width of the slope (purple line, 2) represents the hardcore of the distribution, the biggest physical distance between the centre of two non-inter-penetrable particles (e.g. crystals) where g(r) = 0 (Stoyan & Stoyan, 1994; Lochmann *et al.*, 2006). A true hard core reflects the minimum distance between particles but is only truly present for monodisperse populations of particles (Finney *et al.*, 1994).

The height and width of the peak (Figure 4, box 3) reflect the significance of clustering in the particle population (Finney *et al.*, 1994), where the width of the peak relates to the variation of the distance between particles. The higher and narrower the peak, the less distance there is between the particles, therefore, the stronger and more clustered the sample is. The peak is smeared and becomes wider for polydisperse particle populations as the characteristic distance to the nearest particle becomes a range of values as opposed to a single value for a monodisperse population. For polydisperse populations, the width of the peak is also influenced by the number of particles and will become wider the more particles there are as more different sizes are sampled. The location of the peak, which is related to the average distance between two particles (Finney *et al.*, 1994; Lochmann *et al.*, 2006) will also reflect a single value for monodisperse populations and a range of values for a polydisperse population.

After the peak, the PCF continues with an undulating tail that tends to g(r) = 1 at large r. The distance over which the tail undulates reflects the size of the clusters, and the position and amplitude of the undulations can indicate the presence of less frequent clusters.

Using PCFs on 3D data would improve the accuracy of the result, solving the implicit assumptions of 2D data. The volume used for the 3D data shows the spatial distribution of the features in question and the 3D data set is larger, therefore more accurate (Mock & Jerram, 2005).
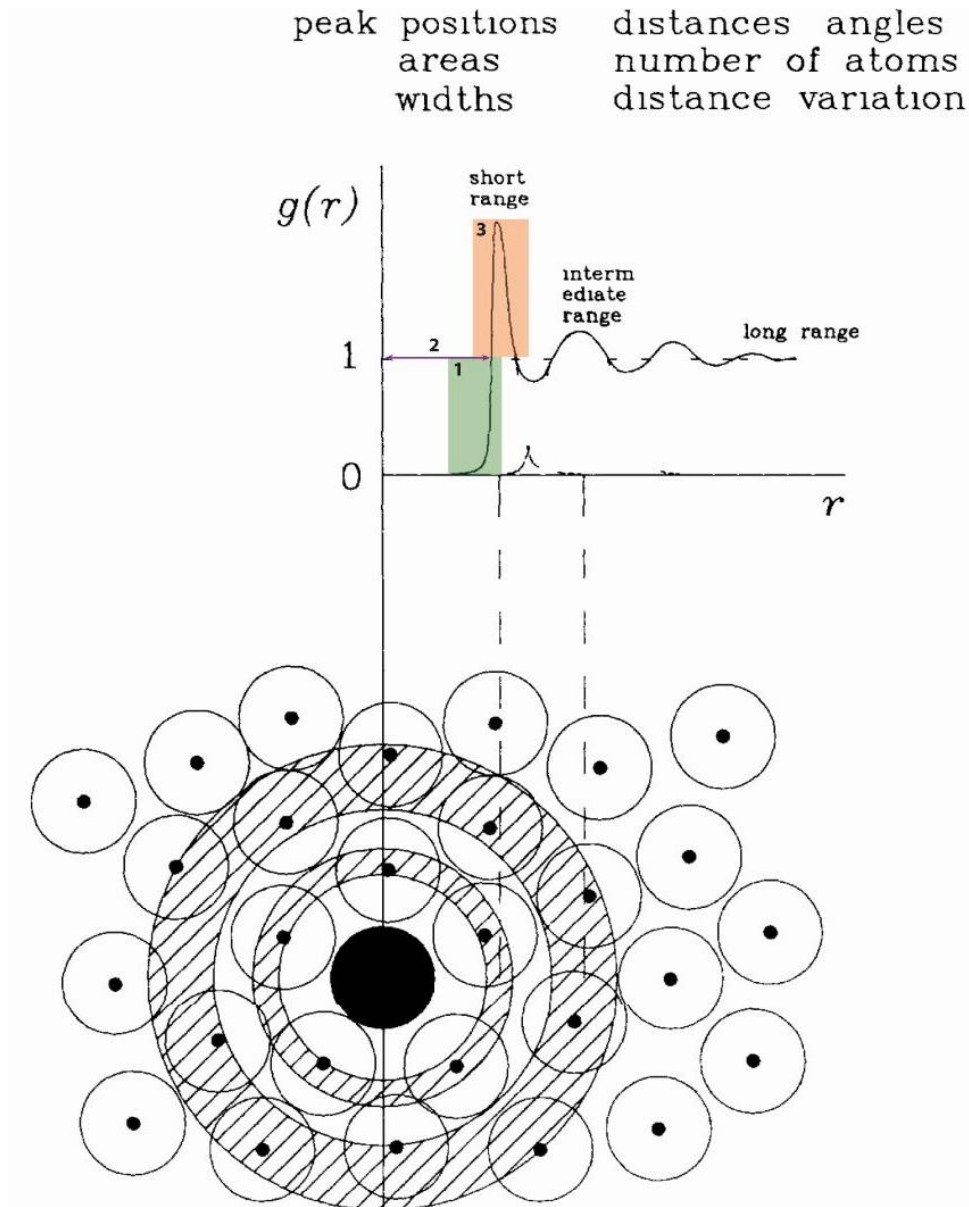
Figure 4— *Typical example of a PCF of a randomly packed particle population from the literature. The dashed line g(r) = 1 represents total spatial randomness; the green box (1) highlights the slope of g(r) below g(r) = 1; the purple line (2) highlights the hardcore effect and the orange box (3) highlights the peak of the PCF. Modified from Lochmann et al., (2006)*

2.2.4   What is the benefit of XRCT on these methods?

Traditional textural studies of igneous rocks are performed using thin sections, a 2D slice through a 3D object. Users need to assume that the thin section is representative of the 3D texture of the sample. However, igneous textures are often heterogeneous. Therefore, we suggest a 3D approach to textural analysis as a solution to the loss of the third dimension.

Using 3D data presents many advantages: three dimensional, spatially heterogeneous textures of igneous rocks are explored properly in 3D, taking into account their spatial distribution in the sample which effectively removes the assumptions made necessary by the use of thin sections.

The 3D nature of the data means that many more crystals are considered in the textural analysis, which increases the quality of statistics on metrics such as grain size, shape or volume. The larger number of grains also increases the quality of CSDs allowing for a better understanding of crystal growth kinematic in the magma reservoir.

The metrics of size, area, volume and shape performed on a 3D volume of the sample yield the true values for size, etc whereas a 2D vision only provides an intersection value where the volume of rock is cut to produce the thin section. This also contributes to a better understanding of cumulate processes in the magma reservoirs.

2.3   Samples for a quantitative assessment of X-ray computed micro-Tomography

The samples used in this study are cumulus crystalline igneous rocks from gabbroic intrusions. One sample is from the Younger Giant Dyke Complex in South Greenland. Other samples considered for this study are from the layered mafic intrusion of Rum, an island of the Inner Hebrides, Scotland.

2.3.1   Tugtutôq, South Greenland

Sample GAR 231 is from South Greenland and was collected by Dr M. Humphreys (2013). The sample is from Tugtutôq, part of the Gardar igneous province. Manifestations of magmatism along the Tugtutôq-Narssarssuaq zone are represented by giant dykes that can be followed for up to a hundred kilometres in the landscape (Upton, 1964a; Emeleus & Upton, 1976; Upton & Blundell, 1978). The dykes can reach up to 8 km across and show internal synform-shaped layered structures (Upton & Thomas, 1980). The

giant dykes of Tugtutôq are derived from olivine-basalt magmas, and after undergoing differentiation, are the source of alkaline rock complexes of the area (Upton & Thomas, 1980).

The sample comes from the Younger Giant Dyke Complex (YGDC) (Emeleus & Upton, 1976), which has a broad compositional range and contains internal structures (Upton & Thomas, 1980). It was emplaced circa 1163 Ma ago (Upton, 1964a, 1987). One of the features of this gabbroic complex is the 'Troll's Mouth', composed of crescent-shaped peridotite bodies that can reach 10 meters in length and 3 meters in height embedded in pale troctolites (Upton, 2013, Figure 5). The peridotite bodies exhibit crude columnar jointing normal to the dyke wall, hence the name (Figure 5, 1).
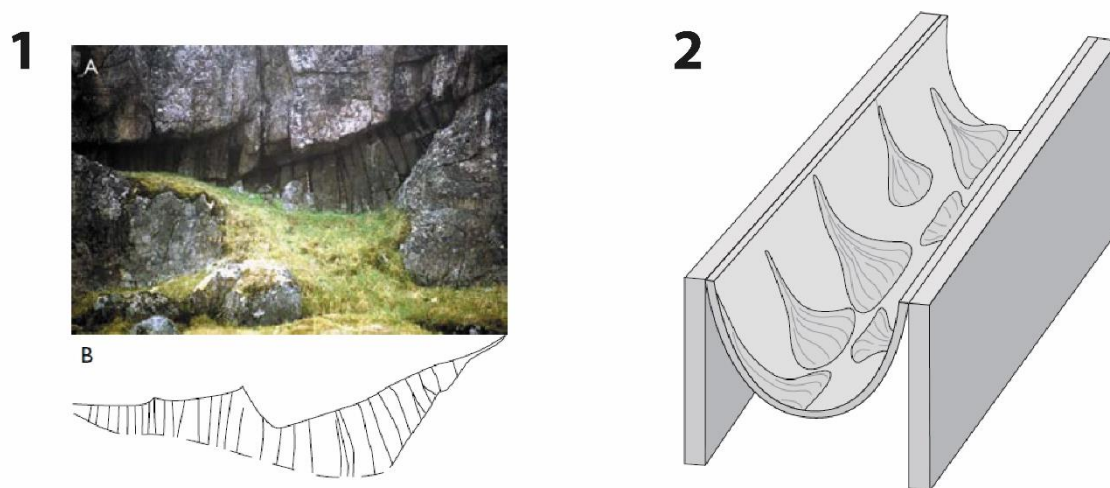
Figure 5— 1: lenticular-section of a peridotite abruptly defined from the above and underlying troctolite, known as the "troll's mouth". The sketch below highlights the characteristic jointing transverse to the cooling surfaces. 2: schematic model of the localised sedimentary fans of peridotite descending along the sides of the dyke walls. After Upton (2013)

The peridotite units are interpreted as cross sections of fan-like olivine-rich slurries that flow down the internal walls of the dyke (Figure 5, 2), in structures analogous to sedimentary alluvial fans. GAR 231 is from one of these peridotite bodies, and so the sample has a well-constrained emplacement history, and there is little post-emplacement modification to the structure of the mush.

2.3.2 Layered mafic intrusion of Rum, Scotland

The Isle of Rum, Inner Hebrides, Scotland is part of the British and Irish Tertiary Volcanic Province (Emeleus and Gyopari, 1992; Bell & Williamson, 2002), and exposes an exceptionally well-preserved ultra-mafic to mafic layered intrusion. The layers complex has been dated to 60 Ma (Hamilton *et al.*,

1998) and is part of the magmatism associated with the impingement of the proto- Icelandic plume during the Paleogene (Kent, 1995; Saunders *et al.*, 1997; Bell and Williamson, 2002).

The layered series was formed by the successive intrusion of multiple sills of ultramafic and mafic composition (Emeleus, 1997). The mafic complex is divided into Eastern, Central and Western regions. Samples considered for this study are from the Eastern Layered Intrusion (ELI), a 750-meter thick succession of olivine cumulates interspersed by troctolitic and gabbroic units formed by numerous small intrusions of picritic or basaltic magma (Renner and Palacz, 1987; Holness *et al.*, 2007; Holness and Winpenny, 2009; Hepworth *et al.*, 2017, 2018).

At the interface of some layers, the contact between gabbro and peridotite is characterised by a "wavy horizon" (Holness *et al.*, 2007). It is the expression of the reactive front at the contact of gabbro with hot picritic mush (Holness *et al.*, 2007; Holness and Winpenny, 2009; Leuthold *et al.*, 2014; Hepworth *et al.*, 2017, 2018).

A better understanding of the 3D mush textures in these rocks would allow us to see how the chemical reaction (magma mixing) is controlled by the mush permeability. Samples were therefore collected on either side of a "wavy horizon" (Figure 6) to test this hypothesis using XRCT to study the structure of the initial mushes.
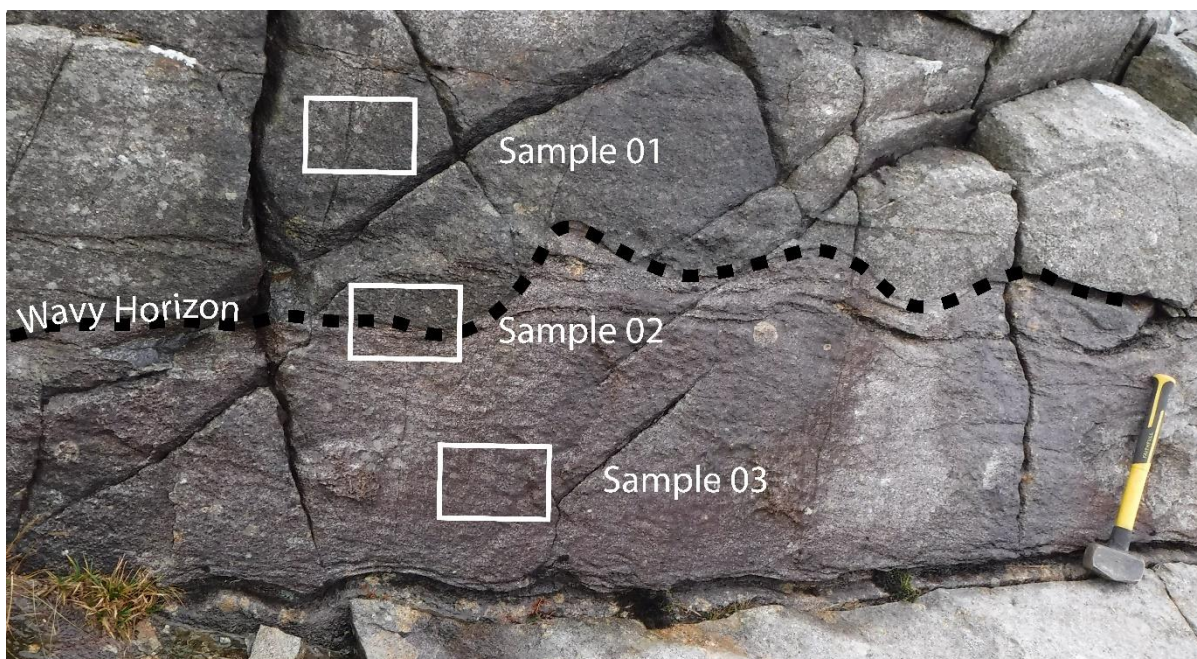
Figure 6— Visualisation of sampling across the Wavy horizon in the ELI. The dashed line highlights the reaction front. Below that is the reacted material and above is the non-reactive

3   Methodology

The following section presents a robust methodology for assessing cumulate igneous textures in 3D x-ray tomography (XRCT) datasets. This chapter presents the image processing methodology and the methods and approaches used to compare data of different image modalities, resolutions and dimensions. Qualitative and quantitative assessments of how well the 2D thin section analysis and 3D tomography-based image analysis describe the textures are presented, compared and interpreted in subsequent chapters. The Younger Giant Dyke Complex sample from Tugtutôq shows the simplest mineralogy and texture, with a single (olivine) cumulate phase, and is the focus of the following chapters.

Defining a robust post-acquisition processing protocol for determining mush spatial distribution from 3D images, and the subsequent comparison of the 3D analysis to the traditional 2D with stereological correction methods represents the bulk of this study.

3.1   Materials

The Younger Giant Dyke Complex sample from Tugtutôq has the simplest mineralogy and texture (a single cumulate phase, olivine and the occasional plagioclase cumulate crystal) and has the best constrained emplacement history. This sample is therefore used for the method development and comparative analysis. We concentrate on the cumulus phases to better understand the crystal mush. All samples are composed of olivine, plagioclase and clinopyroxene in varying proportions.

3.2   Data generation

3.2.1   X-ray Computed Tomography (XRCT) acquisition

X-ray Computed Tomography is a non-destructive 3D imaging technique that produces a high-resolution 3D image of an object. An x-ray beam is fired at a rotating sample and is progressively attenuated as the x-rays travel through the minerals, where the attenuation rate is a function of the properties of the mineral (chemical composition, density, …) and x-ray energy. After exiting the sample, the attenuated beam hits a scintillator where the x-rays are converted into photons and captured as an image on a detector. Hundreds or thousands of images (projections) are collected over a 360 rotation and all are used to reconstruct a 3D greyscale volume, where the greyscale value of each voxel (3D equivalent of a

pixel) represents the mean attenuation of the corresponding volume of the sample, which in geological samples is closely related to the density, and in turn the mineralogy (Ketcham and Carlson, 2001).

The attenuation of a mineral phase can be calculated from the NIST database[1], and the x-ray energy used for the scan can be optimised for the mineralogy of the sample. For the Tugtutôq peridotite, this means that to distinguish clinopyroxene from olivine, the image is collected with a narrow range of energies (35 to 70 kV) over which the attenuation coefficients are the most different (dashed box, Figure 7). In some cases, it is possible in some samples to determine olivine composition directly from the greyscale and to observe zonation in the individual crystals (Pankhurst *et al.,*2018).
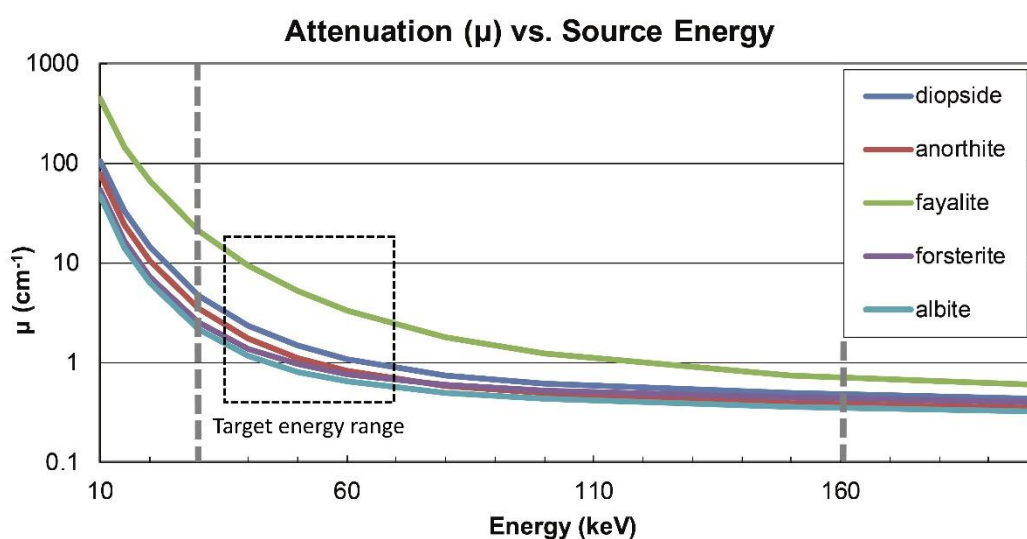
Figure 7— X-ray attenuation coefficient for rock-forming minerals in the Tugtutôq peridotite. The higher the energies, the closer the curves are, the less distinguishable the signals will be for the different minerals. To distinguish all the minerals in the tomography greyscale result, the scan needs to be performed at low energies. The XRadia Zeiss VersaXRM 410 x-ray tomography scanner uses energies ranging 30 to 160 keV (grey dashed lines). Source: MUCALCTOOL, UTCT (Hanna & Ketcham, 2017).

In this study a 1.5 cm diameter drill core was imaged using the XRadia Zeiss VersaXRM 410 x-ray tomography scanner at Durham University. The scan was acquired at a maximum accelerating voltage of 70 kV, at 10W. No additional filtration of the beam was applied to maximise the flux of low energy x-rays. 3201 projections were collected, with a 20-second exposure. No pixel binning was applied. Projection data were reconstructed using the proprietary Xradia filter back projection algorithms, giving a voxel resolution of 11.9 microns (voxel edge length). Despite beam optimisation and long scanning

---

[1] The spreadsheet used to generate the attenuation coefficient graph is available here:
http://www.ctlab.geo.utexas.edu/software/mucalctool/

times, the high overall attenuation and variable nature of the sample mean that while the mineral

phases are distinguishable in the reconstructed data set, subtle variations in composition are not.

3.2.2   Thin section preparation and data acquisition

After XRCT scanning, two thin sections were made from the peridotite drill core. These were cut parallel

to the rotation axis (Figure 8). The thin sections were scanned at high resolution on a slide scanner and

each olivine crystal identified (see Section 3.3.5)
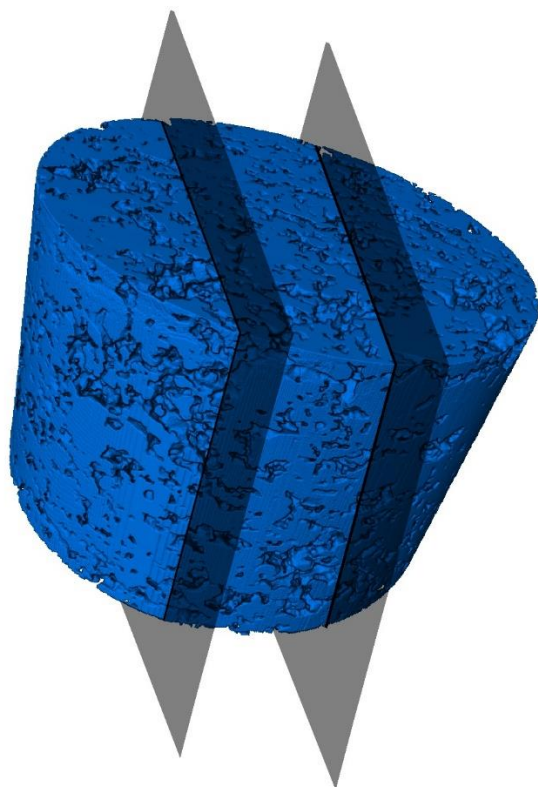
Figure 8— Sketch of general emplacement of the thin sections in the peridotite drill core sample. They are both parallel to the rotation axis of the XRCT acquisition.

3.3   Tomography Data treatment

Image processing – the steps between data acquisition and quantitative data interpretation – is

separated in four steps: i) post-processing for image noise reduction and to remove acquisition

artefacts, ii) segmentation – the labelling of each voxel as belonging to a particular object class or not,

in this case labelling as a mineral phase iii) separation – to "break up" all the voxels labelled as olivine

into individual grains, and iv) extraction of the quantitative measurements. Each step can be complex

and requires a number of user-made decisions, even when the user is applying automated image

analysis algorithms. The overall workflow for the processing showing all the major stages is shown in

Figure 9, with further details provided below. All processing presented here is performed using the ThermoFisher-FEI package Avizo™.
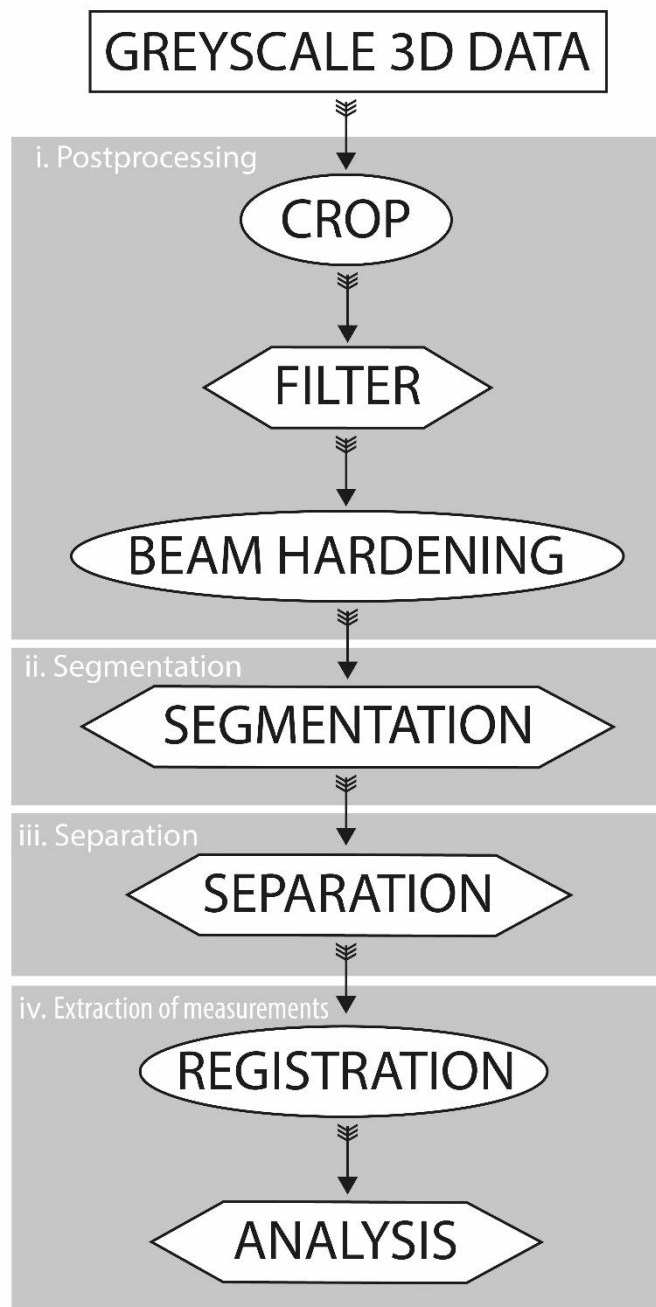
Figure 9— Basic structure of general workflow. Details about the different steps will be added to the figure through the methods chapter. Rectangular boxes signify a data set, oval shapes mean the application of an in-built function in Avizo™ and the hexagonal boxes represent decision points. The user has to visually judge the quality of the result before moving to the next step.

3.3.1 Terminology

In the XRCT literature, a range of terminology is used to describe the multiple components of processing or visualisation. Before going into the detail of data treatment, a short introduction to the terminology is provided.

Slice – A slice is any 2D plane placed through the 3D data volume. It is often used to define the horizontal plane (perpendicular to rotation) in reference to the way synchrotron CT datasets are reconstructed, but here, using 3D laboratory data we use *Slice* to mean a 2D plane cut through the 3D data in the orientation given, and *tomography slice* to mean the slice through the x-ray data that corresponds to the thin section.

Stack – this term is often given to a series of sequential horizontal (perpendicular to rotation) slices, which is more accurately a sub-volume of the 3D data. Here we use the term *tomography stack* to describe a 3D render of the grains in the *tomography slice* i.e. a 3D render of the grains equivalent to those in the thin section.

Volume – A volume is any 3D object. Here we use *3D volume* to mean the full x-ray data of the core.

Labelled data – Labelled data is a data set that has been evaluated for its attributes. It is the result of a segmentation and can be a binary data set (has the attribute = 1, does not have the attribute = 0). If the particles in the data have been analysed for additional volume or shape parameters, then the Labelled data can be represented as a non-binary data, showing the particle index value or any other measured parameter as the value attributed to each particle.

Avizo™ contains a large number of algorithms and commands that can be used to treat image data. The majority of these are generic processes or have been incorporated from the literature and are referenced within the package. In the subsequent workflow, specific algorithms or module names are provided (and associated references where applicable), as are the parameters or conditions which are used in that application. They are in the following format

module name <parameters>

together with a brief description of the actions or process being applied and the reasoning behind the choices made. This information is critical. Without it, it is impossible for anyone to reproduce the data analysis.

3.3.2 Post-processing

Post-processing describes the steps taken between acquiring the raw greyscale volume and the start of extracting the data. It usually involves steps to extract a volume of interest (if applicable) and filtration to reduce image noise.

The top and bottom of the sample cylinder are different in colour than the rest of the sample. This is explained by a combination of two artefacts of the tomography acquisition due to the geometry of the beam, known as the "cone beam effect". The x-rays are emitted from a point source and travel from source to detector in a conical beam. This means that a higher flux of x-rays is hitting the detector in the centre (directly behind the sample) than at the edges (Figure 10, x-ray flux gradient on detector). This effect is corrected automatically by the scanner, by taking a "flat field" image of the beam without the sample and using the x-ray flux distribution to correct the image data.

The second effect of the beam geometry is caused by the incident angle of the x-rays, where the edges of the sample are being traversed by x-rays at all viewing angles (Figure 10, grey corners of the sample). X-rays passing through the top and bottom corners of the sample closest to the source will not hit the detector, so this part of the sample is under-sampled. The data can be usable but would require different data treatment protocols as the greyscale values will be different, and so these regions are cropped from the processed volume.
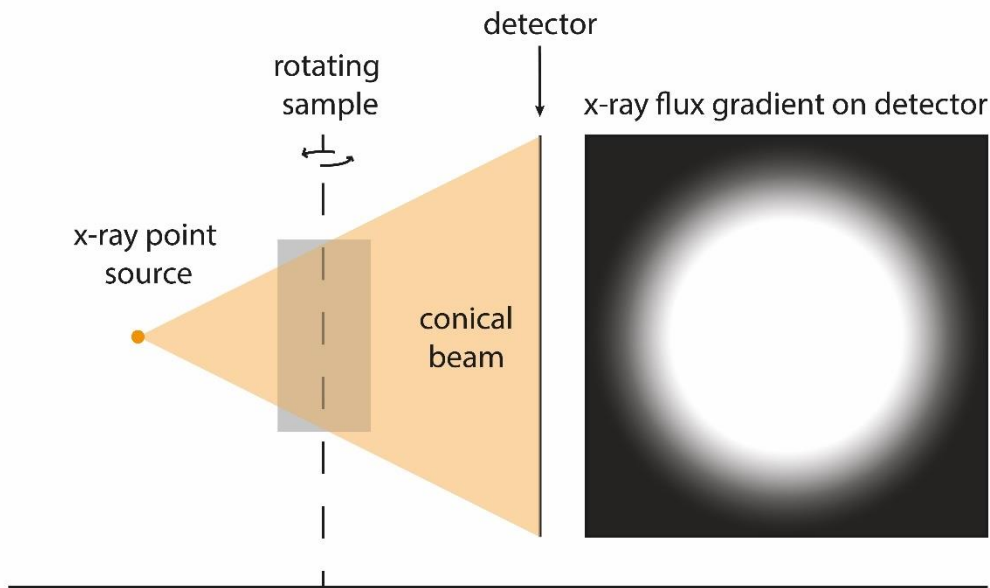
Figure 10— Sketch explaining cone beam effect and the subsequent x-ray flux gradient on the detector. The gradient on the detector illustrates the distribution of rays on the detector, the centre receives more rays than the edges. The second effect of the conical beam is the lack of x-rays on the detector for the top and bottom parts closer to the source (see grey edges of the sample, they are not traversed by the beam of x-rays captured on the detector).

Tomography images are generally noisy. To improve contrast between close linear attenuation coefficients of the rock-forming mineral, a low energy beam is needed. This lowers the overall flux and reduces the signal to noise ratio. Other potential sources of noise are fluctuations in the x-rays beam during scanning, non-linear pixel behaviour on the detector and x-ray scattering from the sample. Noise is usually manifested as discreet erroneous voxel values or clusters of voxels with erroneous voxel intensities.

A further source of uncertainty in XRCT data is the blurring and diffusion of phase boundaries. This is caused by the "partial volume effect". A voxel represents the reconstructed bulk attenuation value of the volume it describes. At a perfect planar phase boundary, the bulk value of the voxel will be made up from both materials in proportion to the volume fraction, unless the phase boundary and the voxel boundary are perfectly overlain. In geological samples, planar interfaces are not always planar. Grains may be smaller than a voxel or contain inclusions, fractures or other features that lead to a lower bulk density thus a different voxel intensity value (Ketcham & Carlson, 2001). The effect leads to blurring of the edges and leaves a gradient in greyscale across discrete phase boundaries.

Noise reduction in tomography data is achieved using filters, which smooth the greyscale data. As the aim of this study is to develop a workable processing workflow, filter selection was limited to those implemented in Avizo™. All were tested and a limited parameter sweep through each algorithm was conducted, with varying results.

Bilateral

Box

Gaussian

Median

Recursive exponential

Delineate

Unsharp masking

FFT Filter

Anisotropic diffusion

Non-local means

Of all the Avizo™ filters tested, the best result was produced by the *Anisotropic diffusion* filter and the *Non-local means* filter. The other filters either caused too much smoothing of grain boundaries or did not help reduce the discrete noise.

Anisotropic Diffusion is a popular and widely applied image enhancing algorithm filter commonly used for denoising scalar volume data (Wildenschild and Sheppard, 2013). It characteristically enhances contrasts and preserves strong edges. The filter works by reassigning the greyscale value of each voxel by comparing the value of the current voxel to its 6 neighbours. If the difference does not exceed the diffusion stop criterion (set manually, see parameters), there is diffusion. If the criterion is set to zero, there is no diffusion and the greyscale values remain the same. Diffusion is allowed to continue for a user-defined number of iterations (the diffusion time) which will impact the resolution of the filtered image. High numbers of steps with a low diffusion stop criterion will smooth areas of near equal intensity while leaving boundaries unchanged while a too long diffusion time will result in a blurry image (Perona & Malik, 1990).

Testing showed the best parameters for *Anisotropic Diffusion* are using a threshold at 5000 and 15 iterations when applied in 3D. The result is good, but the image retains some of its grainy texture and is blurry (Figure 11).

Anisotropic diffusion < 3D settings, threshold at 5000, 15 iterations>
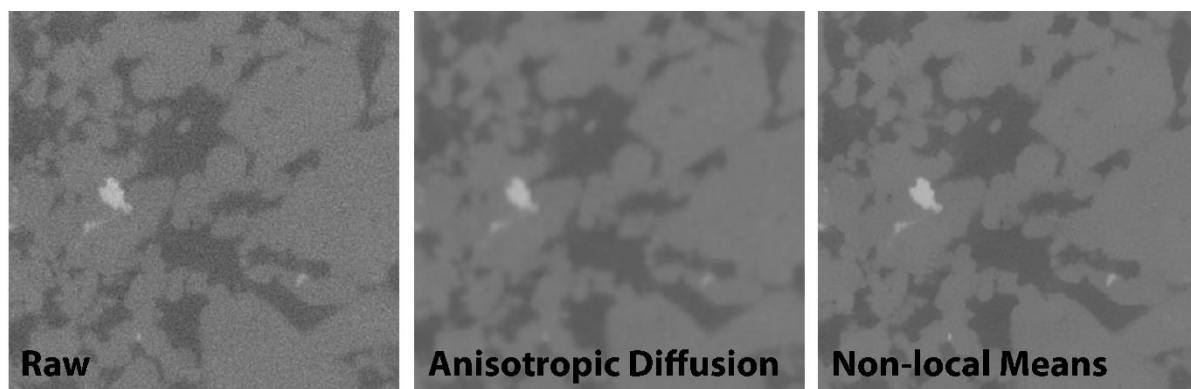
Figure 11— Side-by-side comparison of the raw data and the two most successful filters: Anisotropic diffusion and Non-local means.

In contrast, the *Non-local Means* filter defines the new value of a voxel by taking the weighted average of all voxels in a user-defined search window, weighed by the similarity with the target voxel. The filter is good for this study as it preserves most features of the data even small and thin asperities, which are the target here (grain boundaries). It also generates less data loss, but the computation time is enormous and can last for days.

The best result was obtained by applying the *Non-local Means* in 3D with a search window of 21 voxels and a similarity value of 0.8. The resulting filtered image is sharper than the raw data and the boundaries between the particles are sharpened. In general, the *Non-local Means* produces a better result than the Anisotropic Diffusion (Figure 11).

Non-local means <3D settings, search window of 21 voxels, 5-voxel

neighbourhood, similarity value of 0.8>
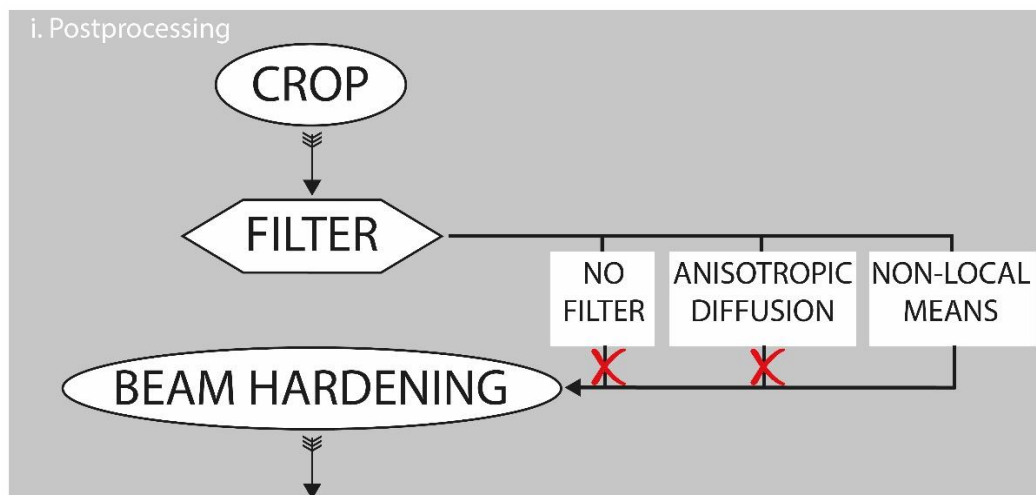
Figure 12— Detail of the tomography data processing workflow: filtering.

The filtered data also has a radial greyscale gradient where the core is darker than the rim. This is due to the increased beam path towards the centre of the sample. Beam hardening, especially for low energy x-rays, is a common feature of polychromatic laboratory scanners. Low energy x-rays can pass through the sample where the beam path is shorter (at the edges), whereas only the harder x-rays penetrate the sample in the centre. This means that the edge of the core appears less dense (lighter in colour) (Wildenschild & Sheppard, 2013; Jovanović *et al.*, 2013). Beam hardening is corrected during acquisition and reconstruction, but for higher density samples with low beam energies and heterogeneous phase distributions (i.e. this sample) this automatic procedure is insufficient. Additional correction was applied to normalise the data using the greyscale histogram.

Beam hardening correction < rotation around the z axis >

This module is used to correct the radial increase of the attenuation coefficient in cylindrical volume data. An average radial intensity profile is taken around a given rotation axis (here, the z axis) and then smoothed by a Gaussian filter and normalized. All radial intensities are then divided by the smoothed data which generates an averaged regional greyscale across the radius of the data.

3.3.3 Segmentation

Segmentation is the process of labelling voxels belonging to a particular class or having a particular attribute. The aim of this step is to label all voxels that are cumulus phase (olivine). The idea is to separate the tomography volume into two classes of voxels, the olivine crystals and the rest (pyroxene,

plagioclase, oxides and minor phases). The olivine and clinopyroxene are close in greyscale, thus the easiest approach is to label and remove each of the other phases in turn before performing a more detailed segmentation to untangle the olivine-pyroxene pair.

Step1: The first step is to extract the oxides. These are simple to extract because of their high greyscale values (due to their high density). The best result was produced by using an *auto-threshold* Module, which automatically computes the local position of the oxide boundary based on the histogram of the input image using the entropy of the greyscale as criterion. In applying the auto-segmentation, the user must set two parameters, defining a range in which the algorithm then uses the local greyscale environment to determine the placement of the phase interface (Pun, 1981; Kapur *et al.*, 1985).

Auto-Threshold < high intensities, 3D settings, 27000 - 28000, entropy >

Step2: Plagioclase, with its low linear attenuation coefficient, is segmented by changing the parameters of the auto-threshold algorithm.

Auto-Threshold < low intensities, 3D settings, 21000 - 21500, entropy >

Top Hat segmentation, designed to segment small features, was tested on both oxide and plagioclase segmentation with no improvement to the results.

Step 3: After the plagioclase and oxides are subtracted or masked from the 3D volume, the final step is to separate the olivine and clinopyroxene.

Olive and pyroxene have very similar greyscale values. In addition, some of the olivine shows an internal greyscale gradient toward the boundaries, suggesting a change in density through chemical zonation or alteration. These darker regions have the same greyscale values as the pyroxene. This makes it difficult to apply any threshold algorithm. Applying an *auto-threshold* that correctly labels the majority of the olivine and clinopyroxene incorrectly labels these gradational rims of olivine as clinopyroxene artificially creating a band of pyroxene around all the olivine. The best results were achieved when the oxides and plagioclase are physically removed from the image, thus changing the range of greyscale values used in

the labelling algorithm. They are removed by subtracting a mask of the oxides and plagioclase data from the cropped and filtered tomography data.

The most successful method for segmenting olivine and clinopyroxene is the *watershed* algorithm. This segmentation tool is particularly useful for segmenting two phases that have similar greyscale values or blurry, gradient-like contacts (Vincent and Soille, 1991; Wang, 1997). Conceptually, the algorithm uses an immersion simulation with water rising from specified markers on the greyscale (Beucher and Lantuéjoul, 1979). Where the waters meet defines the crest lines and the data is segmented along those lines. It addresses the internal gradient in the olivine grains as the internal gradient is weaker than the gradient on the olivine-clinopyroxene boundary.

The watershed algorithm uses a set of user-determined kernels (seeds or markers) from which the water rises. In this study, these seeds are levels of greyscale that best represent olivine, clinopyroxene and plagioclase as they are the three phases we want to detangle. Plagioclase is added to the *watershed* in case there are stray voxels of plagioclase not removed by the *auto-threshold* (step 2). The watershed segmentation is only applied to a targeted area around the clinopyroxene-olivine-plagioclase boundaries, where the gradients are. The *watershed* is run a first time using olivine, clinopyroxene and plagioclase as seeds.

Watershed < manually selected seeds in segmentation tab >

Visually, the result is more accurate than that achieved using the *auto-threshold* and all the remaining plagioclase on olivine-plagioclase boundaries is well segmented. However, too much clinopyroxene is labelled as olivine. The erroneously labelled olivine (actually clinopyroxene) is defined as the clinopyroxene seed and a second *watershed* is applied to the olivine volume resulting from the first watershed. The second watershed produces a good segmentation for olivine and there is minimal mislabelled clinopyroxene.

Watershed < manually selected seeds in segmentation tab >

Once all phases are correctly labelled, a binary mask of all the olivine grains is generated.

3.3.4 Separation

All voxels of olivine have now been identified and segmented into one labelled data volume. The next objective of the processing workflow is to separate the individual olivine grains from each other. The separated olivine grains will hereafter be referred to as particles.

The Avizo™ module *Separate objects* is used to achieve the separation. The module suggests two levels of separation: an aggressive one and a conservative depending on the severity of the separation wanted. A step-by-step illustration of the inner workings of the separation algorithms on a simplified sample of segmented olivine is shown in Figure 13 – (conservative separation) and Figure 14 (aggressive separation).

The conservative separation algorithm, also known as Chamfer Conservative is a high-level combination of a distance transform, watershed and numerical reconstruction. The algorithm performs a distance map to the nearest void voxel to identify the local distance maxima (Figure 12, B). These are used as the seeds/markers for a *watershed* which identifies the crest lines representing potential separation boundaries (Figure 12, B). The algorithm uses the marker extent, a user-determined parameter that determines the minimum ratio between the markers for separation to occur. In Figure 12, the marker extent is fixed at 2, meaning the ratio between the values of the marker has to be at least 2. This is the case for two markers, which leads to the separation of two particles (Figure 12, C). This type of separation does not promote strict separation and targets isolated objects.
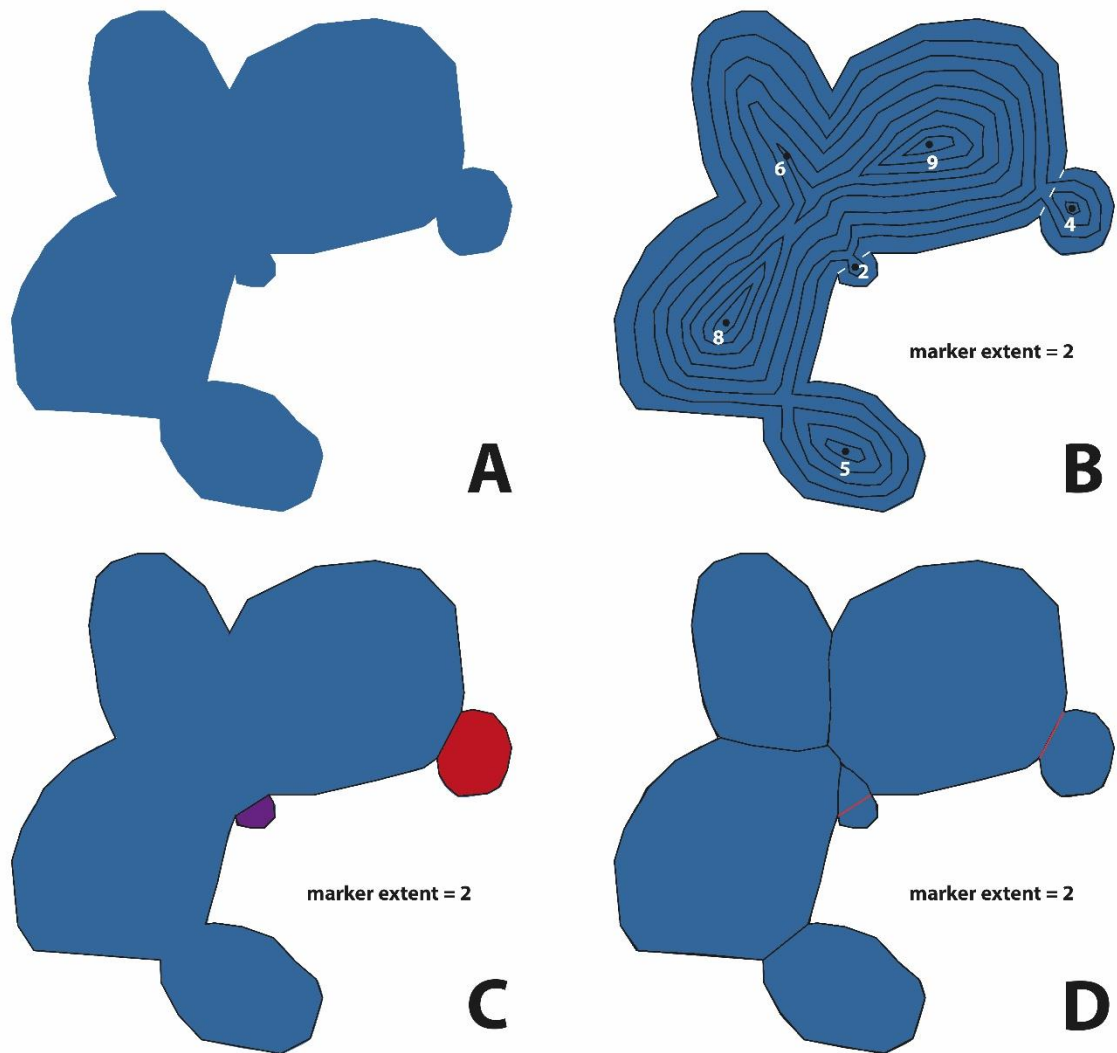
Figure 13 – Detail of the conservative separation algorithm. A shows the segmented volume ready for separation; B depicts a distance map to the nearest void space produced on the volume showing the local maxima and their value. The separations that fulfil the marker extent criteria are shown in dashed lines; C shows the separated objects; D compares the separation to the real crystal shapes of clumped olivine.

The aggressive separation (also known as Skeleton-aggressive) first produces a distance map of the segmented object to the nearest void voxel (Figure 14, B) from which the highest values are retained to form the skeleton of the object (Yousef *et al*., 2007). The skeleton (Figure 14, orange lines in B) is the thinnest representation of the segmented object that preserves its shape. The connectivity of the lines that make up the skeleton is evaluated: they are either categorized as "channel lines" or "dead ends". The aggressive algorithm breaks up the object on the "channel lines" (Figure 14, B) to produce a first separation (Figure 14, C). A conservative separation is then performed on the result of the first separation (Figure 14, D), breaking up the segmented object even more (Figure 14, E). The aggressive separation promotes more separation than the conservative one, breaking up clumps as well as isolated grains.
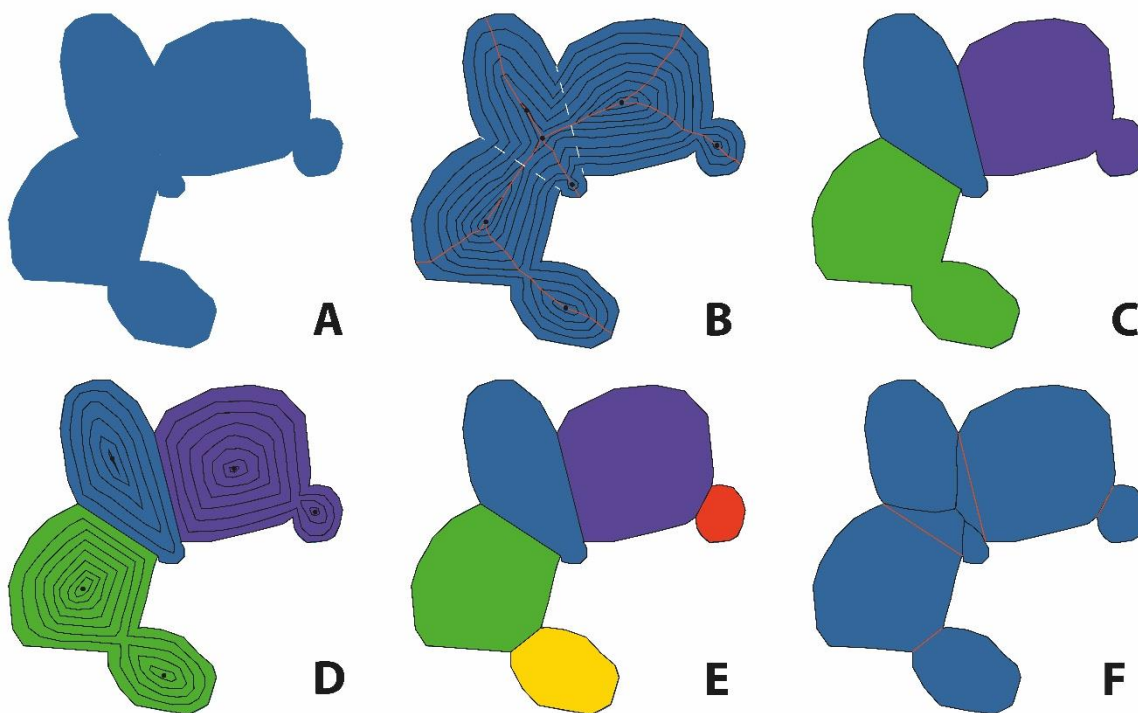
Figure 14 — Detail of the aggressive separation algorithm. A shows the segmented volume ready for separation; B depicts a distance map to the nearest void space produced on the volume showing the local maxima and the segments forming the skeleton of the geometry (orange lines). The separations along the connected segments are shown in dashed lines; C shows the separated objects; D depicts a distance map to the nearest void space produced on the new separated volumes; E shows the separation of the particles with maxima that fulfil the marker extent criteria; F compares the final separation to the real crystal shapes of clumped olivine.

There are several other user-based parameters that are used to define the behaviour of both the conservative and aggressive applications. Connectivity can be defined requiring planar face-to-face voxel contact, or with edge or corner contact being sufficient. Face connectivity will separate more particles.

The *Separate Objects* module is applied to the segmented olivine in both conservative and aggressive mode with variations of the user-controlled parameters, but the results are not realistic. In general, large objects are divided straight down the middle (Figure 15, B and C), which is unlikely to be real given the known geometry of the grains on the thin section. For smaller isolated objects, the result is good, although the largest of them are artificially divided down the middle as well. The separation of clumped olivine is not satisfactory either, with arbitrary separations down and across clumps.
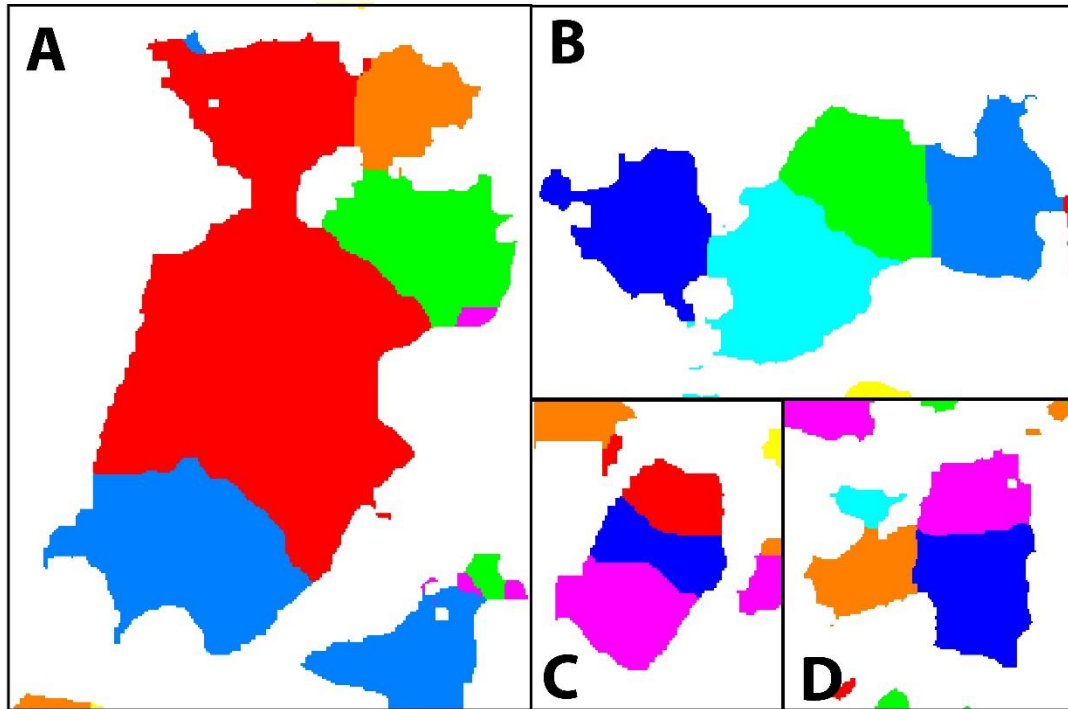
Figure 15 – Detail examples of separation of the processed tomography data.

As the separation is generally good on isolated objects, we apply a stepwise iterative separation process, with the satisfactory particles identified at each stage and removed from subsequent processing. The separation algorithms can then be re-applied with different parameters to tackle the remaining grains until all the volume is separated into realistic shapes. The processing is separated into four iterative steps.

Step 1: Isolated, more rounded particles are targeted using a conservative separation. A high connectivity (neighbourhood) requiring face to face contact of the voxels is used to properly separate isolated particles and the marker extent is fixed at 6 to limit the division of larger particles.

Separate objects < conservative, 3D, neighbourhood 6, marker extent 6 >

The isolated particles, which are also the rounder ones, are well separated, while the clumps of olivine crystals are separated in unrealistic shapes (cf. Figure 15). The separated objects are first eroded (shrunk by 10 voxels) and smoothed to accentuate the isolated particles. To remove the well-separated grains, the smoothed and eroded separated objects are sorted by roundness, with only the roundest selected and removed from the next step of analysis.

Label Analysis < 3D, roundness >

Step 2: The remaining objects (all but the roundest) are dilated (grown back by 10 voxels) and binarised. The remaining tomography volume is largely formed of olivine clumps. There is still a slight greyscale gradient within the olivine clumps so the darkest parts are segmented out manually using a selection tool in the Segmentation window. The darker regions are removed to attempt to obtain triple points, the intersection of three olivine grains, and the remaining labelled volume is processed using

Separate objects < aggressive, 3D, neighbourhood 6, marker extent 6 >

The new separated objects are then opened (eroded and dilated) by 2 voxels to avoid noise in the separated image and any face and corner contact between the objects. Visual inspection reveals that no isolated particles are found within the largest objects, and so the 40 000 largest objects (i.e. the remaining olivine clumps) are filtered out for the next step of processing. All but the 40 000 largest particles are put aside for later.

Sieve analysis < ~40 000 largest particles >

Step 3: The binarised clumps from the previous separation are separated using an aggressive separation and a lower marker extent to promote more separation.

Separate objects < aggressive, 3D, neighbourhood 6, marker extent 4 >

The 2000 biggest particles are filtered out of the newly separated objects using

Sieving analysis < ~ 2000 largest particles >

Step 4: The last round is an aggressive separation with an even higher connectivity degree and a low marker extent to break up the last of the clumps. All the separated particles are then added to a single file, ready for the dimensional metrology.

Separate objects < aggressive, 3D, neighbourhood 18, marker extent 2 >

3.3.5   Thin section data treatment

To analyse the olivine crystals in the thin section, the crystals need to be segmented from a scanned image. The outline of each crystal is drawn by hand in ImageJ and exported into Avizo™. When the

boundary of touching crystals was unclear on the plain-light scan, a cross-polarised microscope was used to determine the exact outline of the crystals. In Avizo™ the olivine crystals exist as a binary file composed of the outline of each crystal (1 pixel thick lines) surrounded by void. An *auto-threshold* segmentation is applied to the thin section data to select only the material inside the crystal outlines. The areas of non-olivine that are fully enclosed by olivine grains (and therefore segmented as they fall entirely within the outlines) are removed manually in the Segmentation window, leaving only the grains as a collection of disconnected particles that are not touching, a critical control on the separation. At this point, the particles are disconnected but exist as one entity, therefore a *Separate Objects* is applied to separate them into individual particles. The separation algorithm is conservative with a high marker extend to only discretise the particles not divide them.

Separation < conservative, 3D settings, neighbourhood of 6, marker extend 4 >

The separation is completely controlled as the particles are not physically in contact and therefore produces a perfect separation. Lastly, the particles are grown by 1 pixel to compensate for the deleted outline.

3.3.6 Extraction of measurements

At this stage, the 3D tomography volume and the thin section are satisfactorily segmented and separated. To properly compare the thin section to the tomography, the thin section needs to be located in the core. This is called image registration and can be performed in 2D or 3D data. There is an automatic registration module in Avizo™ designed to position one object with regard to another based on the greyscale. The application to 2D and 3D data, however, does not produce plausible results and better registration is achieved manually. The outline of the thin section and the silhouette of the core are used for coarse alignment and then positioned more precisely by matching up the shape of plagioclase and oxides primarily. Once aligned, the transformed 2D data is "resampled" to homogenise voxel sizes, orientation and location in space in both images.

Performing this step before extracting the measurements from each of the separated particles means that the spatial coordinates of the tomography volume and thin section are uniform. Spatial data from the different datasets can then be plotted overlain as they share a coordinate system.

To allow comparison of tomography data and the thin section, three data sets are generated from the tomography data. The plane where the thin section intersects the tomography volume defines the **tomography slice**. It is the tomography equivalent of the thin section. Using the position of the tomography slice, the **tomography stack** is extracted. The stack is a 3D render of the particles in the tomography slice. They are extracted from the tomography volume by filtering the particles by an attribute that provides the coordinate of the first and last voxel of a particle in each direction X, Y, Z. The thin section – and therefore the tomography slice – is defined in X and Z (and only one Y coordinate) and is 30 µm thick. The particles of the tomography volume are filtered along the Y axis for any particles that finish before the Y coordinate ± 15 µm of the tomography slice and particles that start after that Y coordinate.

To facilitate the comparison of the tomography datasets to each other, the *Label Analysis* of the slice and stack is run using the output of the tomography volume analysis as a reference. Since the particles in the slice and stack exist also in the volume, they have the same index and can, therefore, be directly compared to each other. The thin section data cannot be linked to the other data sets in the same way because the grains are not identical in both data sets. Particles can, instead, be compared using the barycentre coordinates and other geometric data.

The dimensional measurements of each particle in each data set are extracted using

Label Analysis <2D or 3D options used, measurements listed below>

The *Label Analysis* is used to extract the following measurements or attributes:

For 2D data sets (thin section, tomography slice and stack):

- Barycentre X and Y coordinates: coordinates of the centre of mass of each particle [µm]
- Area: the area of each particle [µm^2]
- Equivalent diameter: the diameter of a circle of the same area as each particle [µm]
- Shape factor: a dimensionless number expressing the roundness of a particle
- Volume: the volume of each particle [number of voxels]

- Feret diameters: group of diameters defined as the distance between two parallel tangents of the particle at an arbitrary angle [μm]

- Length: the longest Feret diameter [μm]

- Width: the shortest Feret diameter [μm]

For 3D data sets (tomography stack and volume):

- Barycentre XYZ: coordinates of the centre of gravity of each particle [μm]

- Area 3D: the area of the surface of each particle [$μm^3$]

- Equivalent diameter: the diameter of a sphere of the same volume as each particle [μm]

- Shape factor: a dimensionless number expressing the roundness of each particle

- Volume 3D: the volume of each particle [$μm^3$] and [number of pixels]

- Feret diameters: distribution of lengths of bounding box oriented along specific directions [μm]

- Feret shape: ratio of the Feret diameter normal to the shortest ferret diameter over the smallest Feret diameter

- Length: the longest Feret diameter [μm]

- Width: the shortest Feret diameter [μm]

- Breadth: is the Feret diameter normal to the length and the width [μm]

2D and 3D analyses are run on the tomography stack so that the volume (from 3D) and area (from 2D) are directly comparable to the thin section data and the tomography slice.

3.4   Methods of analysis and comparison

The thin section data and the tomography data cannot simply be compared to the other as the objects are on different scales. The comparison necessitates comparing the same type of objects and of similar size. For this reason, the comparison is organised in a succession of steps.

The first step is to compare the thin section data with the same slice within the tomography data, the tomography slice. This tests how close the tomography data in the slice is to the thin section, which is used as a reference for the olivine crystals in the sample. The accuracy and precision of the tomography

data processing are evaluated by comparing the dimensional metrology of the particles (size, shape, occurrence, …) and the structure of the mush in both objects.

The second step is to compare the tomography slice to the 3D render of the particles within it, the tomography stack. The idea is to quantify the difference in the dimensional metrology between a set of particles analysed in 2D and the same particles analysed in 3D. This also evaluates how and what information is given when working in 3D. This step works with a simplified system where the particles in the stack are the same as in the slice.

The third step is for evaluating how representative the tomography stack is of the whole tomography volume. The size, shape and structure of the mush at the two different scales are compared.

The final step is to compare the thin section data to the tomography volume using prior comparisons and a stereological conversion of the 2D data in 3D. The aim of this section is in two parts: i) to evaluate how close the tomography data is to the thin section and if the difference in scale can compensate for the differences in dimensional metrology: ii) to test the pertinence of studying cumulate igneous rocks in 3D, and whether the extra information provided by the 3D data adds significantly to the knowledge provided by a thin section.

The tools used for the comparison are described in section 2.2 and their application is detailed below.

3.4.1   Numerical and particle scale methods

Determining particle size and distribution throughout the sample provides valuable information about the structure of the mush. The area distribution adds to the characterisation of the mush structure. The size and area distributions can be performed in 2D (thin section), but the accuracy of the result is enhanced using by 3D data (eg. Carlson and Denison, 1992; Holness, 1997). There are several ways of converting 2D observations in 3D, however, we will be using a stereological approach developed by Sahagian and Proussevitch (1998).

The area for each particle is provided by the *label analysis* performed in Avizo™. For size, the equivalent diameter is used.

3.4.1.1 Bulk statistics

To have an overview of particle size and area, the mean, mode and median are calculated. The arithmetic mean represents the central value of a data set calculated by dividing the sum of all values by the number of values. The mode is the most frequent value in the data set and the median corresponds to the 50th percentile of the cumulative distribution of the data.

To illustrate the size distribution, histograms for area and equivalent diameter are plotted (e.g. Figure 16). Both are useful tools for comparing data, although the measured area in 3D is a surface area and is therefore not directly comparable to the 2D measurement.
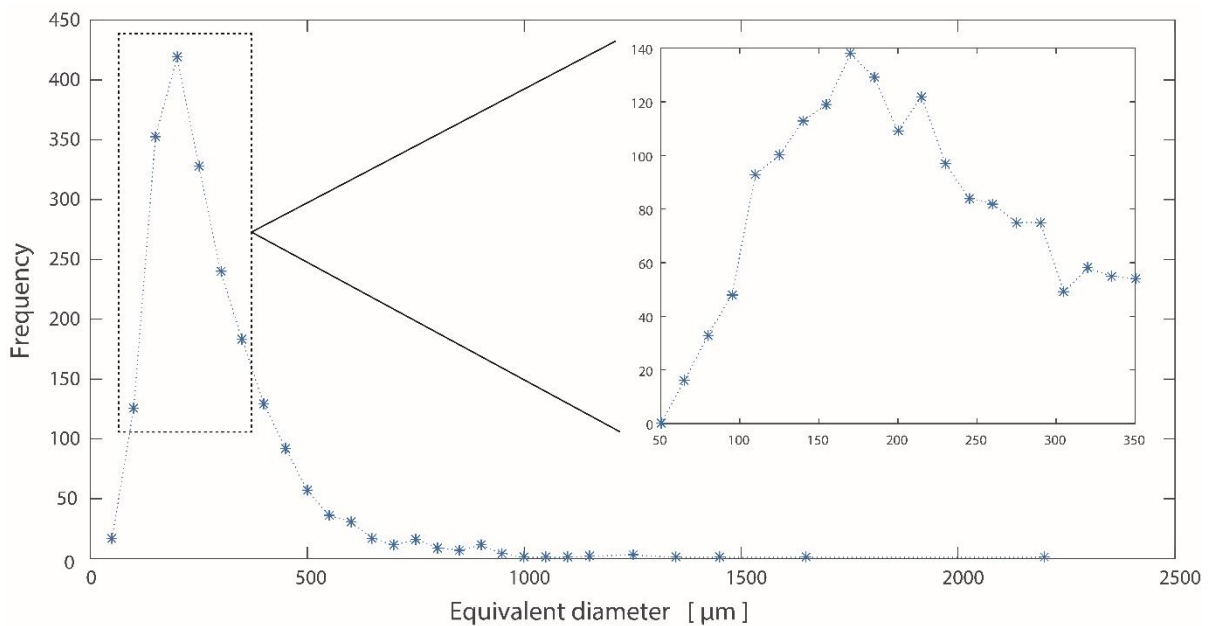
Figure 16 – Equivalent diameter histogram of particles in the thin section. The histogram was constructed using size bins of 50 μm. The close-up of the peak is a histogram constructed using size bins of 15 μm.

3.4.1.2 Crystal size distribution

Crystal size distributions are a quantitative tool widely used to determine the structure of a rock or, mush. Igneous processes such as crystal nucleation and growth rate, at play during the formation of the rock, can be inferred from the result (Cashman, 1988; Marsh, 1988a; Cashman and Marsh, 1988; Cashman and Ferry, 1988). In this study, we use CSD only to characterise and quantify mush structure and then compare the 2D and 3D results.

CSD is an empirical relationship based on only one parameter: crystal length, size or area. In this work, the equivalent diameter is used to compute CSDs as it is the **only** attribute that is directly comparable from 2D to 3D. The CSDs are histograms generated by classifying the data into defined linear size bins

and computing the frequency of elements in each bin. For each bin, the 95% confidence intervals are calculated to 2σ precision (Gualda, 2006), using $2\sigma = 2\sqrt{N}$, where N is the number of values in each bin. In this study, we plot CSDs as the size of the particles on the X axis against the natural logarithm of the frequency of crystals in each size bin (see example Figure 1).

3.4.1.3   3D stereological conversion

The accuracy of the CSD is significantly enhanced by using 3D data, and as 3D data are not often available, stereological corrections are used to transform 2D data into 3D. The stereological conversion used here to compute 3D particle size distributions from 2D data, based on Sahagian & Proussevitch (1998), was translated into an R script by Dr D. Neave for work on bubbles in volcanic rocks (Hughes *et al.*, 2017). This is considered appropriate for olivine, which is sub-rounded.

The code necessitates input values from the 2D data to calculate the 3D conversion. The input is similar to a histogram, with size bins, minimum and maximum values. For each bin, the number of particles per area unit (N_A) is necessary as well as a mean the particle size for each bin. The code is run in R with the *plyr* package (Wickham, 2016) and produces an output file with the 3D conversion data. The result is composed of the same size bins, each associated with a number of particles per volume unit (N_V). The equivalent diameter is used for particle size. The results are visualised in a CSD graph (see Figure 1, **Error! Reference source not found.**).

3.4.2   Spatial methods

To visualise the spatial distribution of the particles, the location of particle barycentre and the corresponding area was mapped as using the spatial coordinates from the tomography data processing.

3.4.2.1   Barycentre location

The barycentre maps are created by plotting the X and Y coordinates of the centre of mass of each particle. The barycentre of each particle is provided by the *Label Analysis* in Avizo™. The maps are created for the 2D data sets (thin section and tomography slice) and for the tomography stack (3D render of the particles in the tomography slice; e.g. Figure 17), where the 3D data is projected on the 2D plane using just the X and Y coordinates of barycentre.

The barycentre location maps provide valuable qualitative information about the spatial distribution of the particles. Comparison can be done by overlapping two maps, the thin section particles and the tomography slice for example (Figure 17) to judge how close the particles are to each other.
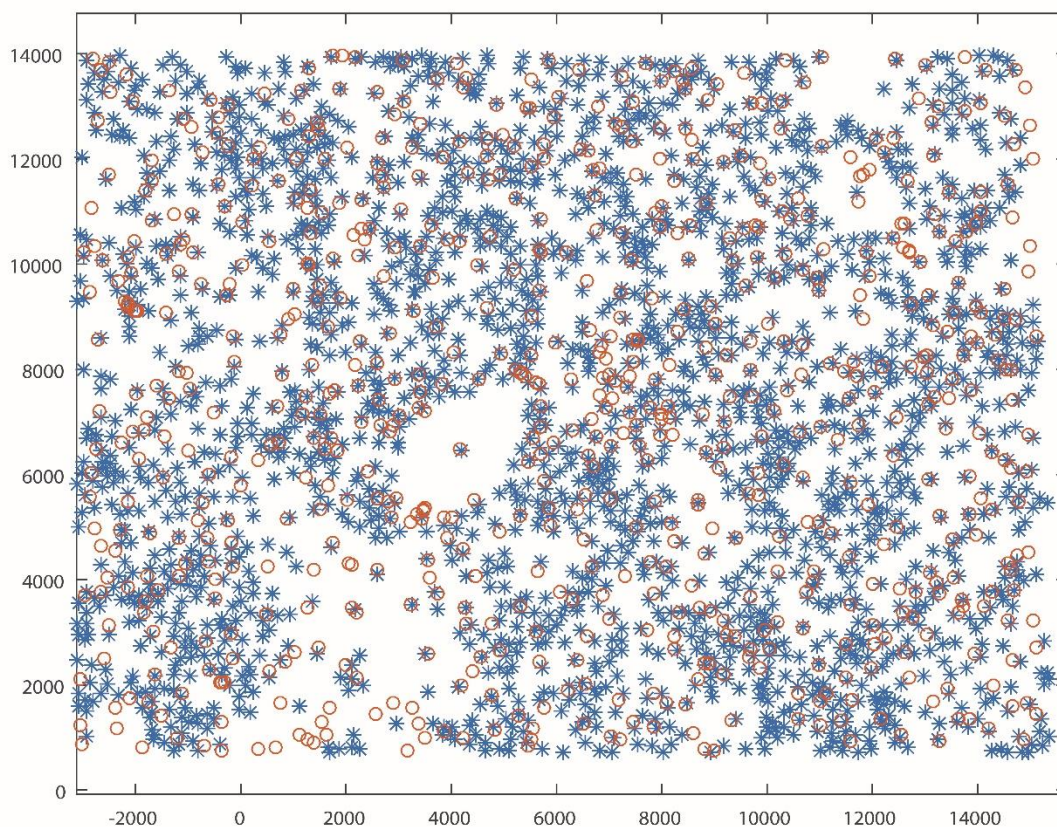
Figure 17 – Barycentre location for the thin section and tomography slice overlaid. The blue circles are the thin section and the orange stars are the tomography slice. X and Y axis are position in μm.

3.4.2.2   Nncross

The *nncross* function of the R package *spatstat* (Baddeley *et al.*, 2015) provides a way of quantitatively assessing the proximity of particle barycentre location between two data sets. For each particle in one data set, the function finds the nearest neighbour in the second data set and computes the distance between the two.

The input for the *nncross* function is two vectors (point pattern data sets; see below) containing the X and Y coordinates of particle barycentre of each data set. The output is composed of the particle index of the first data, the distance between the nearest neighbour pairs matched up by the *nncross* function and the index value of the paired particle in the second data set. Below is an example of the code used in R to compute the *nncross* function:

```
install.packages("spatstat")
```

```
library(spatstat)
```
<div align="center">Installing the package in R, adding the package to the library</div>

```
TS <-read.csv("TS-XYZ.csv", header = TRUE)
Slice_2D <- read.csv("Stack-XYZ_341.csv", header = TRUE)
```
<div align="center">Reading the csv files containing the data</div>

```
TS_bary <- TS[ ,1:2]
Slice_2D_bary <- Slice_2D[ ,1:2]
```
<div align="center">Selecting the appropriate columns in the cvs file</div>

```
TS_baryPPP     <-     ppp(TS[     ,1],TS[     ,2],     window=owin(c(-
    3112,15364),c(715,13973)))
M2D_baryPPP    <-     ppp(Slice_2D_bary[   ,1],Slice_2D_bary[   ,2],
    window=owin(c(-3046,15117),c(740,13973)))
```
<div align="center">Generating the point pattern data sets for the two data sets</div>

```
M2D_to_TS        <-        nncross(M2D_baryPPP,TSFilt_baryPPP,
    iM2D_bary=NULL, iTS_bary=NULL)
```
<div align="center">Computing *nncross* function</div>

```
N1 <- nncross(M2D_baryPPP, TSFilt_baryPPP)$which
```
<div align="center">Storing the index reference of the nearest neighbour pairs</div>

```
plot(superimpose(M2D_baryPPP=M2D_baryPPP,
    TSFilt_baryPPP=TSFilt_baryPPP),        main="nncross",
    cols=c("red","blue"))
arrows(M2D_baryPPP$x,  M2D_baryPPP$y,  TSFilt_baryPPP[N1]$x,
    TSFilt_baryPPP[N1]$y, length=0.03)
```
<div align="center">Visualisation</div>

```
write.csv(M2D_to_TS, file = "M2D_to_TS.csv", append = FALSE,
        row.names = TRUE, col.names = TRUE)
```
<div align="center">Storing output in a csv file</div>

Visualised graphically, the output expresses the position of the particles in both data sets and the paired nearest neighbours and the distance separating them is shown by black arrows (see example Figure 47). The length of the arrows is proportional to the distance between the paired particles from both data sets

From here on, the nearest neighbour computed using the *nncross* function will be referred to as *nncross nearest neighbour*.

3.4.2.3   Area map

The barycentre maps and the *nncross* function do not take into account the area of the particle, which can lead to false interpretations. The barycentre map will show a region of close particle packing if there are large close-packed particles or smaller well-spaced particles.

It is therefore important to consider particle barycentre location as well as the area, and area maps of the 2D datasets are therefore generated. Circles representing the area of each particle are centred on their barycentre location with a radius proportional to their area. The area maps are generated for the 2D datasets only (see example, Figure 18).
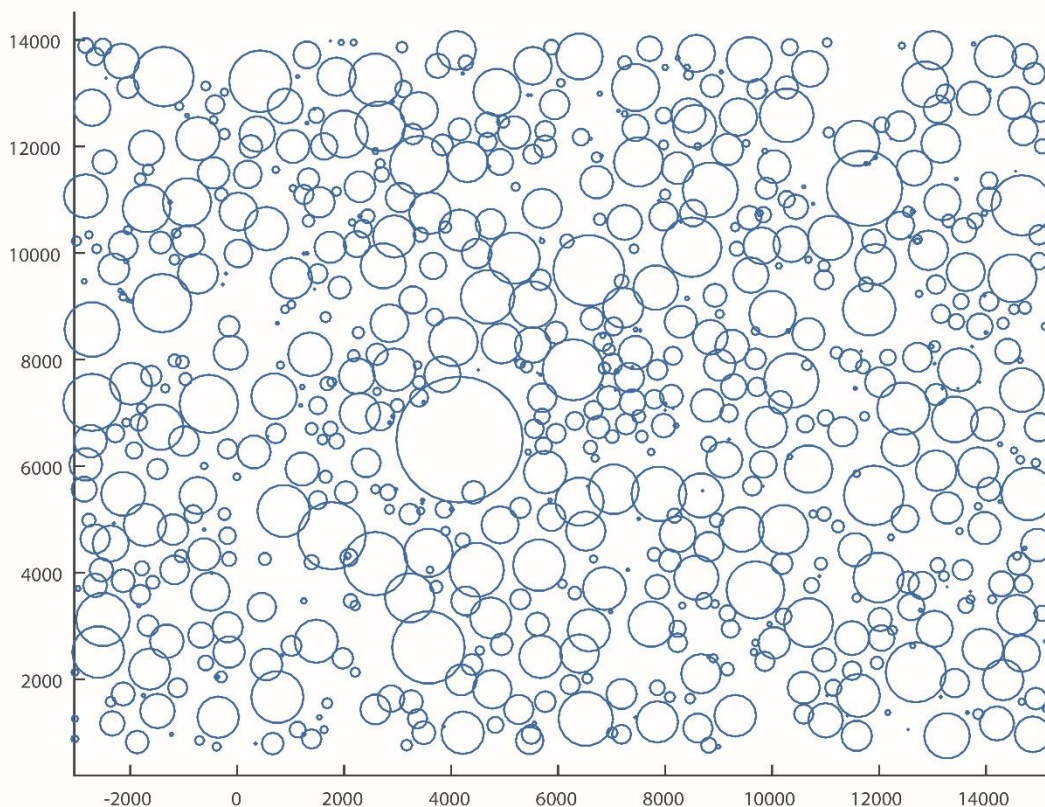
Figure 18 – Example of an area map. The area is represented by a circle centred on the barycentre location of each particle and with a radius proportional to particle area.

3.4.3   Mush structure methods

To describe the spatial distribution of particles in the mush, Ripley's K-function, as well as the pair correlation function, are considered. Both are calculated, but the pair correlation function data only are shown, as these give the same information as the K function as well as additional information.

3.4.3.1   Ripley's K function

Ripley's K function is calculated in R and is included in the *spatstat* library. The function has similar input to the *nncross*, namely the vector containing the barycentre coordinates for one data set.

An example of the script is as follows:

```
K_TS    <-   Kest(TS_baryPPP,   r=NULL,   rmax=NULL,   breaks=NULL,
correction=c("border", "isotropic", "Ripley", "translate"))


Lr       <- sqrt(K_TSFilt[["border"]]/pi)-K_TSFilt[["r"]]

Lrtheo   <- sqrt(K_TSFilt[["theo"]]/pi)-K_TSFilt[["r"]]
```

The K function is called `Kest` in *spastat* and the input vector is `TS_baryPPP`. The output of the

function is composed of several corrected versions of the K function versus r, the radius of the circle

considered in the function. The function is corrected for edge effects on the border of the sample to

reduce the bias on the function (Rippley, 1988; Baddeley, 1998). The correction use in this study is the

isotropic correction that is designed for rectangular or polygonal samples.

The K function is then visualised in its transformed form L(r). The output of the function also includes

an estimation of K for complete spatial randomness ("`theo`") such as L(r_{theo}) = 1 for all r. The

visualisation of Ripley's K function is illustrated in Figure 3.

3.4.3.2   Pair correlation function

The clustering of particles in a 2D or 3D dataset is evaluated using the *pair correlation function*,

commonly used in material science and applied to geology for the distribution of metamorphic

porphyroblast (e.g. Daniel & Spear, 1999). PCF is a radial distribution function that calculates the

probability of finding a particle in a given radius r. If the value is greater than one (one being the value

for complete spatial randomness), the crystals in the sample are clustered. If smaller than one, the

crystals are ordered.

The PCF function in R runs on the *spastat* (Baddeley *et al.*, 2015) and is called pcf. The input is a

barycentre coordinate vector. To check the statistical significance of the function, simulation envelopes

are calculated. They represent 39 iterative simulations of the PCF for random data of the same size as

the actual data set. They represent the area where 95% of the simulations fall. If the function is in the

region defined by the envelopes, the function is statistically insignificant and is considered as noise.

```
TS_PCF <- pcf(TS_baryPPP)
```

```
                                                          Computing nncross function
epcf <- envelope(TS_baryPPP,fun=pcf,nsim=39)
                                          computing simulation envelopes, 39 simulations
hipcf <- epcf[["hi"]]

                                                              defining top envelope
lopcf <- epcf[["lo"]]

                                                           defining bottom envelope
plot(TS_PCF[["iso"]]~TS_PCF[["r"]])
lines(TS_PCF[["theo"]]~TS_PCF[["r"]])
lines(hipcf~TS_PCF[["r"]])
lines(lopcf~TS_PCF[["r"]])
```

3.4.4   Shape

As olivine is usually sub-rounded, comparing the 2D shape of the particles between the thin section and the tomography data is a proxy for the accuracy of the shape of the particles in the tomography data.

The shape factor is given by $S = \frac{P^2}{4\pi A}$, where P is perimeter and A is area. For a circle, the shape factor is 1: $S_{circle} = \frac{(2\pi r)^2}{4\pi\,(\pi r^2)} = \frac{4\pi^2 r^2}{4\pi^2 r^2} = 1$. The closer the particle shape factor is to one, the rounder they are. Larger values of S belong to more angular particles. This attribute can be used in 2D and in 3D by using the surface area of each particle compared to the surface of a sphere.

The length and width of the particles are also attributes that are used to compare particle shape. These attributes are provided directly from the *Label analysis* in Avizo™.

4 Results

4.1 Textures

4.1.1 Thin section textures

The Tugtutôq peridotite is entirely crystalline and contains olivine, plagioclase and clinopyroxene as well as oxides. There are also small amounts of apatite and biotite. Observed under the microscope, olivine crystals are sub-rounded and have conchoidal fractures. Plagioclase and clinopyroxene are present as large oikocrysts, enveloping the cumulate olivine crystals (Figure 19). There is some alteration around olivine, breaking it down into a fine-grained aggregate. This leads to wider and less sharp crystal boundaries (Figure 20, A).
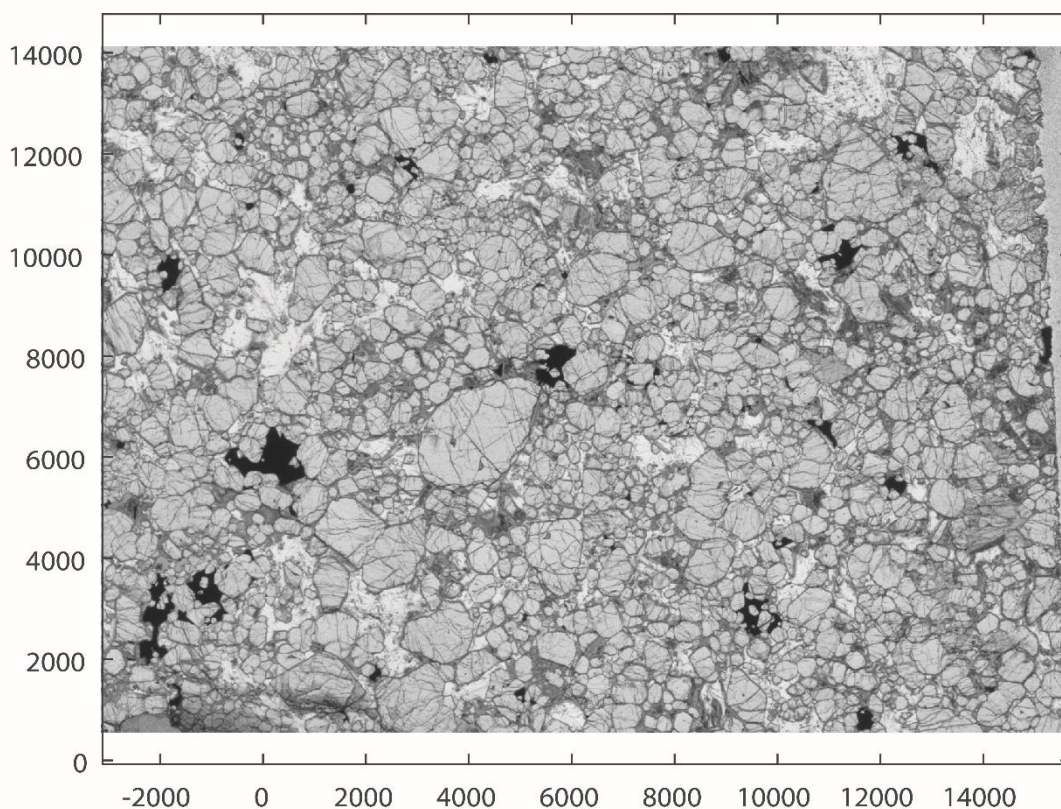
Figure 19 – High-quality scan of the thin section. The sub-rounded grains are olivine crystals. The dark patches are oxides and the interstitial phase is plagioclase and clinopyroxene. X and Y axis are in μm.

Olivine crystals are dominant and range from ~20 μm to 2200 μm across. The largest particles are not evenly distributed throughout the thin section but concentrated towards the bottom western corner of the sample. The majority of the particles have medium to small sizes and are evenly distributed, while small crystals either fill the space between the medium-sized crystals (Figure 20, C) or agglomerated around larger crystals (Figure 20, A).
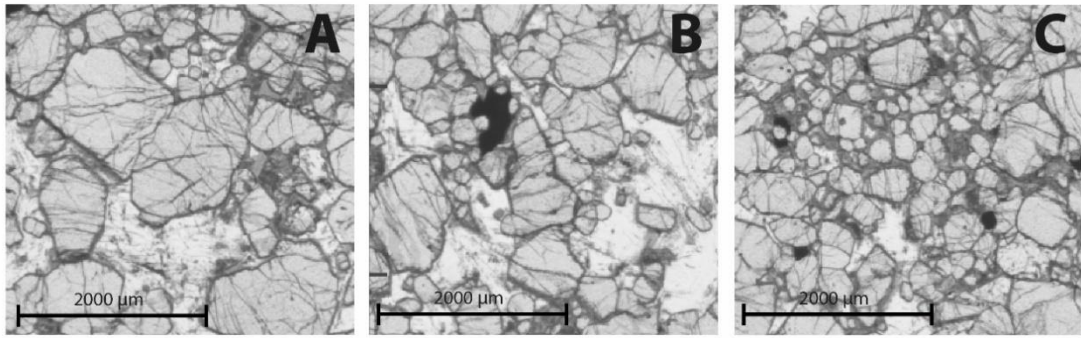
Figure 20 – Close up of olivine textures found in the thin section. A: small crystals agglomerating around large crystals; B: large olivine crystals clumped together and the contact forces them to accommodate their shape; C: accumulation of small olivine crystals in interstitial phases.

Olivine crystals are either clumped, touching on one or several sides (Figure 20, B) or isolated (not touching, or only rare point contact with other olivine crystals; Figure 20, C). When touching, the crystals accommodate the shape of their neighbours by annealing (Figure 20, A and B) or the small gaps are often filled with alteration product (Figure 20, C). Apart from the very large crystals (e.g. the one in the middle and in the north-eastern corner of Figure 19), olivine crystals are often found in close proximity to olivine of similar size (Figure 20, B).
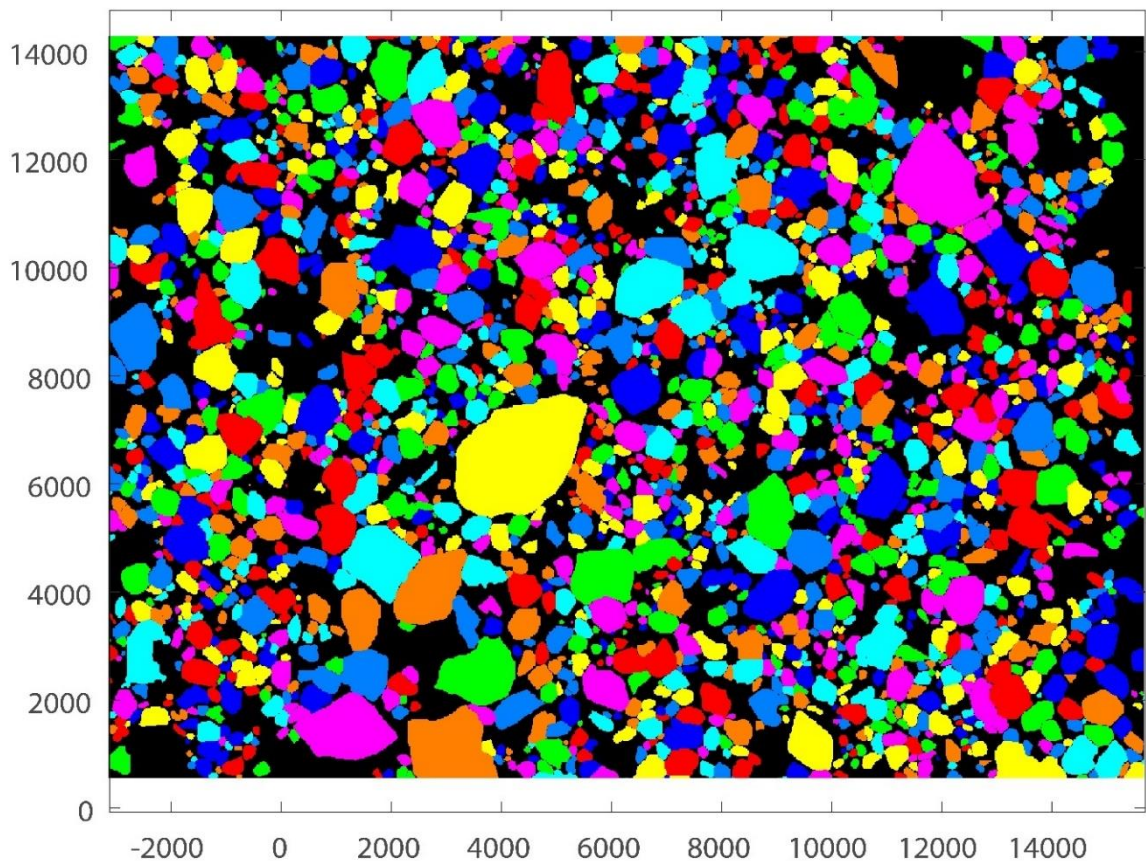
Figure 21 – Separated and segmented olivine from the thin section. The colours are arbitrary. X and Y axis are in µm.

66

The processed thin section is shown in Figure 21, using arbitrary colours corresponding to the grain index value (default map generated by Avizo™). The smallest crystal measured is 2 pixels across, with a pixel size of 11.9 µm. The segmentation and separation are a close reproduction of the textures observed under the microscope. Particles at the edges of the sample are not included because these are truncated by the cropping of the sample and could affect the statistics.

4.1.2   Tomography textures

An example slice through the raw 3D greyscale XRCT data is shown in Figure 22. There are four mineral phases visible here, as shown by the different greyscale regions: the lightest are the oxides; the darkest is plagioclase; and clinopyroxene is only a little darker than olivine which makes them difficult to distinguish (see Figure 22).
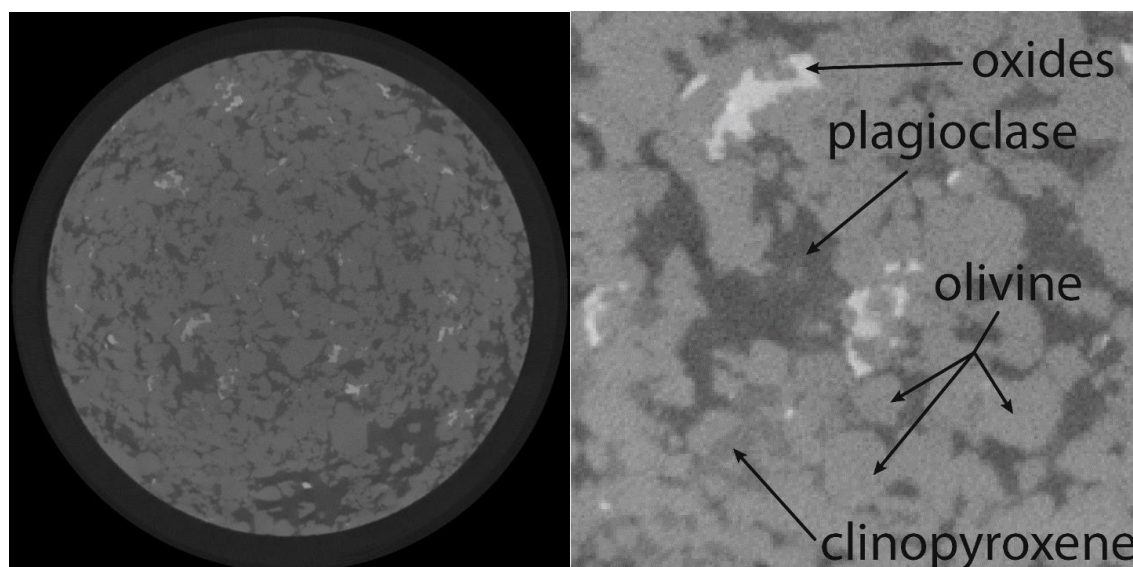
Figure 22 – Left: Slice through the 3D greyscale tomography data; the view is perpendicular to the long axis of the core. Right: Close-up of slice to identify the mineral phases in the raw data

The segmented olivine is shown in Figure 23. The segmented olivine crystals are not separated yet and exist all as one object. The pores represent anything that is not olivine: plagioclase, clinopyroxene and oxides are considered "pores". The general appearance is that olivine takes up most of the sample, but the "pore" space is plotted on its own shows that it is only an artefact of visualisation in 3D (Figure 24).
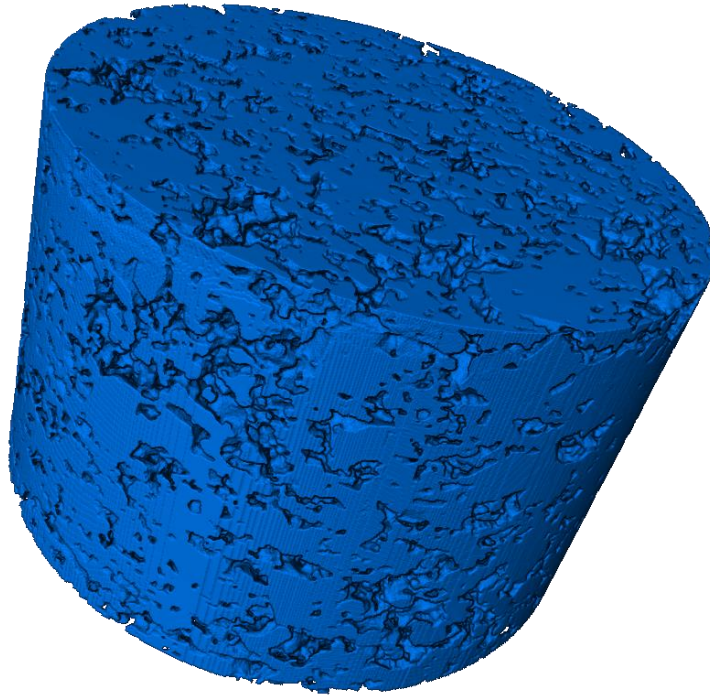
Figure 23 –3D representation of the segmented olivine. The "pores" are anything that is not olivine.
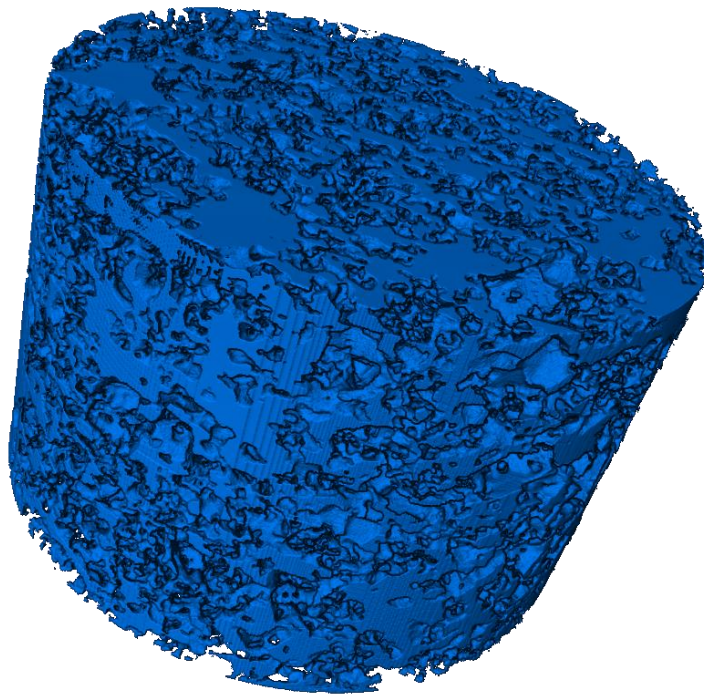
Figure 24 –3D representation of "pore" space in the segmentation This volume represents any mineral phase that is not olivine.
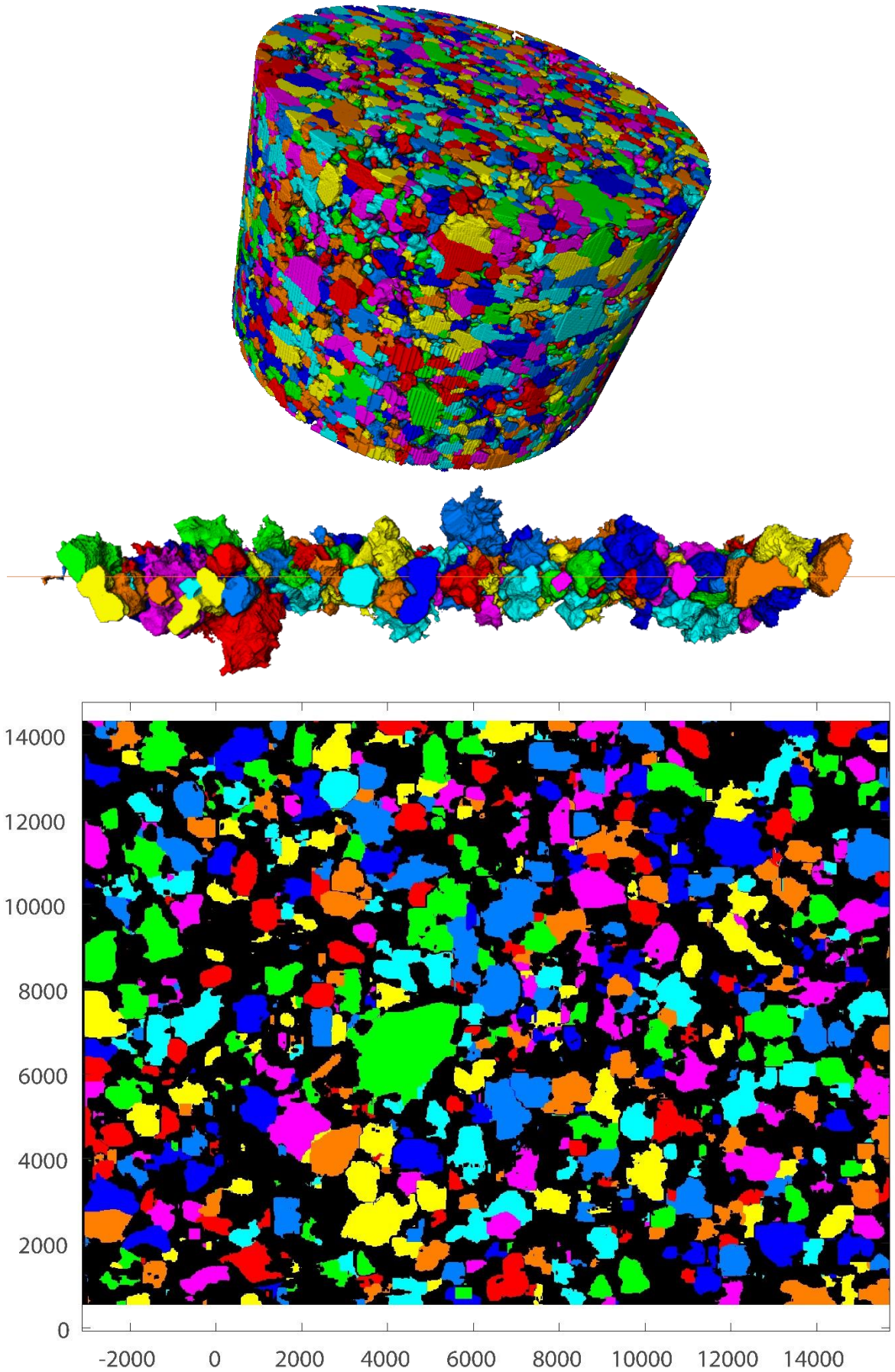
Figure 25 – Visualisation of the separated particles. Top: 3D representation of the separated particle in the core. The colours are arbitrary. Middle: 3D render of the particles in the slice equivalent to the thin section position in the core, the tomography stack. Bottom: tomography slice through the core, equivalent to the position of the thin section.

The separated olivine particles are shown in 3D (Figure 25, top), in the stack (Figure 25, middle) and in the tomography slice (Figure 25, bottom). Particles of all sizes are found in all regions, ranging from 1 pixel/voxel (11.9 µm) to 2221 µm across (Figure 26, B).
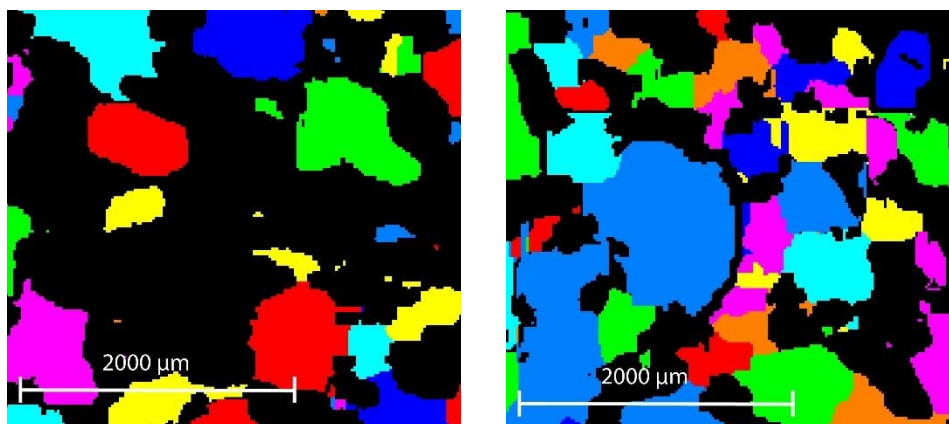
Figure 26 – Close up of textures in the tomography slice. Left: example of particles that are not touching. Right: example of particles that are clumped together.

4.2 Comparison of 2D data sets: thin section and tomography slice

4.2.1 Bulk statistics

Statistics are performed on the size and area of the particles to characterise their distribution in the sample. The results provide information about the textures of the crystals and the overall architecture of the mush.

4.2.1.1 Thin Section

The mean, median and mode equivalent diameter of the particles in the thin section are shown in Table 1. Due to the 2D nature of the thin section, these diameters are essentially intersection diameters of the crystals in 3D. The mean and median have a difference of 20%, meaning the mean is affected by the large particles. The mode value is the smallest and is half the value of the median.

Table 1: Quantitative evaluation of particle equivalent diameter and area in thin section. Values are given in μm for equivalent diameter and in μm² for area.

Thin section	Mean	Median	Mode
Equivalent diameter [μm]	261	218	109
Area [μm²]	$7.6 \cdot 10^4$	$3.7 \cdot 10^4$	$9.3 \cdot 10^3$

Most of the particles have an equivalent diameter smaller than 750 μm, as shown by the curve of the distribution (Figure 27). The peak of 425 particles at 200 μm recalls the mode value, however, the difference between the calculated value and the peak is due to the size of the bins. A close-up with smaller size bins provides a more precise peak at 170 μm, closer to the mode value. The drop-off for small sizes could be due to incomplete data acquisition of smaller particle size, but that is unlikely as particles as small as 24 μm were measured, therefore it is probably real and not an artefact of the data. Few particles have an equivalent diameter larger than 750 μm. The largest particle has an equivalent diameter of 2173 μm (the large yellow particle, Figure 21).

The mean, median and mode particle area in the thin section are shown in Table 1. The mean and the median have a 50% difference which shows that the mean is strongly influenced by the large particles. The modal size represents less than 25% of the mean or median.
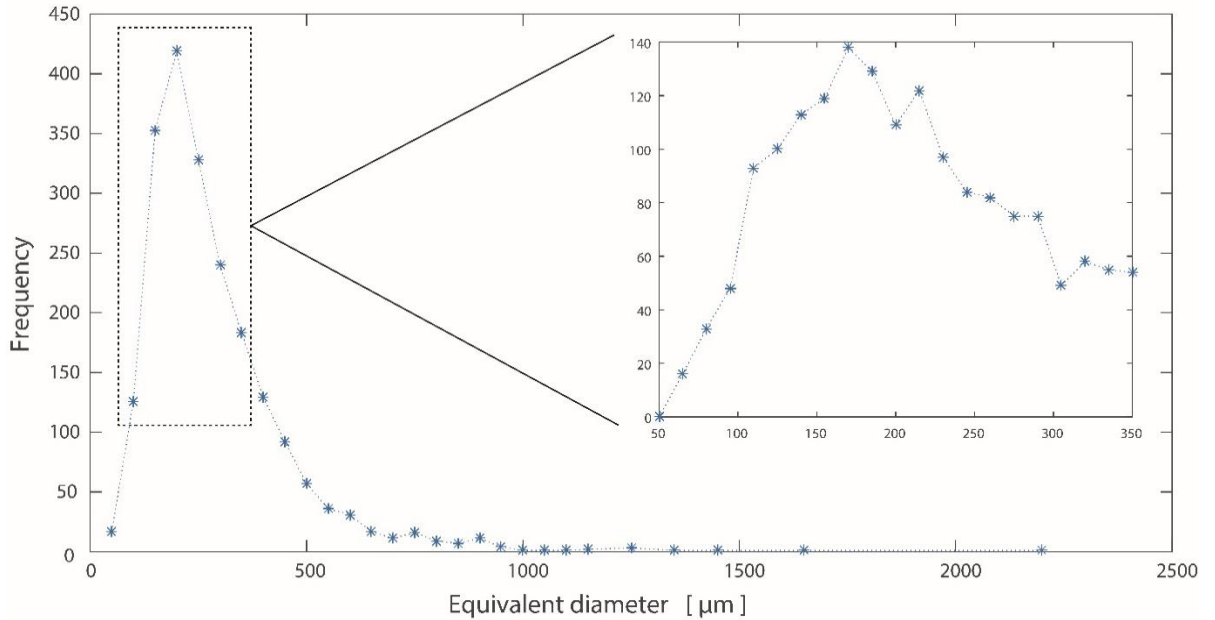
Figure 27 – Equivalent diameter histogram of particles in the thin section. X axis is equivalent diameter in μm and Y axis is frequency. The histogram was constructed using size bins of 50 μm. The close-up of the peak is a histogram constructed using size bins of 15 μm.

Most of the particles have an area below $0.5 \cdot 10^6$ μm^2 (Figure 28), and the distribution has a peak of 184 particles around $0.2 \cdot 10^4$ μm^2 which recalls the mode (Table 1). The mode value appears higher in the histogram due to the size of the bins (5000 μm^2). There are only few particles larger than $0.5 \cdot 10^6$ μm^2: particles spread out until $1.55 \cdot 10^6$ μm^2, with an outlier at $3.7 \cdot 10^6$ μm^2 which belong to same large particle (Figure 21).
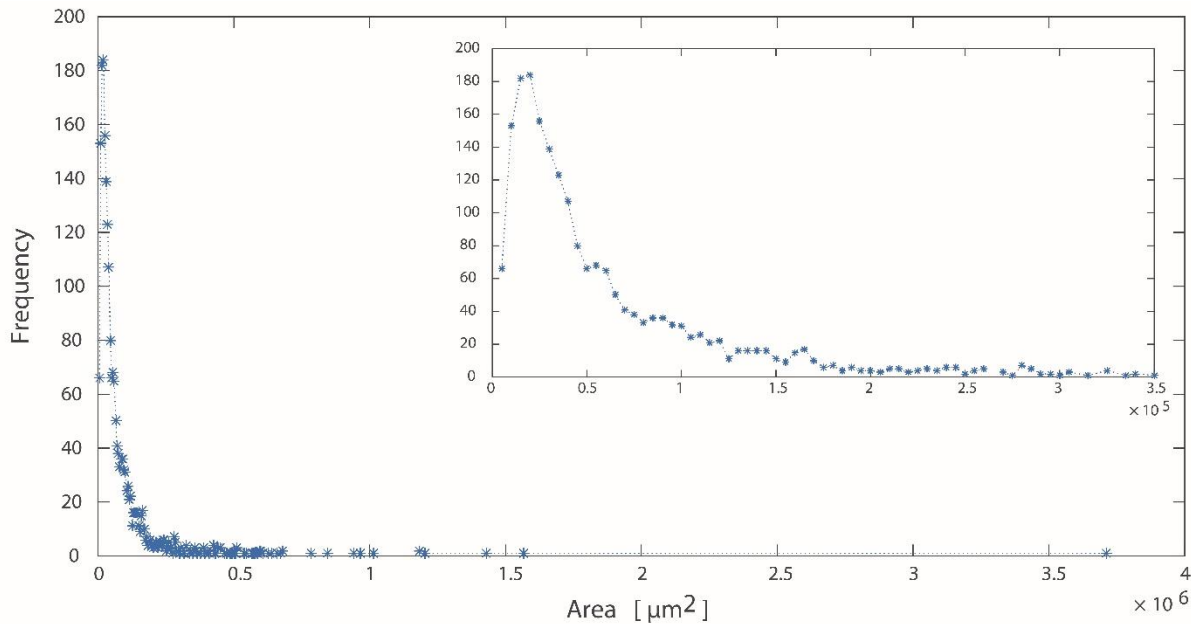
Figure 28 – Particle area histogram of thin section. X axis is area in μm^2 and Y axis is particle frequency. The histogram was constructed using size bins of 5000 μm^2.

The mean, median and mode equivalent diameter and area values for the tomography slice are given

in Table 2. Due to the 2D nature of the tomography slice, these diameters are essentially intersection

diameters of the crystals in 3D.

Table 2: Quantitative evaluation of particle equivalent diameter and area in tomography slice.
Values are given in μm for equivalent diameter and in μm² for area.

Tomography slice	Mean	Median	Mode
Equivalent diameter [μm]	362	311	16
Area [μm²]	$1.6 \cdot 10^5$	$7.6 \cdot 10^4$	197

The mean and the median equivalent diameter in the tomography slice have a difference of 14%, a small

difference that shows the mean is weakly influenced by the large particles (Table 2). The equivalent

diameter mode is very small compared to the mean and median values for the tomography slice.

The equivalent diameter histogram shows that the tomography slice has a high frequency of small

equivalent diameters, the most common being ≤ 50 μm, the smallest size bin in the histogram (Figure

29). Particle frequency decreases with increasing size for the tomography slice.
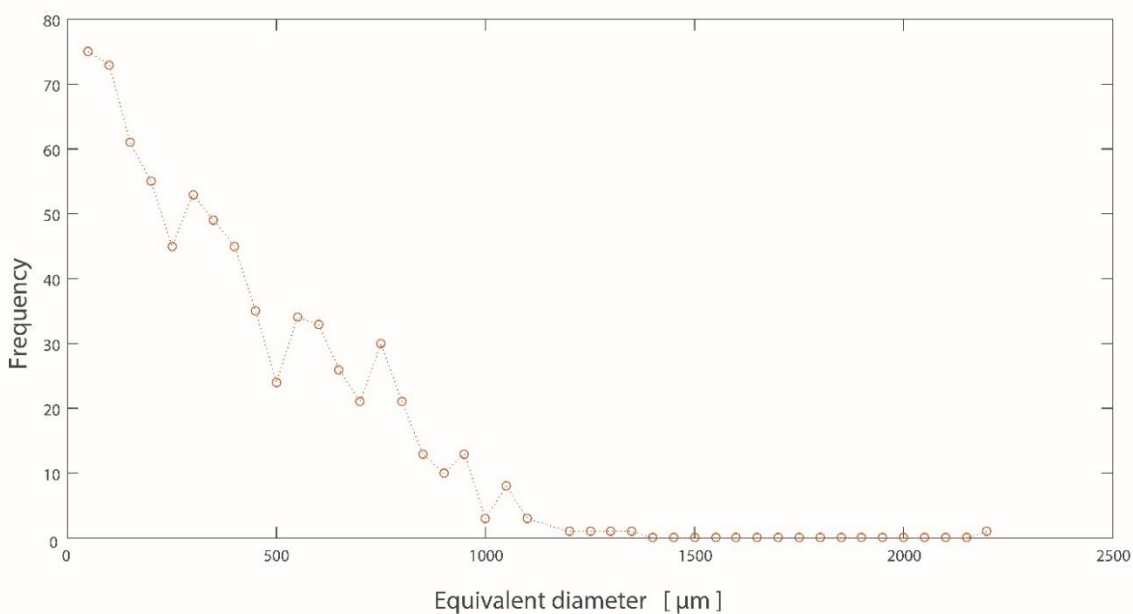
Figure 29 – Equivalent diameter histogram of particles in the tomography slice. X axis is
equivalent diameter in μm and Y axis is frequency. The histogram was constructed using size
bins of 50 μm.

The mean and the median particle area in the tomography slice have a difference of 54%, which is due to the influence of the large particles on the mean (Table 2). The mode of the area is noticeably smaller compared to the mean and median values for the tomography slice (up to 100% smaller).

The tomography slice has a high frequency of small particles, with the highest frequency for areas ≤ 5000 μm² (Figure 30), correlating well with the mode (Table 2). Particle frequency rapidly decreases with increasing particle area; the majority of particles have an area smaller than $1.5 \cdot 10^5$ μm². There is a local maximum at areas of 15000 μm² (close-up, Figure 30).
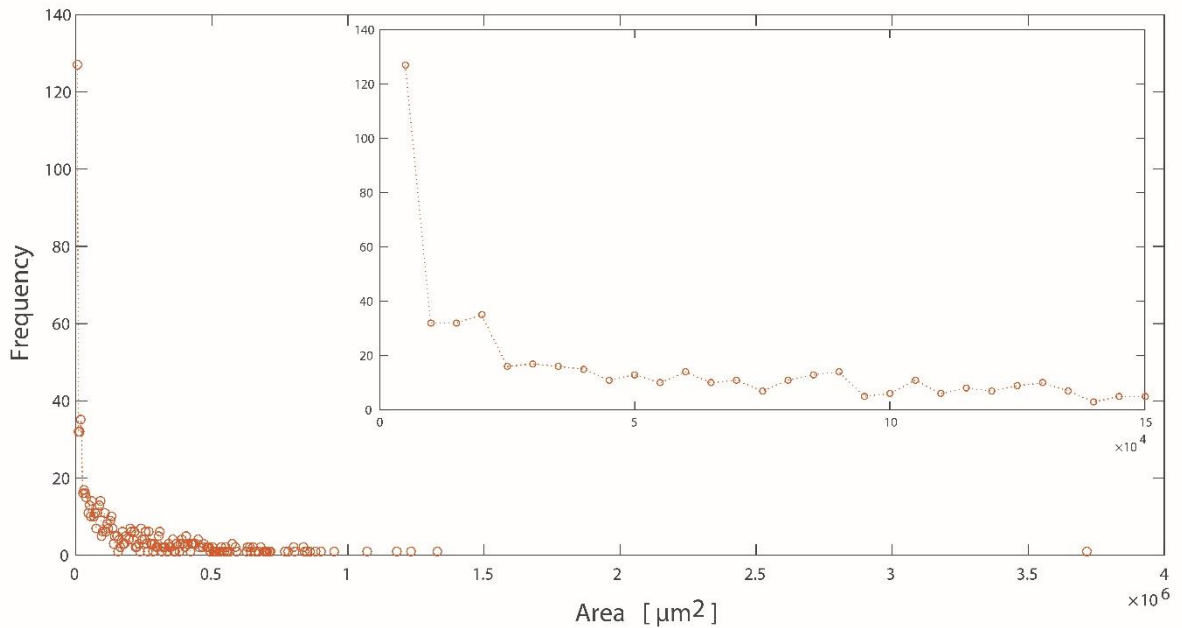
Figure 30 – Particle area histogram of tomography slice. X axis is area in μm² and Y axis is particle frequency. The histogram was constructed using size bins of 5000 μm².

4.2.1.3   Comparison of thin section & tomography slice

The thin section contains 2098 particles whereas the tomography slice contains only 735. The mean equivalent diameter in the thin section is lower than the tomography slice by 28%. The median value for the thin section is 30% lower than the tomography slice median. The difference in mode of the particle equivalent diameter is the biggest: the thin section mode is 71% higher than the tomography slice (Table 3).

Equivalent diameter [μm]	Mean	Median	Mode
Thin section	261	218	109
Tomography slice	362	311	16

The equivalent diameter histogram comparing the thin section and the tomography slice shows a steady decrease in particle frequency with increasing particle size for the tomography slice whereas the distribution for the thin section data is different with a peak for particles of 200 μm (Figure 31). For diameters higher than 550 μm, the two trends experience the same decrease in particle frequency as particle diameter increases.
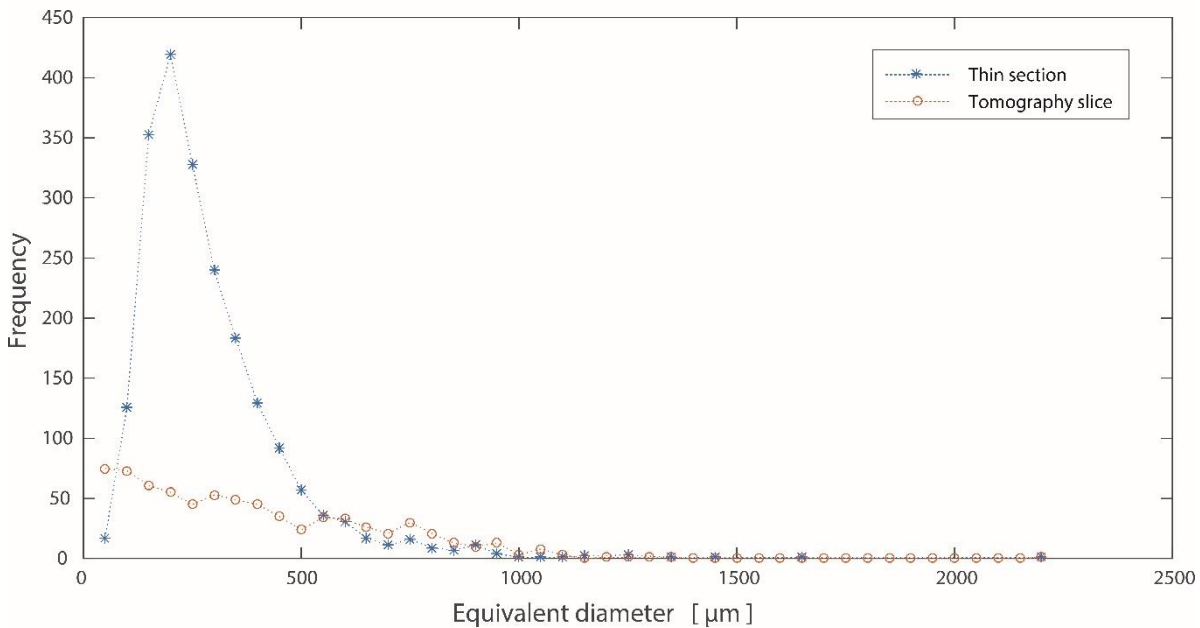
Figure 31 – Equivalent diameter histogram of particles in the thin section and the tomography slice. X axis is equivalent diameter in μm and Y axis is frequency. The histogram was constructed using size bins of 50 μm.

The mean area in the tomography slice is twice as large as the thin section (54%) and the median area in the thin section is half that of the tomography slice (Table 4). The thin section modal area is 50 times higher than that of the tomography slice. The total area in the thin section is $1.60 \cdot 10^8 \mu m^2$ whereas the tomography slice total area is $1.21 \cdot 10^8 \ \mu m^2$. The difference means that there is 24% of the area missing in the tomography slice.

Area [μm²]	Mean	Median	Mode	Total
Thin section	$7.6 \cdot 10^4$	$3.7 \cdot 10^4$	$9.3 \cdot 10^3$	$1.60 \cdot 10^8$
Tomography slice	$1.6 \cdot 10^5$	$7.6 \cdot 10^4$	197	$1.21 \cdot 10^8$

The histogram below shows the differences in area distribution in the sample for both thin section and tomography slice (Figure 32). The narrow bell-shaped curve for the thin section, not observed in the tomography slice, has a peak at 15000 μm², the same area as the local maxima observed in the tomography slice. This area reflects the mode area of the thin section particles, although slightly higher due to the discrete area bins for the histogram. The rapid frequency decrease for increasing area is similar to the tomography slice.
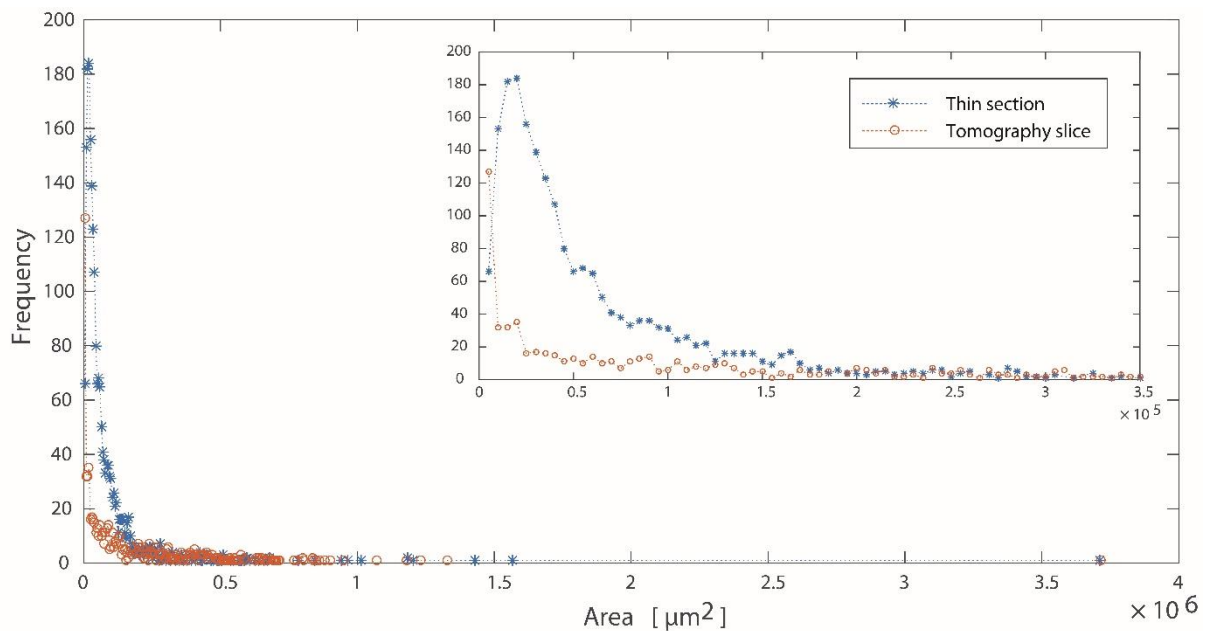
Figure 32 – Particle area histogram of thin section and tomography slice. X axis is area in μm² and Y axis is particle frequency. The histogram was constructed using size bins of 5000 μm². The close-up has the same size bins.

4.2.2 Crystal size distribution

Based on the frequency distribution of the size of the crystals (CSD), the crystal size distribution provides insight into the crystallisation history (see section 2.2.1).

4.2.2.1   Thin Section

The CSD of the thin section particles resembles a log-normal distribution (Figure 33). The peak in the distribution matches the mode of the equivalent diameter (~200 μm, Table 1). The subsequent decrease in frequency for increasing particle size flattens out for equivalent diameters of 1000 μm. As mentioned for Figure 27, the drop-off for small sizes is probably real and unlikely an artefact of the data due to incomplete data acquisition of smaller particle size, as particles as small as 24 μm were measured. For particles larger than 700 μm, the size distribution becomes noisy, with fluctuations only slightly bigger than the error bars. There are few large particles, with one outlier at 2173 μm (large yellow particle, Figure 21). The confidence intervals at 95%, illustrated by the error bars are small for small particles and increase in size for larger particles.
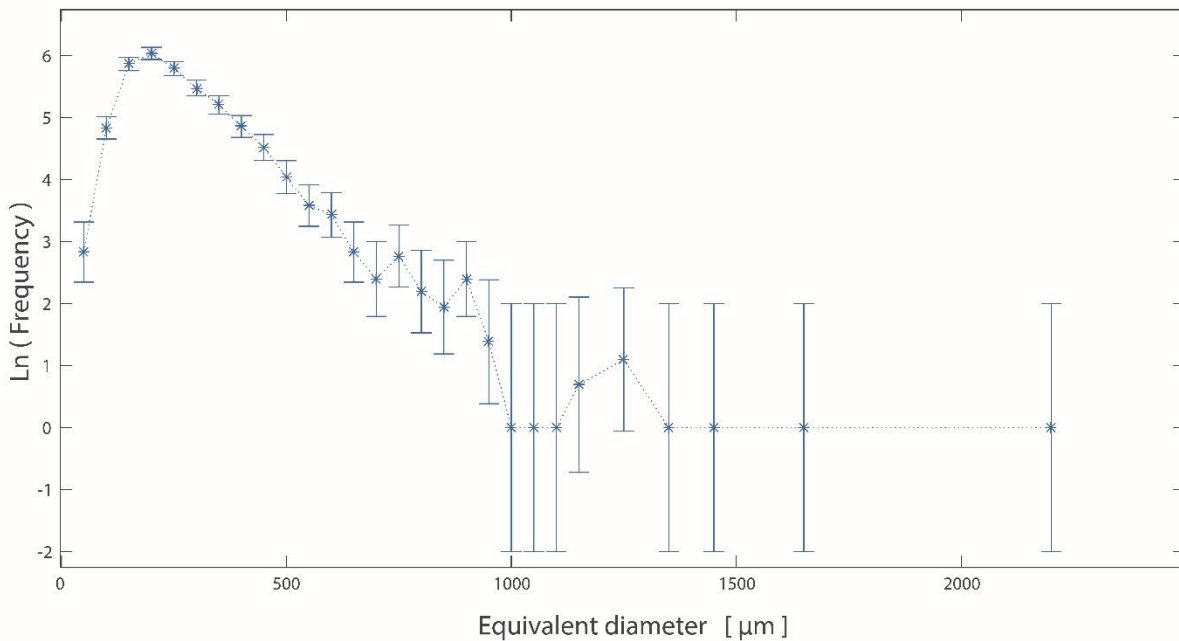
Figure 33 – Crystal size distribution particles in the thin section. The size of the particles was evaluated using equivalent diameter. X axis is equivalent diameter in μm and Y is the logarithm of the frequency. The error bars correspond to confidence intervals of 95%.

4.2.2.2   Tomography Slice

The CSD of the particles in the tomography slice resembles a negative asymptote distribution (Figure 34). The peak in the distribution matches the mode of the equivalent diameter (< 50 μm, Table 2) and then particle number decreases in frequency for increasing particle size to flatten out for equivalent diameters of 1150 μm. There are few large particles, with one outlier at 2173 μm (large green particle,

Figure 25). The confidence intervals at 95%, illustrated by the error bars are small for small particles and increase in size for larger particles.
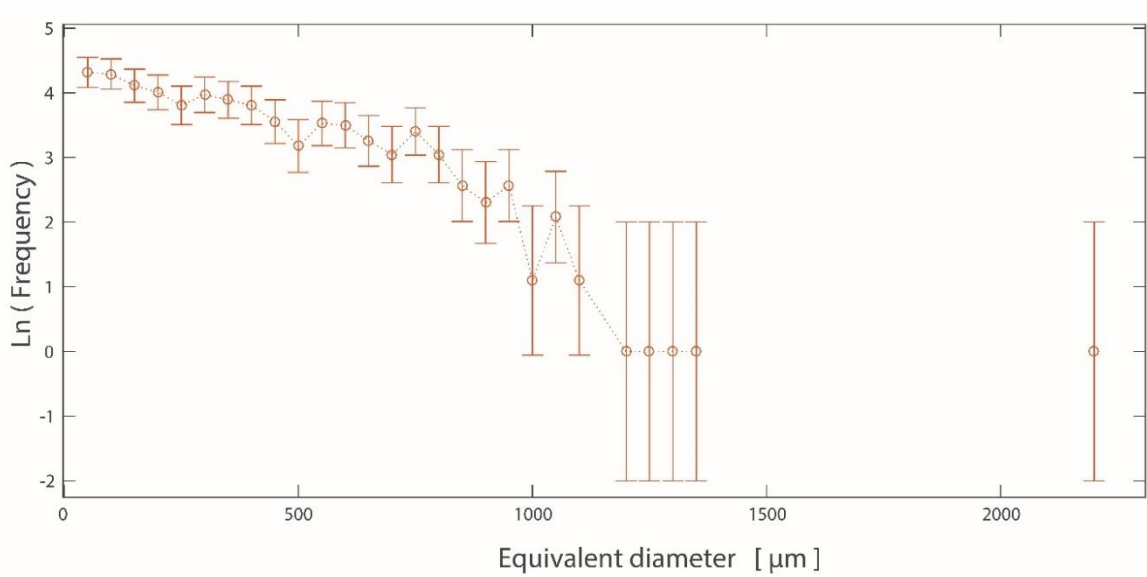
Figure 34 – Crystal size distribution particles in the tomography slice. The size of the particles was evaluated using equivalent diameter. X axis is equivalent diameter in µm and Y is the logarithm of the frequency. The error bars correspond to confidence intervals of 95%.

4.2.2.3   Comparison of thin section & tomography slice
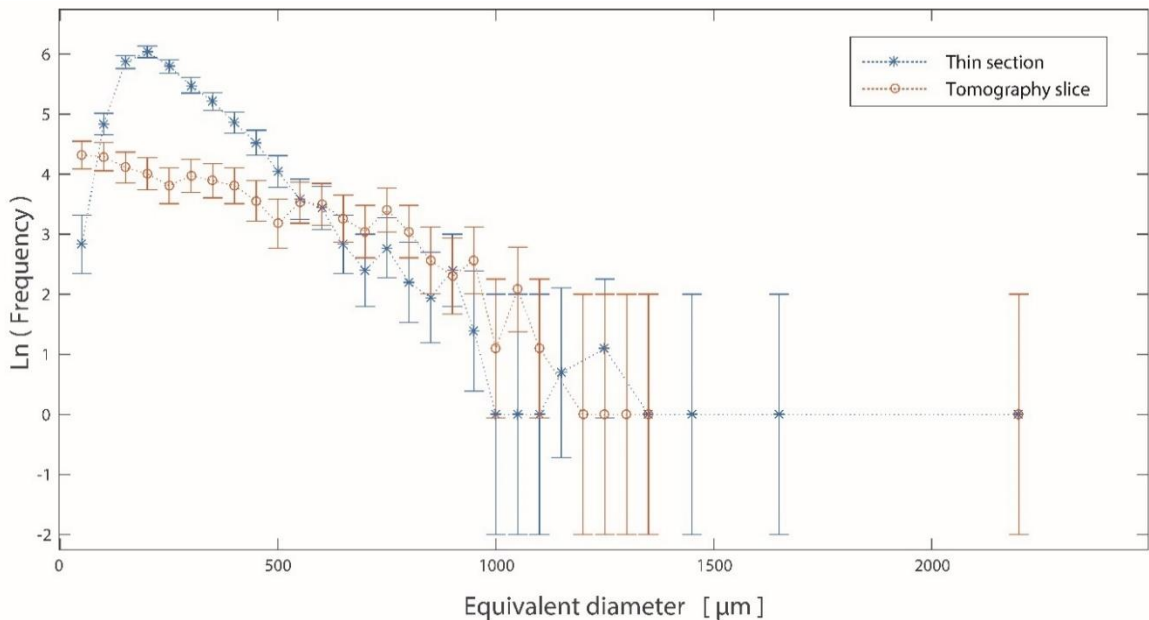
Figure 35 – Crystal size distribution of particles in the thin section and the tomography slice. The size of the particles was evaluated using equivalent diameter. X axis is equivalent diameter in µm and Y is the logarithm of the frequency. The error bars correspond to confidence intervals of 95%.

The thin section CSD and the tomography slice CSD have similar slopes, but the amplitude of the tomography slice CSD is shifted toward higher frequencies (Figure 35). The y-intercept for the

tomography slice is above 4 whereas the y-intercept is below 3 for the thin section maximum. The shape of the trends varies: the tomography slice CSD does not have the same peak at 200 μm as the thin section CSD but instead has a constant decrease of frequencies with an increase in size (Figure 35).
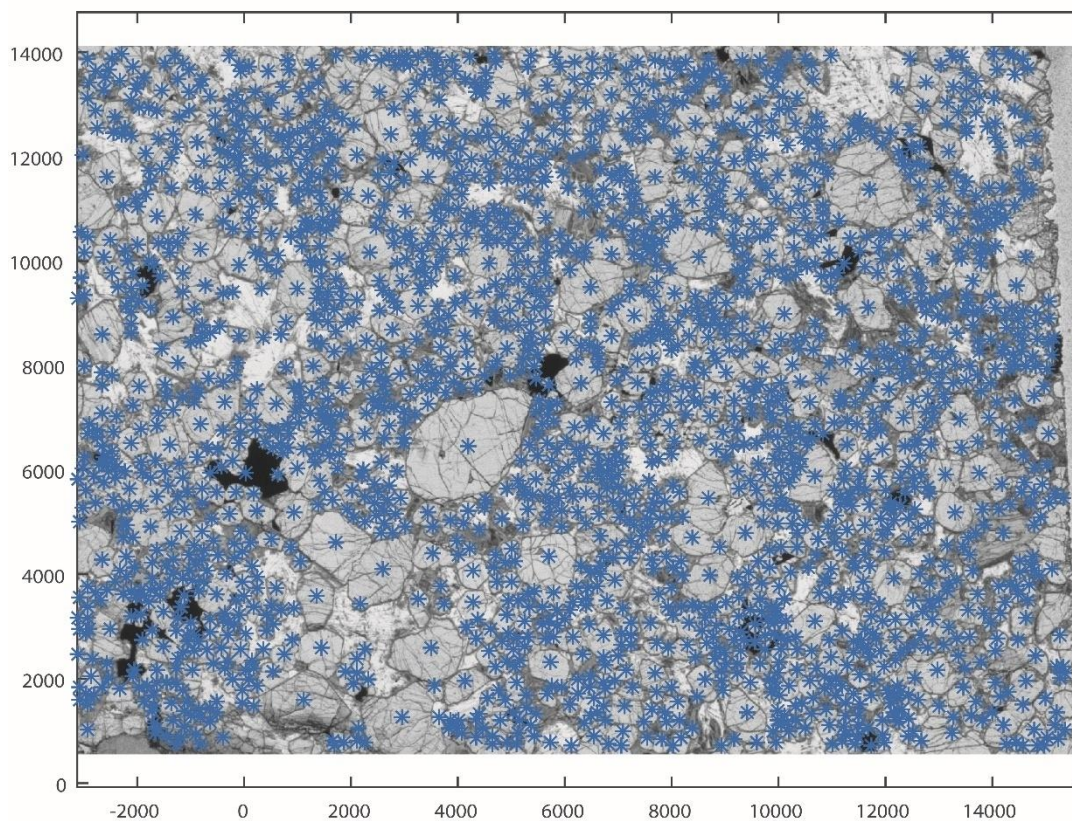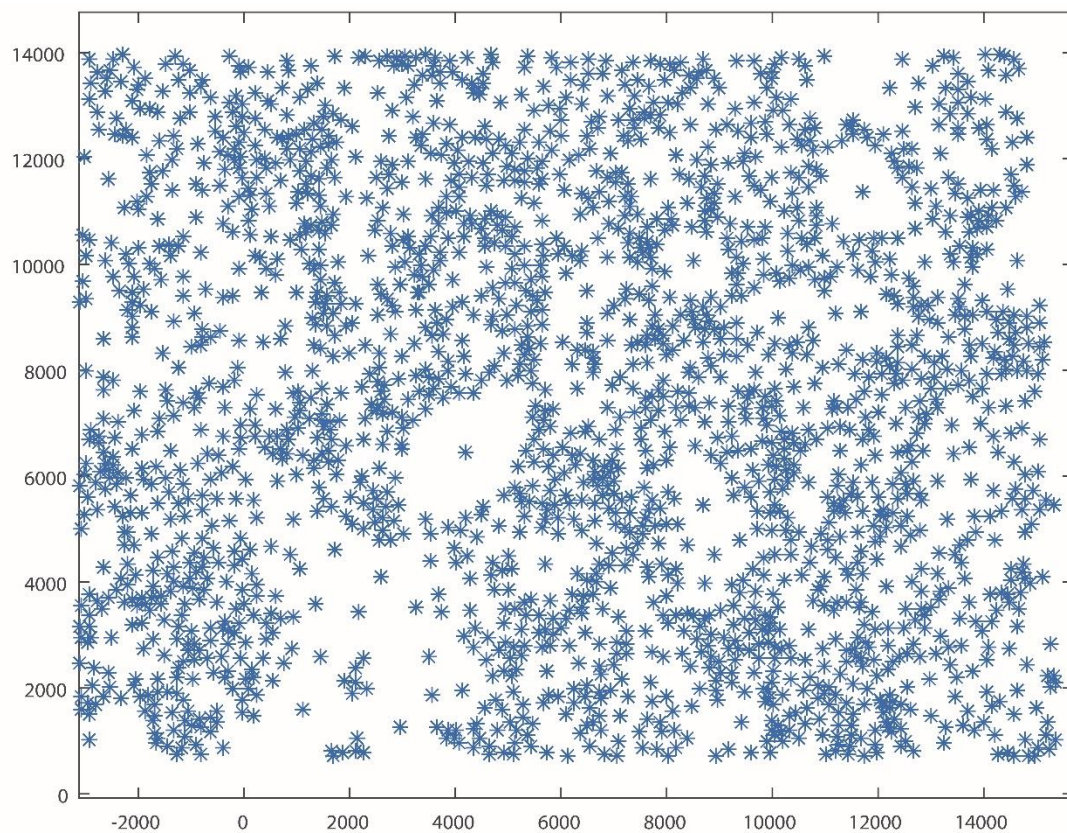
For particles with an equivalent diameter smaller than 1150 µm, the tomography slice CSD has higher frequencies than the thin section CSD, meaning there are more particles ranging from 0 to 1150 µm in the tomography slice than in the thin section. For particles larger than 1150 µm, the CSD trends become similar. The frequency of large particles in both thin section and tomography is similar.

4.2.3   Spatial distribution

4.2.3.1   Thin Section

Plotting particle barycentre location, and subsequently particle area, characterises the spatial distribution of particles throughout the sample.

The spatial distribution of the particles in the thin section is heterogeneous (Figure 36, top). Regions where the barycentre locations are densely packed (Figure 37, A) correspond to small, closely grouped particles (Figure 37, B). The less dense areas are characteristic of larger particles (Figure 37, C and D). The barycentre position map, however, does not take into account the area of the particles and could cause denser regions to be interpreted as clustering when they are in fact just a collection of small particles (Figure 37, A and B). Ordered barycentres of small particles can physically be closer than for large clustered particles (Figure 37, C and D). This visualisation method is useful for determining and comparing the spatial distribution of particles, but not the clustering or ordering.
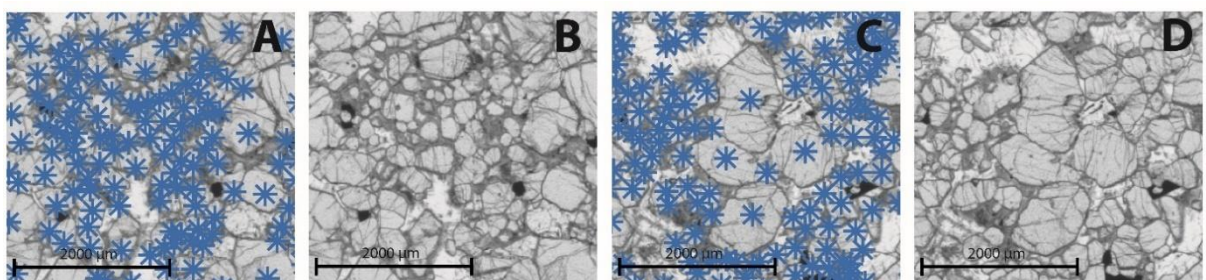
Figure 37 – Close up of olivine textures characterised by particles barycentre density. The images are in pairs, the left one with barycentre location and the right one only the thin section. A and B: Dense cloud of barycentre locations belonging to an accumulation of small crystals. C and D: sparse barycentre locations, belonging to large olivine crystals clumped together.

To better understand the textures, the area is plotted on each corresponding barycentre in Figure 38, by drawing circles of a radius proportional to the area centred on each barycentre. This provides a better

view of the spatial distribution of the size of the particles in the sample. All but the largest particles seem

evenly distributed in the sample (Figure 38). There are instances of large particles
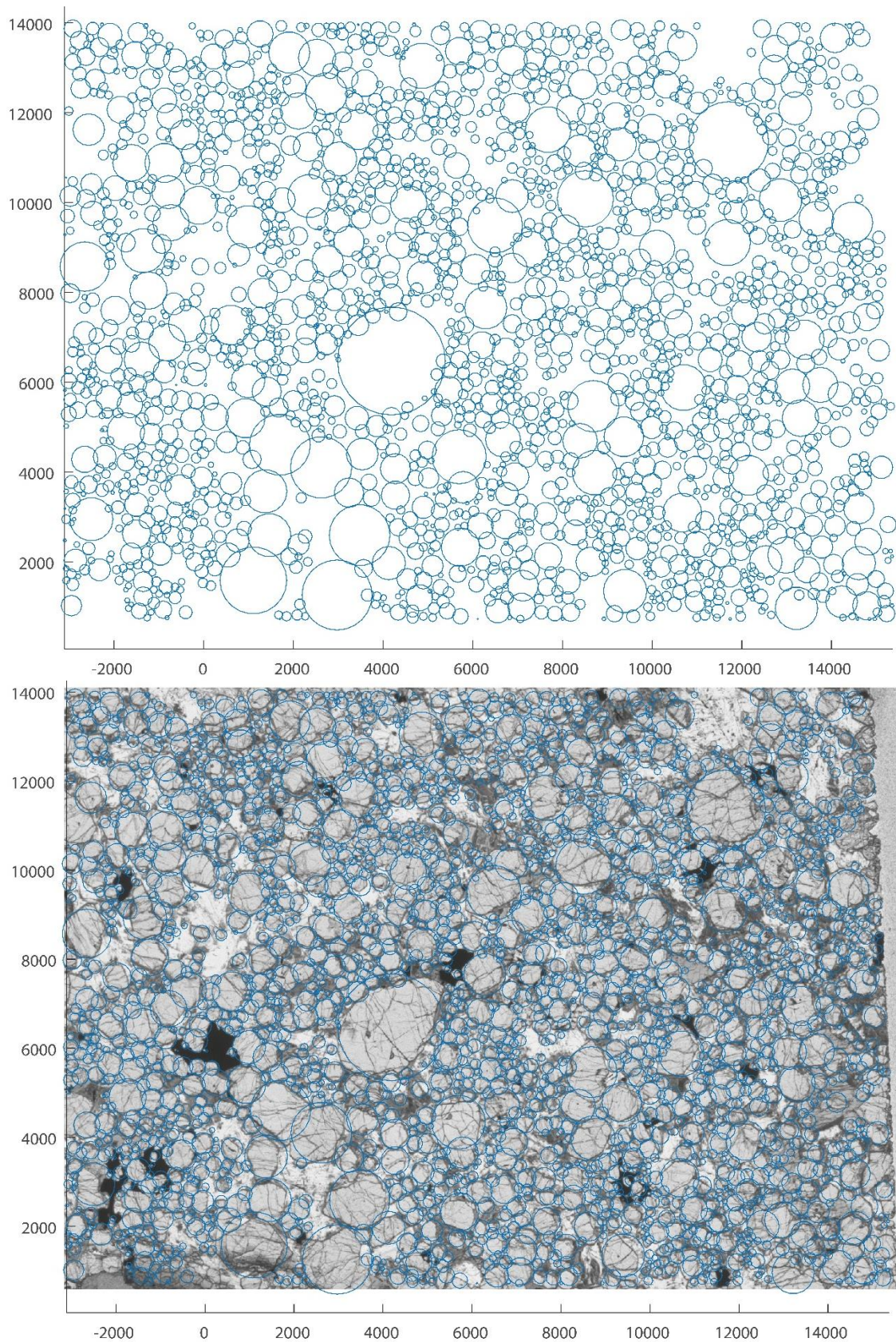
Figure 38 – Top: Area map for particles in the thin section. The circles are of diameter proportional to their area and are centred in their barycentre. X and Y axis are coordinates in μm. Bottom: area map over thin section scan to better associate the area spatial distribution with the olivine textures.

clumped with particles of similar size (e.g. Figure 39, A and B), but mostly, the large particles are found

in close proximity to medium to small-sized particles (Figure 39, C and D). The small particles are often

found surrounding larger ones (Figure 38).
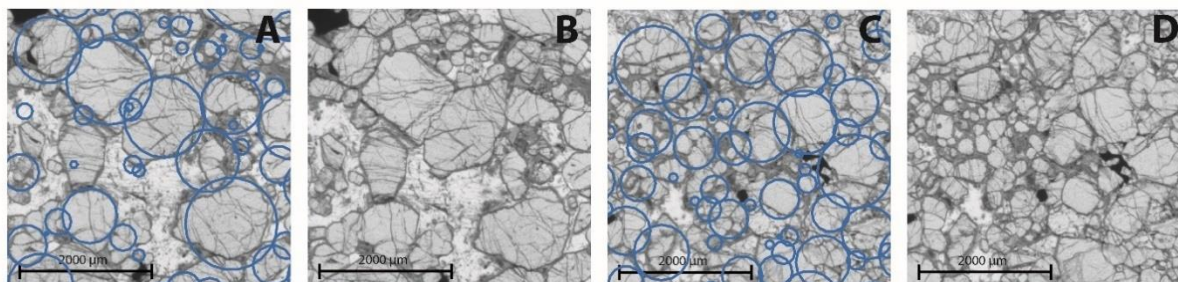
Figure 39 – Close up of thin section textures characterised by particle area density. The images are in pairs, the left one with the area map over it and the right, only the thin section scan. A and B: Dense association of large areas, belonging to clumped large olivine crystals. C and D: Large areas in association with small areas belonging to small olivine crystals agglomerating around larger olivine crystals.

4.2.3.2   Tomography Slice
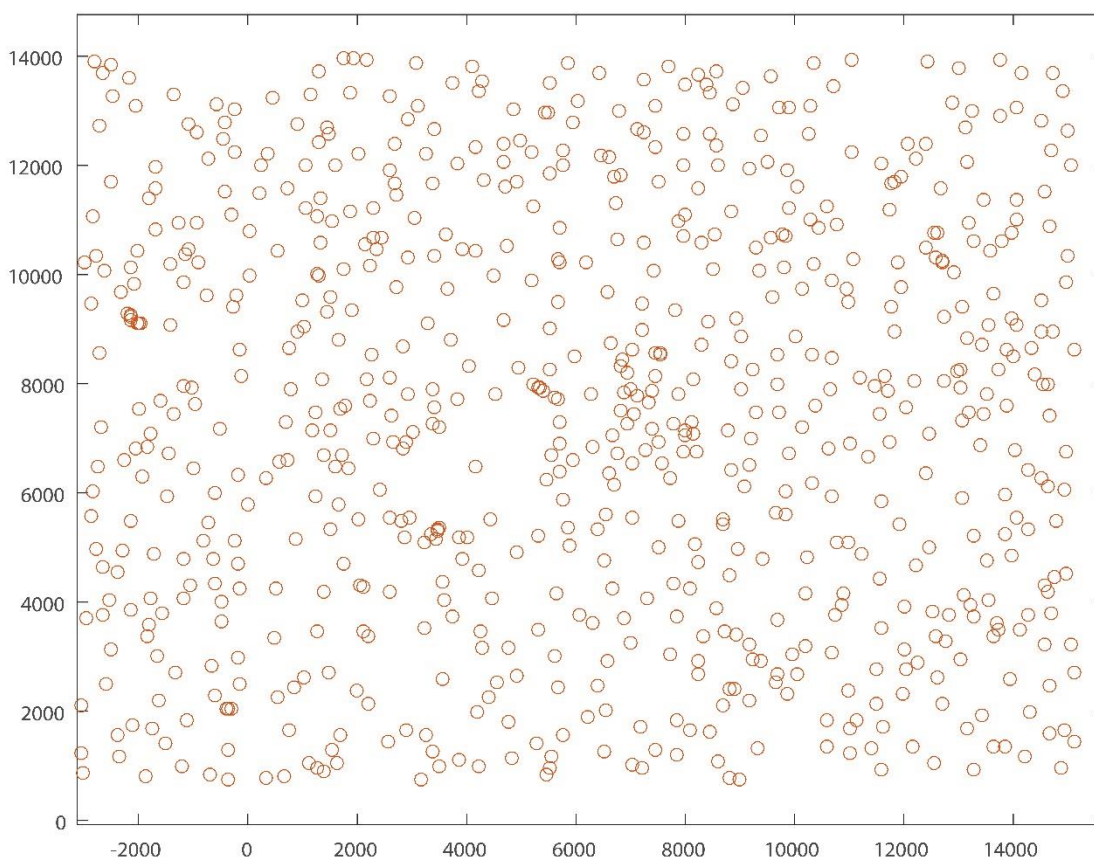
Figure 40 – Barycentre location in the tomography slice. X and Y axis are spatial coordinates in μm. Each circle represents a particle but is however not indicative of the area.

The spatial distribution of the particles in the tomography slice is globally even (Figure 40 and Figure

41). There are instances of denser populations of barycentre (Figure 42, A). These denser regions

correspond to small clustered particles (Figure 42, B). Less dense regions of barycentre locations are also present and translate to larger particles (Figure 42, C and D).

As mentioned above, the barycentre position map does not take into account the area of the particles. Hence, this visualisation method is useful for determining and comparing the spatial distribution of particles, but not the clustering or ordering.
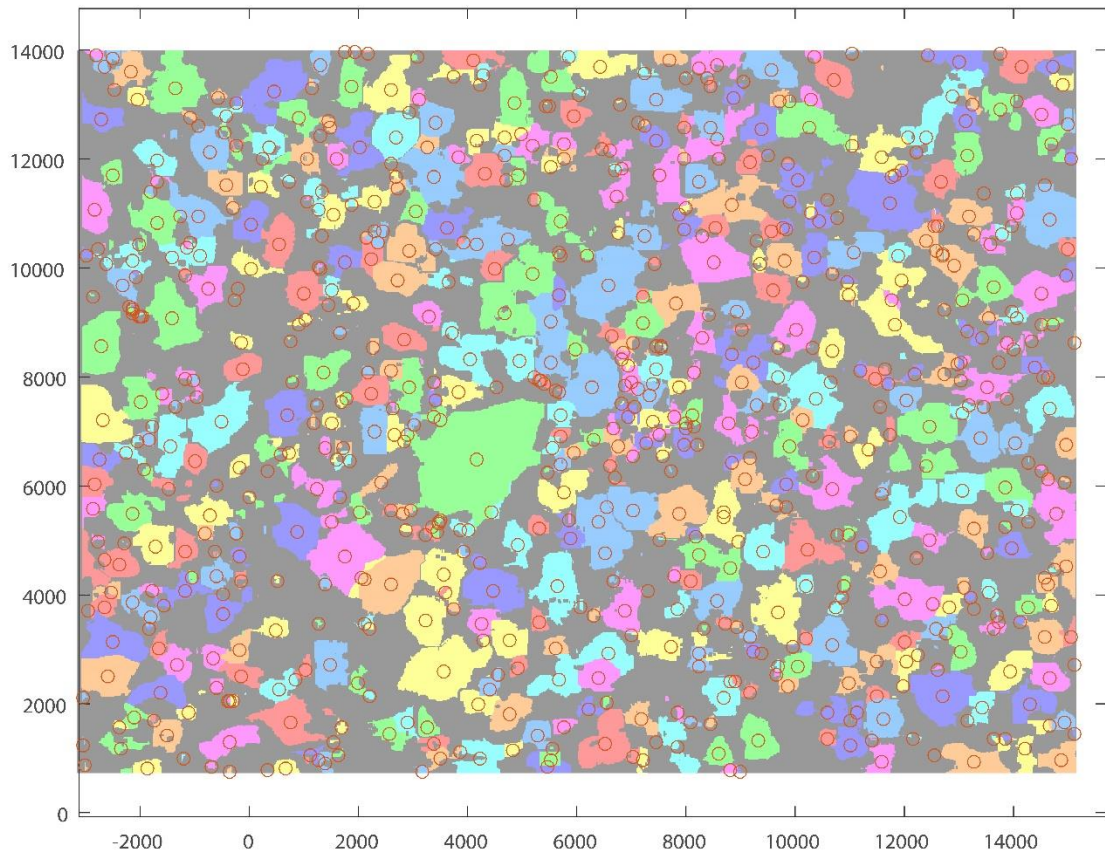
Figure 41 – Barycentre location in the tomography slice above the tomography slice. X and Y axis are spatial coordinates, in µm. Each circle represents a particle but is however not indicative of the area.
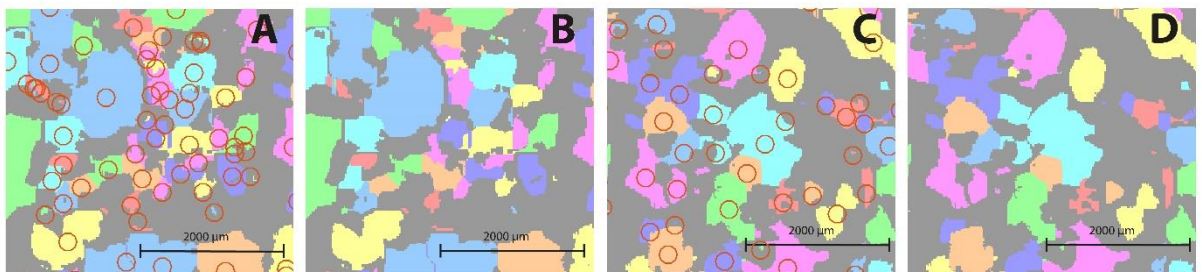
Figure 42 – Close up of olivine textures characterised by particles barycentre density. The images are in pairs, the left one with barycentre location and the right one only the tomography slice. A and B: Dense cloud of barycentre locations belonging to an accumulation of small crystals. C and D: sparse barycentre locations, belonging to large olivine crystals clumped together.

To better understand the textures, the area is plotted on each corresponding barycentre in Figure 43, to provide a better view of the spatial distribution of the size of the particles in the sample. Except for

the largest particle, all large particles seem evenly distributed in the sample (Figure 43, top). The smaller

particles fill the gaps between the larger ones, their spatial distribution is, therefore, less even than for

the larger particles (Figure 43). The smaller particles are also often associated with larger particles
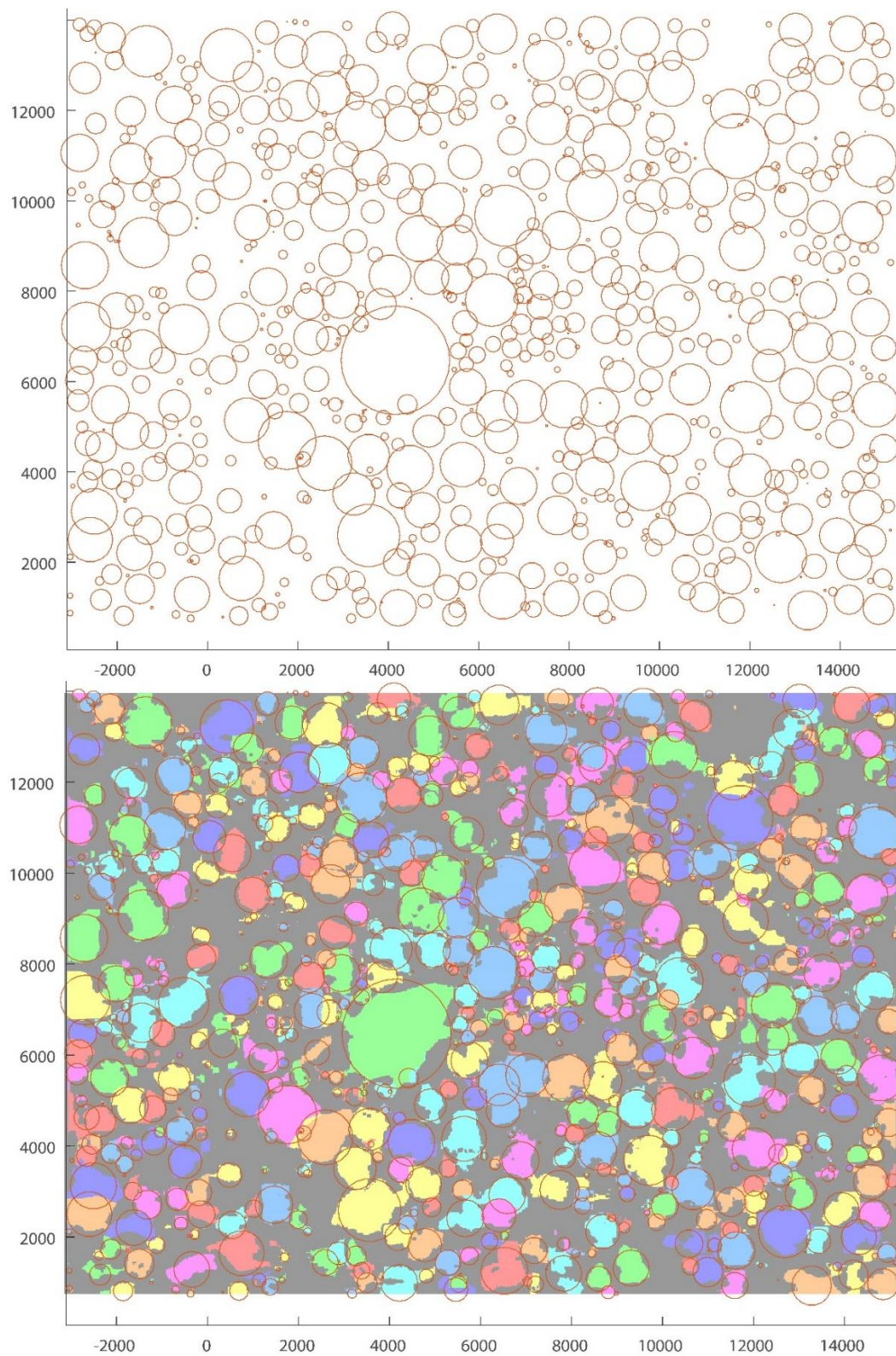
(Figure 43).

*Figure 43 – Top: Area map for particles in the tomography slice. The circles are of
diameter proportional to their area and are centred in their barycentre. X and Y axis are*

4.2.3.3   Comparison of thin section & tomography Slice

The thin section has 2098 particles compared to the 735 particles in the tomography slice (Figure 44). There is, however, a good correlation between barycentre locations in the thin section and the tomography slice for some particles (Figure 45, A). The barycentre locations almost overlap and when correlated back to the particles in the tomography slice and thin section, these correspond to medium to large particles (Figure 45, B and C). On the same Figure 45, the small particles in the thin section are not present in the tomography slice and the presence of "artificial" particles in the tomography slice that are not present in the thin section (two small orange circles in the centre of Figure 45, B).
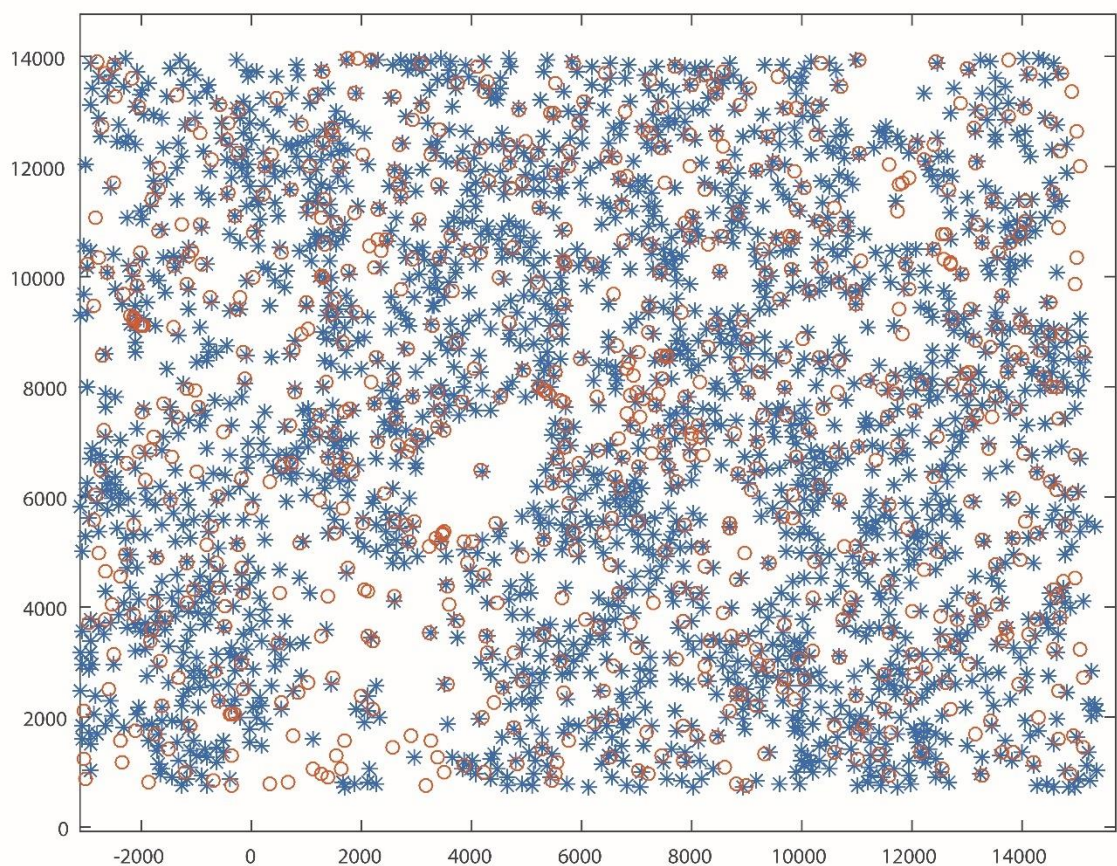
Figure 44 – Barycentre location for the thin section and tomography slice overlaid. The blue stars are the thin section and the orange circles are the tomography slice. X and Y axis are position in μm.
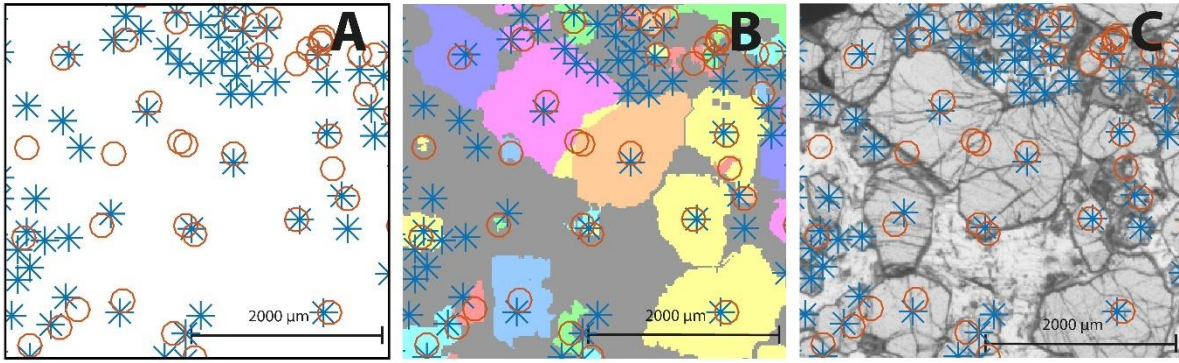
Figure 45 – Detail of barycentre location in the thin section and the tomography slice. A: comparison of barycentre location between the thin section and the tomography slice; B: Barycentre location and the tomography slice; C: barycentre location and the thin section scan.

Due to the difference in particle number between the thin section and the tomography slice, many particles in the thin section do not have a direct representative in the tomography slice. There are groups of particles in the tomography slice that only have one direct equivalent in the thin section (Figure 46, A, B and C). Figure 46 1a and 1b are one example of such occurrence: the angular particle from the thin section (outlined in Figure 46, 1a) is broken up too much in the tomography slice (Figure 46, 1b). Such occurrences of over separation can be linked back to angular particles in the thin section. The opposite texture, one particle in the tomography corresponding to several in the thin section, is also present (Figure 46, 2a and 2b). A close group of sub-angular particles in the thin section (outlined and highlighted in Figure 46, 2a) are represented as only one particle in the tomography (Figure 46, 2b). This occurrence is specific to tight clusters of particles in the thin section, typical of crystals that have grown against each other, like annealed crystals.
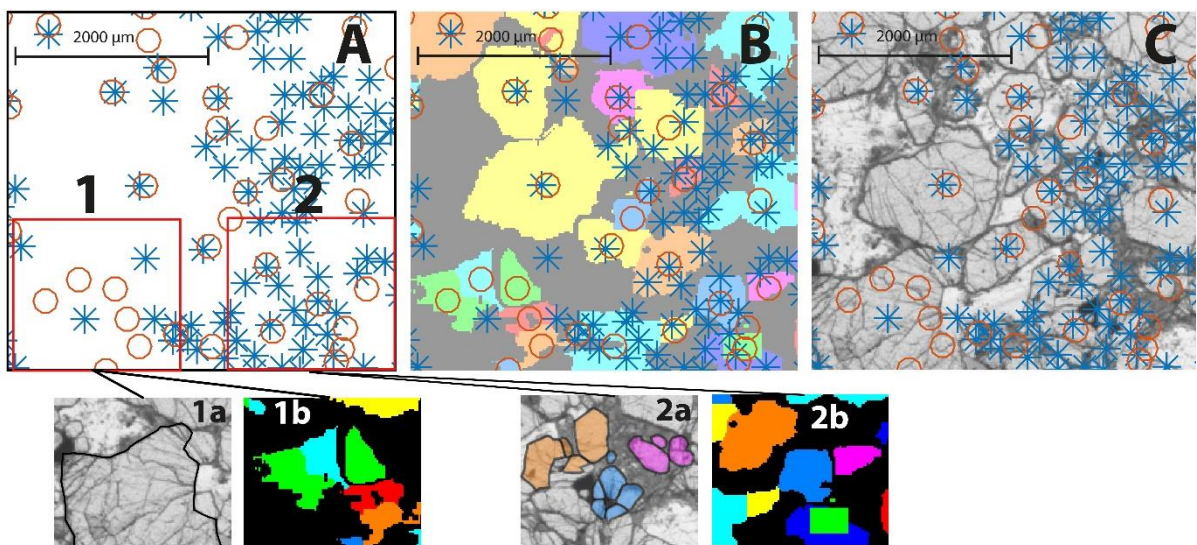
Figure 46 – Detail of barycentre location in the thin section and the tomography slice. A: comparison of barycentre location between the thin section and the tomography slice; 1a and b: an example of over-separation in the tomography data; 2a and b: an example of under-separation in the tomography data; B: Barycentre location and the tomography slice; C: barycentre location and the thin section scan.

87

Using the *nncross* function in R (cf. section 3.4.2.2), each particle in the tomography was assigned a nearest neighbour in the thin section. The particles from the tomography slice and their *nncross* nearest neighbour in the thin section are shown in Figure 47, where the arrow points to the *nncross* nearest neighbours in the thin section and the length of the arrow is indicative of the distance between the particles. Generally, these distances are small (modal distance is 80 µm, Figure 48). The longer arrows correspond to cases of over-separation in the tomography slice: several particles in the tomography slice corresponds to one particle in the thin section (e.g. Figure 46, 1a and 1b). Due to the difference in particle number in both data sets, many particles from the thin section are not paired up with any particle from the tomography slice.

○ Tomography slice △ Thin section
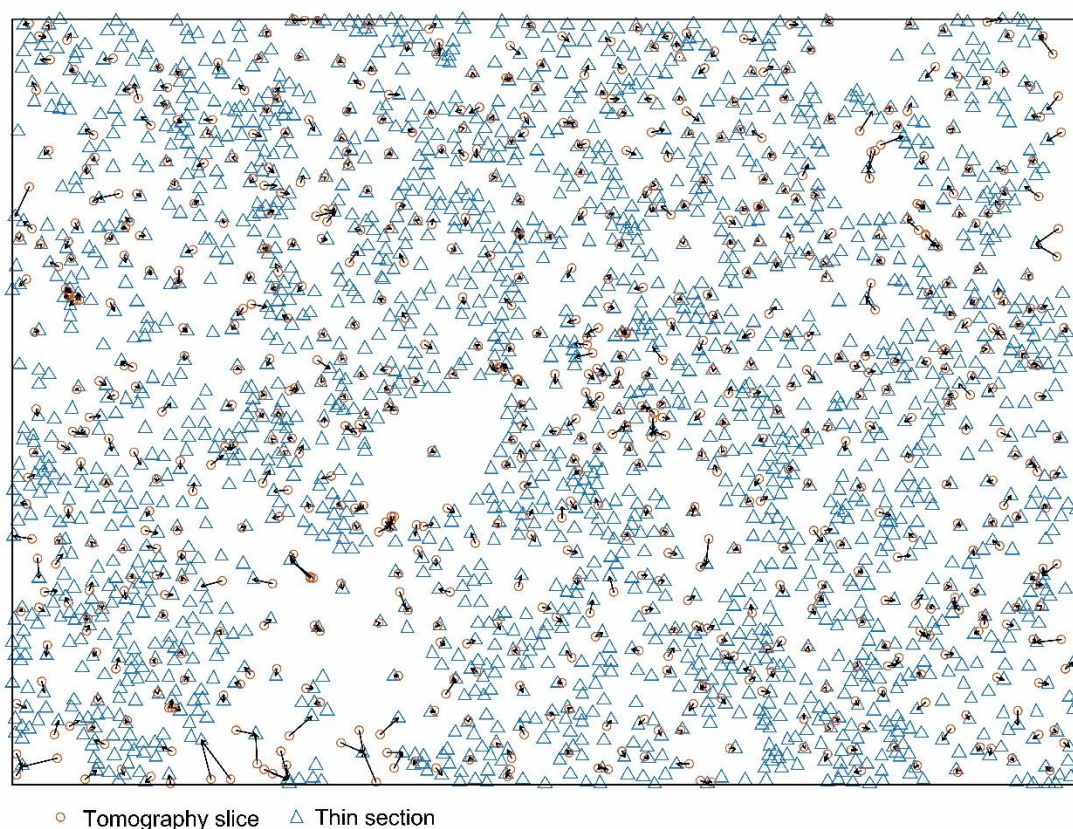
Figure 47 – Nncross nearest neighbour map. Blue triangles represent the thin section particles and orange circles are the tomography slice particles. The black arrows indicate the nncross nearest neighbour and the distance between them.
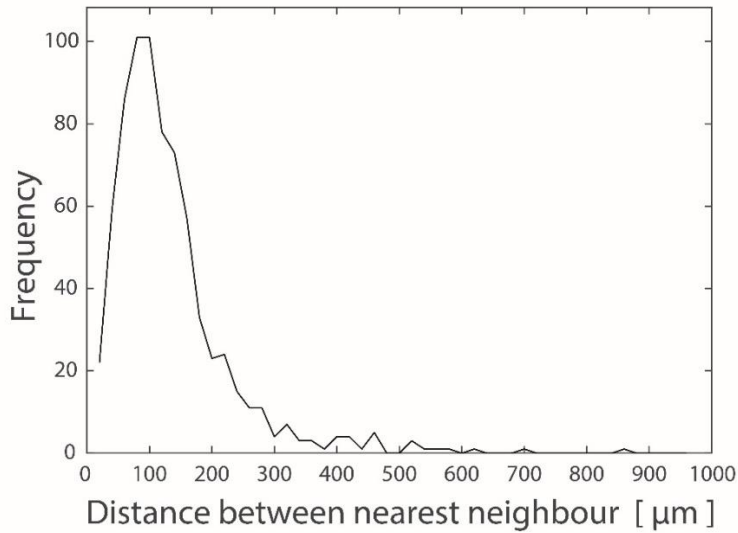
Figure 48 – Frequency histogram of the distance separating the nncross nearest neighbour particles in the thin section and tomography slice.

Quantitively, the distance between the *nncross* nearest neighbour pairs ranges from 0.71 to 843 µm, with a mode of 80 to 100 µm (Figure 48). The distance between the *nncross* nearest neighbours does not depend on the size of the particles.

The thin section particle area is compared to the tomography slice particle area in Figure 49. Visually, there is a good correlation between the areas in the tomography slice and thin section for the large particles. This same correlation was already observed in the particle barycentre map (Figure 44).
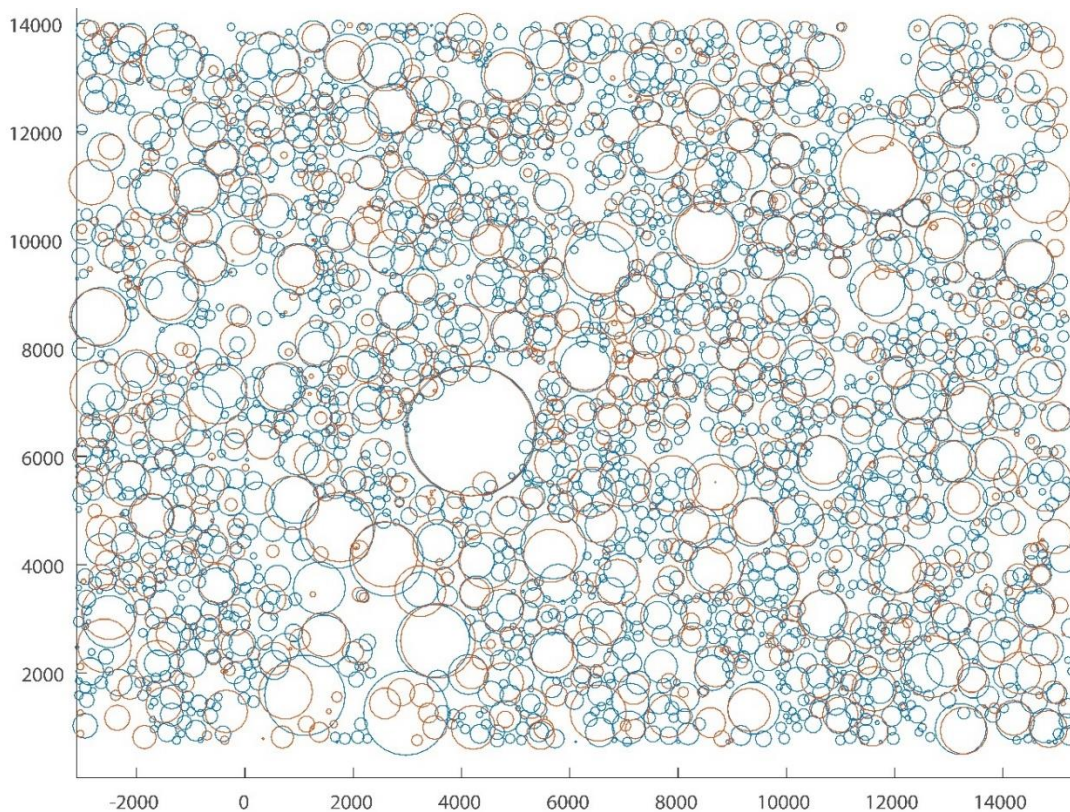
Figure 49 – Area map of the particles in both thin section (blue) and tomography slice (orange). The circles are centred on the barycentre of each particle and have a radius of the area. X and Y axes are position in space and are in µm.

The textures of one particle in the thin section being represented by several particles in the tomography slice and vice versa are also observed in the area map (Figure 50, textures highlighted in A, 1 and 2).
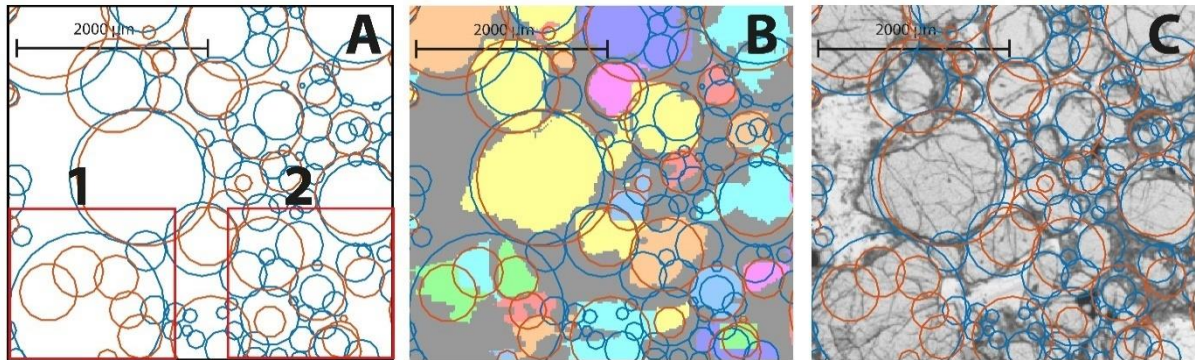
Figure 50 – Detail of particle area in the thin section and the tomography slice. A: comparison of particle area between the thin section and the tomography slice;1: an example of over-separation in the tomography data; 2: an example of under-separation in the tomography data; B: particle area and the tomography slice; C: particle area location and the thin section scan.

The area map of both thin section and tomography shows the small particles missing in the tomography slice. One category of these particles missing in the tomography slice is small particles agglomerated around larger ones (Figure 51, highlighted in A).
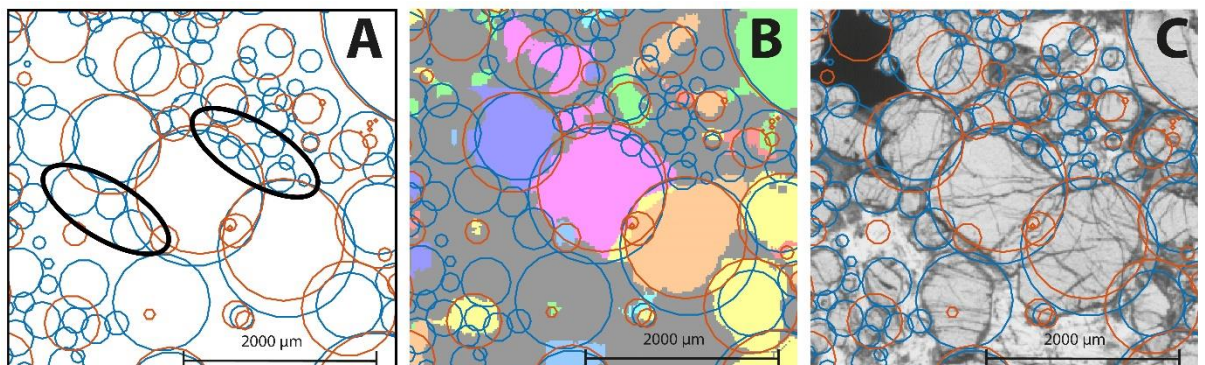
Figure 51 – Detail of particle area in the thin section and the tomography slice. A: comparison of particle area between the thin section and the tomography slice; B: particle area and the tomography slice; C: particle area and the thin section scan.

The other category is composed of small to medium particles in the thin section that fill up the space between the larger particles (Figure 52, highlighted in A). The highlighted particles are missing in the tomography (Figure 51, B) and correspond to small to medium particles in the thin section (Figure 52, C).
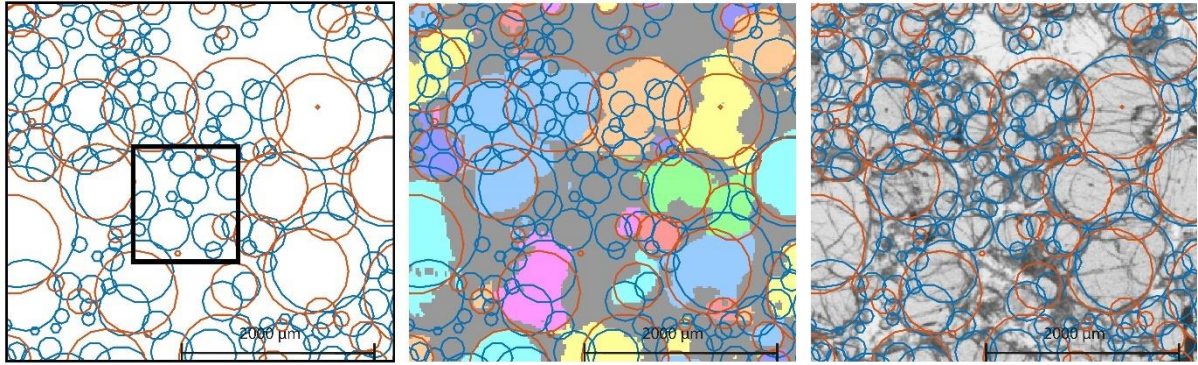
Figure 52 – Detail of particle area in the thin section and the tomography slice showing the small particles present in the thin section but missing in the tomography. A: comparison of particle area between the thin section and the tomography slice; B: particle area and the tomography slice; C: particle area and the thin section scan.

4.2.4   Packing and mush structure

To evaluate clustering and ordering in the 2D data, the pair correlation function, g(r), is used. It is a radial distribution function that calculates the probability of finding a particle in a given radius r. If g(r)>1, g(r)=1 being complete spatial randomness, the crystals in the sample are clustered and if g(r) < 1 the crystals are ordered. The pair correlation function is shown with its uncertainty envelopes representing 39 simulations of completely spatial randomness and thus confidence intervals of 95%.

4.2.4.1   Thin Section
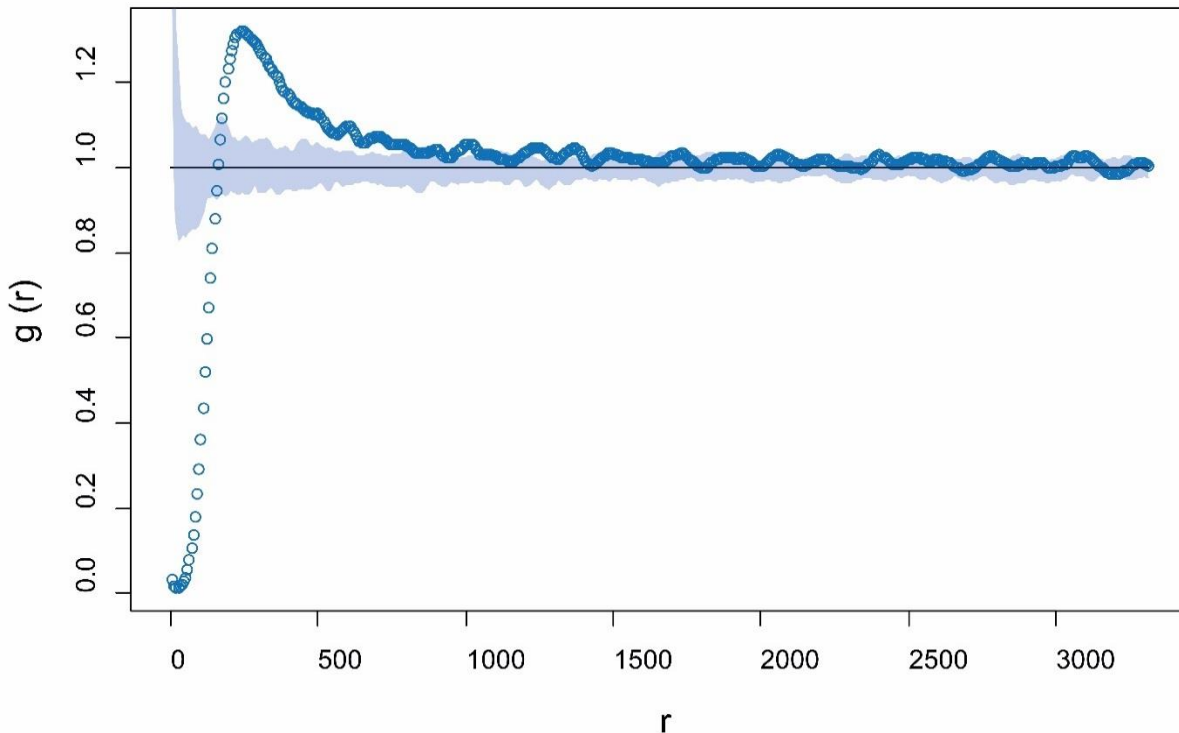
Figure 53 – Pair correlation function for the thin section. The function is represented by the small circles. The straight line at g(r)=1 corresponds to total spatial randomness and the lines around are the uncertainty envelopes. These correspond to 39 simulations of completely spatial randomness, representing, therefore, confidence intervals of 95%. X axis is the radius in μm and Y axis is the g(r) function.

The pair correlation function of the thin section is equal to 0 until r ~20 µm. g(r) increases rapidly to a peak of 1.35 around r = 250 µm and then continues with an undulating tail that loosely tends towards 1 (Figure 53). The peak is well defined and relatively narrow. The hardcore ranges from 0 to 200 µm but due to the polydispersity of the particle sizes, the values do not represent a true hardcore. The peak in the pair correlation function and subsequent undulations are statistically significant because they lie outside the uncertainty envelopes.

4.2.4.2   Tomography Slice
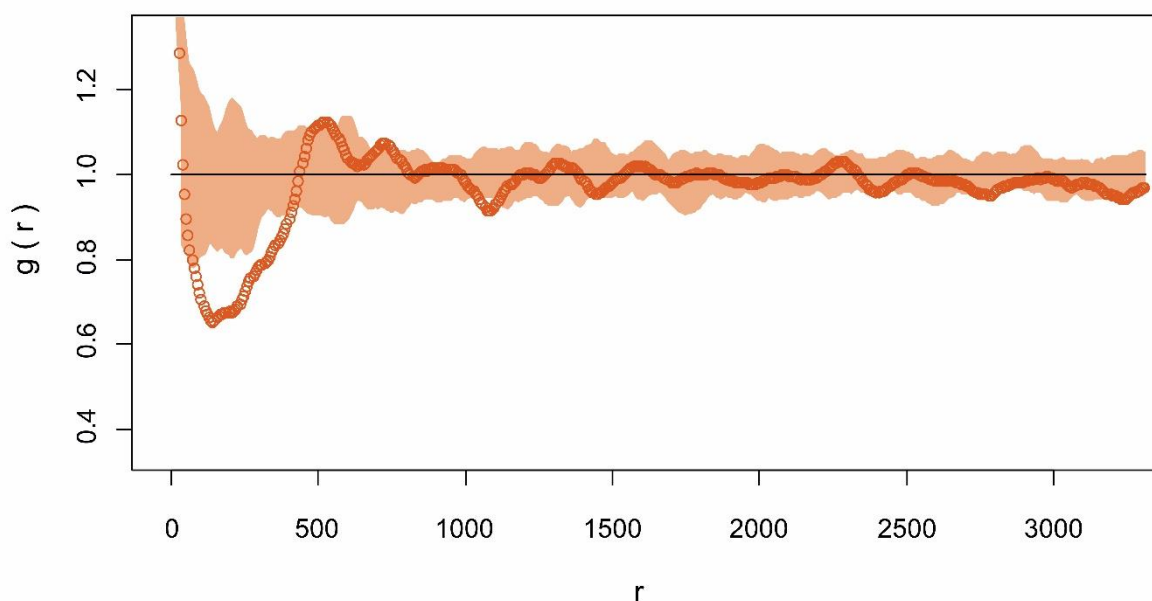
Figure 54 – *Pair correlation function for the tomography slice. The function is represented by the small circles. The straight line at g(r)=1 corresponds to total spatial randomness and the filled area is defined by the uncertainty envelopes. These correspond to 39 simulations of completely spatial randomness, representing, therefore, confidence intervals of 95%. X axis is the radius in µm and Y axis is the g(r) function.*

The tomography slice pair correlation function starts at infinity for r = 0 due to under-sampling of the small particles and continues with a rapid decrease in g(r) to a local minimum of g(r)=0.8 around r = 200 µm (Figure 54). The PCF then defines a relatively narrow peak of g(r)=1.12 at r = 500 µm and, in quick succession, a second one at 1.08 at r = 700 µm. The apparent hardcore ranges from 200 to 450 µm but due to the polydispersity of the particle sizes, the value does not represent a true hardcore. The peaks in the pair correlation function just barely exit the simulation envelopes so are judged only just statistically significant at α = 0.5. The subsequent undulations are not statistically significant because they lie inside the uncertainty envelopes.

4.2.4.3   Comparison of thin section & tomography slice

The comparison of the tomography slice and the thin section PCFs are shown in Figure 55. The peak in the tomography slice PCF is lower than the peak in the thin section but they both have a similar width. The peak in the tomography slice is shifted towards higher values of r. For r > 500 µm, the PCF of both samples tends towards 1 in a fluctuating tail. The pseudo hardcore value is smaller for the thin section which could indicate that the particles are smaller in the thin section.

The fluctuations in the thin section PCF lie outside the simulation envelopes representing confidence interval of 95% (blue area, Figure 55), meaning the fluctuations are statistically significant. The tail of the tomography slice PCF, however, stay within the simulation envelopes (orange area, Figure 55) for r > 900 µm. This means that the fluctuations are not statistically significant.
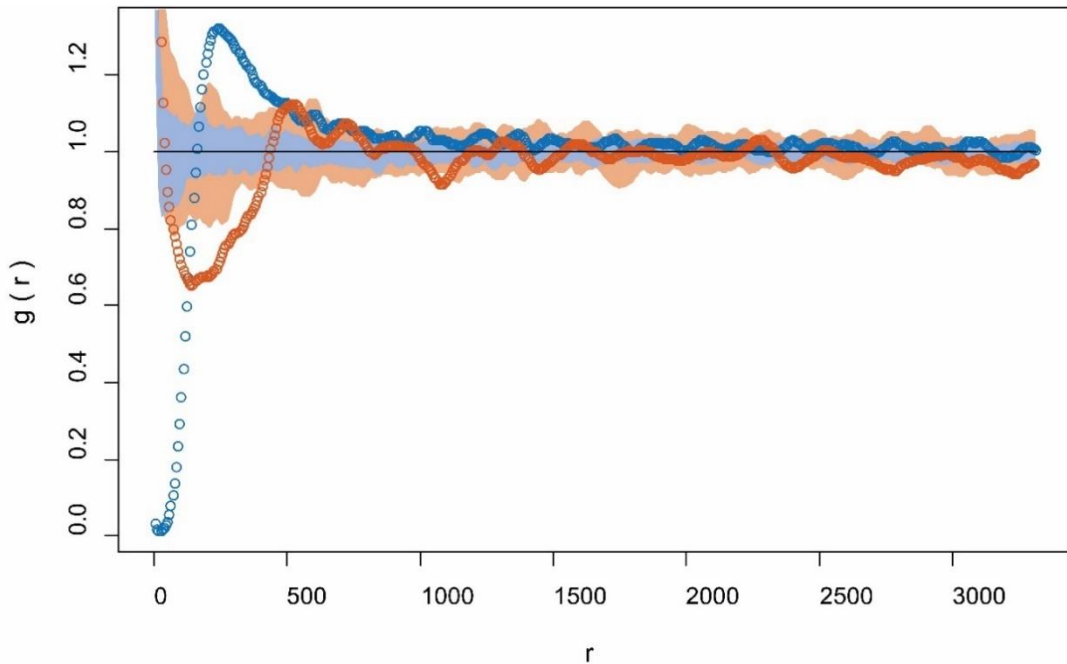
Figure 55 – Pair correlation function for the thin section data (blue), tomography slice (orange) and their corresponding simulation envelopes. The black line represents total spatial randomness g(r)=1, above that line represents a clustering of crystals in the sample and below that line represents ordering in the sample.

4.2.5   Summary of 2D data comparison

The difference in the mean, median and mode values for the equivalent diameter and area is significantly different and the difference of 24% in the total particle area is non-trivial. The correlation for barycentre location between the two data sets is good but only partial due to the missing particles in the tomography slice. The small to medium particles in the thin section are either missing in the tomography slice or erroneously integrated into larger particles. The mush architecture is similar for both thin section and tomography slice.

4.3 Comparison of 2D data sets: Sieved thin section and tomography slice

The missing particles in the tomography slice and the difference in total area between the tomography and the thin section data observed in the comparison above imply that the 3D tomography data or its treatment during segmentation and separation does not include the smaller grains. The comparison above is, therefore, an assessment of how well the tomography slice represents the thin section but does not test how well the tomography slice and thin section represent the same grains.

To address the issue of the missing particles and difference in total area in the tomography slice, the thin section data was sieved. Spatial and area data exist for all particles in both datasets and the thin section data can be sieved to select only the particles which have good spatial and area registration, i.e. the particles present in both datasets. The sieving keeps only the particles in the thin section that have an overlap area equal or greater than 1 pixel^2, 5 pixels^2, 10 pixels^2 and 125 pixels^2 when the particles of the tomography slice are physically put on top of the particles in the thin section. The sieving process enables us to keep *only* the particles that are in both data sets but also deletes any particles smaller than the area overlap criteria.

4.3.1 Bulk statistics

The particle number in the sieved thin section drops to 1719 for sieving with an overlap of 1 pixel, to 1627 for a 5-pixel overlap, to 1565 for a 10-pixel overlap and to 800 particles for an overlap of 125 pixels. The sieved thin section with a 125-pixel overlap has a number of particles closest to the tomography slice, which has 735 particles (Table 5). The mean particle area for the 1-pixel overlap thin section is 8.8 10^4 μm^2 which is 45% smaller than the tomography slice mean particle area. The mean value for the 5-pixel overlap thin section is 9.2 10^4 μm^2, 42.5% smaller than the tomography slice mean value. The 10-pixel overlap thin section has a mean particle area of 9.4 10^4 μm^2 and is 41% smaller than the tomography slice mean area. The closest mean particle area value to the tomography data is the 125-pixel overlap thin section with a mean area value of 1.5 10^4 μm^2, only 6.25% difference (Table 5).

Table 5: Quantitative evaluation of particle area in both the sieved thin section data sets. Values are shown in μm². The difference column indicates the difference in total area with respect to the tomography slice

Area [μm²]	# Grains	Mean	Median	Mode	Total area	Difference
TS 1 overlap	1719	$8.8 \cdot 10^4$	$4.6 \cdot 10^4$	$1.9 \cdot 10^4$	$1.52 \cdot 10^8$	25.6 %
TS 5 overlap	1627	$9.2 \cdot 10^4$	$4.9 \cdot 10^4$	$1.9 \cdot 10^4$	$1.49 \cdot 10^8$	23.8 %
TS 10 overlap	1565	$9.4 \cdot 10^4$	$5.1 \cdot 10^4$	$1.9 \cdot 10^4$	$1.48 \cdot 10^8$	22.4 %
TS 125 overlap	800	$1.5 \cdot 10^5$	$9.6 \cdot 10^4$	$4.4 \cdot 10^4$	$1.23 \cdot 10^8$	1.8 %
Tomography slice	735	$1.6 \cdot 10^5$	$7.6 \cdot 10^4$	197	$1.20 \cdot 10^8$	x

The median particle area for the 1-pixel, 5-pixel and 10-pixel overlap thin section data sets are lower than in the tomography slice and are respectively 39%, 36% and 33% smaller. The median particle area for 125-pixel overlap thin section is the closest to the tomography slice median value and is 26% higher (Table 5). The modal particle area for all sieved thin section data sets is at least two orders of magnitude higher than the mode for the tomography slice which is very low (197 μm²).

For smaller overlap areas, the total particle area is higher. Compared to the total particle area of the tomography slice (1.28 10⁸ μm²), the closest is the 125-pixel overlap thin section with only 1.8% difference.
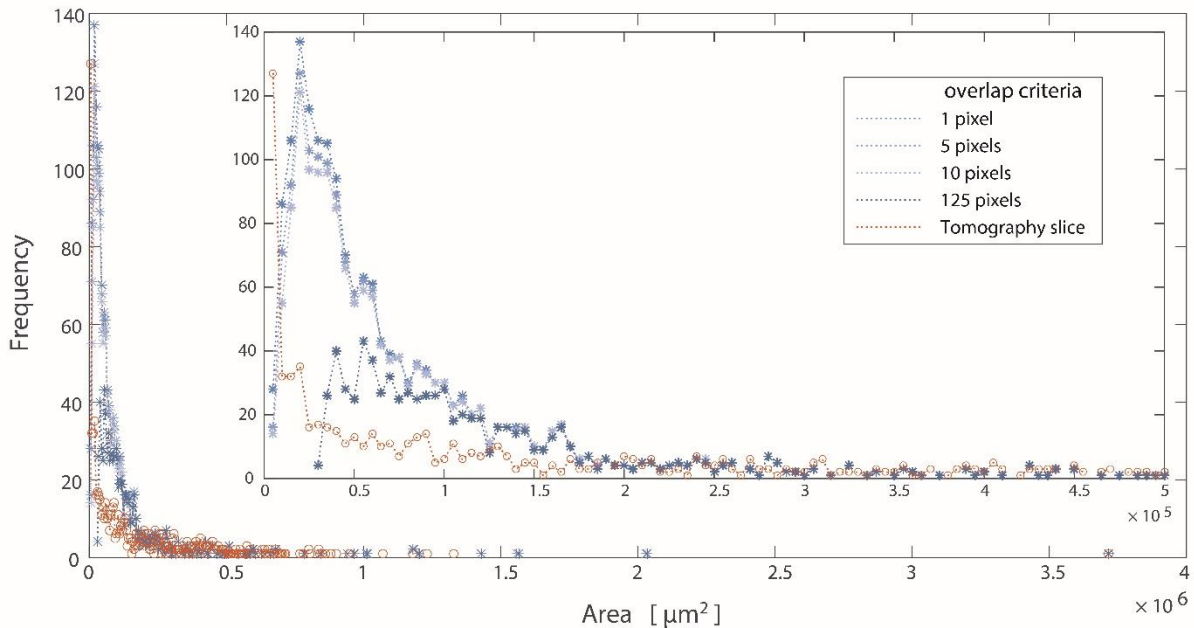
Figure 56 – Particle area histogram of sieved thin section data sets and tomography slice. X axis is area in μm² and Y axis is particle frequency. The histogram was constructed using size bins of 5000 μm².

The histogram of particle area (Figure 56) illustrates the numbers of Table 5. For particles $< 1.8 \cdot 10^5$ μm^2, the 1-pixel, 5-pixel and 10-pixel overlap thin section data all have a peak in the histogram for an area of $2 \cdot 10^4$ μm^2. This is close to the mode of the particle area ($1.9 \cdot 10^4$ μm^2 cf. Table 5). The histogram for 125-pixel has a lower amplitude peak over a range of areas of $4.5 \cdot 10^4$ μm^2 to $5.5 \cdot 10^4$ μm^2. This is close to the mode in Table 5 and the difference is explained by the size of the bins. The sieve thin section data sets all have a peak that is not present in the tomography slice. The peak of that histogram is for areas < 5000 μm^2, corresponding to the calculated mode (197 μm^2 cf. Table 5) within the range of the size bins (5000 μm^2). The 125-pixel overlap thin section has the lowest amplitude peak and is the closest to the tomography slice data. For particle areas $> 1.8 \cdot 10^5$ μm^2, the trends of the sieved thin section data sets, as well as the tomography slice, are similar. The trends become discrete points for areas larger than $7 \cdot 10^5$ μm^2.

The equivalent diameter histogram (Figure 57) has the same pattern as the particle area histogram (Figure 56). The sieved thin section data sets are distinguished from the tomography slice by a peak at 200 μm for 1 to 10-pixel overlap and at 300 μm for the 125-pixel overlap thin section, corresponding to the mode. The tomography slice does not have a peak but a maximum for particles smaller than 50 μm. For equivalent diameters > 550 μm, the trends become similar for all sieved thin section data sets and the tomography slice. The closest trend to the tomography slice is the 125-pixel overlap thin section.

Figure 57 – Equivalent diameter histogram of particles in the sieved thin section data sets and the tomography slice. X axis is equivalent diameter in μm and Y axis is frequency. The histograms were constructed using size bins of 50 μm.

Comparing the sieved thin section data sets to the tomography slice shows that the sieving brings the thin section data closer to the tomography slice, especially the 125-pixel overlap thin section. It represents best the particles that are in both the thin section and tomography slice. The particle numbers are close (800 for the 125-pixel overlap thin section compared to 735 particles in the tomography slice). The 125-pixel thin section has the closest total area (< 2% difference) and mean, median and mode areas (Table 5). Using the 125-pixel overlap thin section that represents best the particles in the tomography slice will enable us to interpret the comparison without having to account for the uncertainty of the missing particles in the tomography slice. From here on, the 125-pixel overlap thin section will be referred to as the *sieved thin section* and its dimensional metrology will be compared to that of tomography data to evaluate the accuracy of the shape and dimensions of the particles.

Figure 58 – Equivalent diameter histogram of particles in the sieved thin section and the tomography slice. X axis is equivalent diameter in µm and Y axis is frequency. The histograms were constructed using size bins of 50 µm.

The sieved thin section equivalent diameter histogram has a frequency peak of 145 at 300 µm. The tomography slice histogram does not show a peak but a negative trend with a maximum at < 50 µm (Figure 58). From equivalent diameters of 550 µm to higher values, the two histograms are similar although the tomography slice histogram is higher than the sieved thin section histogram. The differences in the histograms mean that there are more particles with equivalent diameters of 200 to 550 µm in the sieved thin section than the tomography slice but more medium to large particles (600-

97

1100 μm) in the tomography slice. These differences can be explained by under-separation of the tomography slice.

The particle area histograms for both data sets show trends similar to the equivalent diameter histograms. The sieved thin section has a peak around areas of 4.5 to $5.5 \cdot 10^4$ μm^2 that is not present in the tomography slice (Figure 59). For particle areas $> 2.5 \cdot 10^5$ μm^2, the histograms have similar trends tending to a frequency of 1. The differences in the particle area histograms can be explained by the under-separation of the particles in the tomography slice.
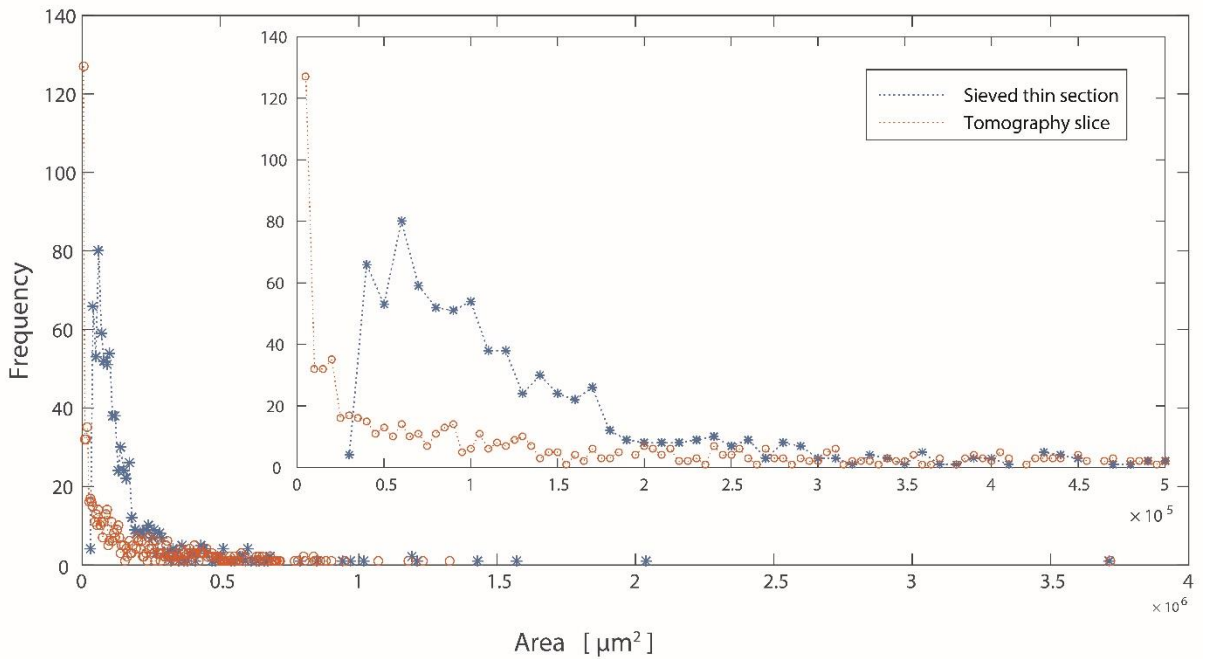
Figure 59 – Particle area histogram of the sieved thin section and tomography slice. X axis is area in μm² and Y axis is particle frequency. The histogram was constructed using size bins of 5000 μm².

4.3.2 Crystal size distribution

The sieved thin section CSD is humped with a maximum frequency around an equivalent diameter of 300 μm. The population density then decreases for increasing particle size, until 1000 μm when the signal becomes noisy and flattens out (Figure 60). Confidence intervals at 95%, illustrated by the error bars are smaller for higher frequencies and become large for low frequencies.
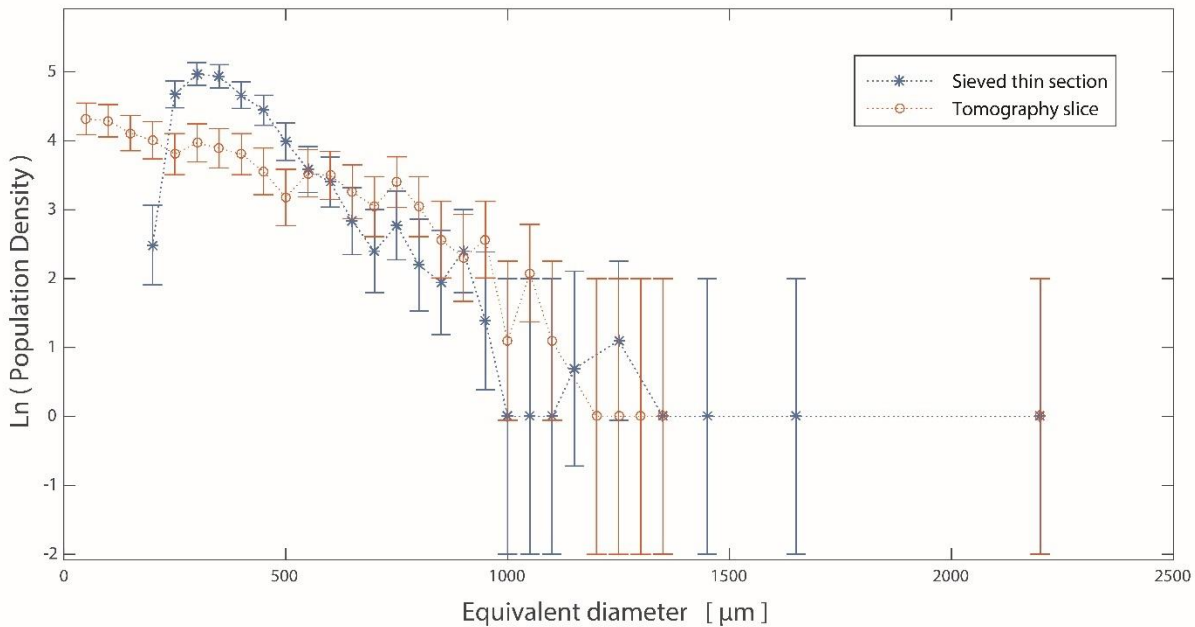
Figure 60 – Crystal size distribution of particles in the sieved thin section and the tomography slice. The size of the particles was evaluated using equivalent diameter. X axis is equivalent diameter in μm and Y is the logarithm of the frequency. The error bars correspond to confidence intervals of 95%.

The sieved thin section CSD is closer to the tomography slice CSD than the original thin section, with a lower amplitude peak in the sieved thin section data. The peak in frequency at 300 μm in the sieved thin section is absent in the tomography slice CDS. The sieved thin section has a higher frequency of particle sizes ranging 250 μm to 500 μm (Figure 60). For particles > 550 μm, both have similar slopes and become noisy around 900 μm due to low frequencies.

4.3.3 Spatial distribution

Comparing the barycentre locations of the sieved thin section and the tomography slice (Figure 61), the correlation is similar to the comparison between the thin section and the tomography slice (cf. Figure 44), where there is a good correlation for medium to large crystals (cf. Figure 45). The sieving of the thin section data affects the small particles as any particles under 125 μm² in area are not retained during the sieving process. The difference is shown in Figure 62: the agglomeration of small particles in the thin section (top of Figure 62, 1C) that are represented by fewer particles in the tomography (top of Figure 62, 1B) are now almost all gone (top of Figure 62, 2A, 2B and 2C). This confirms that there is less ambiguity in detecting over- and under-separation in the tomography slice.
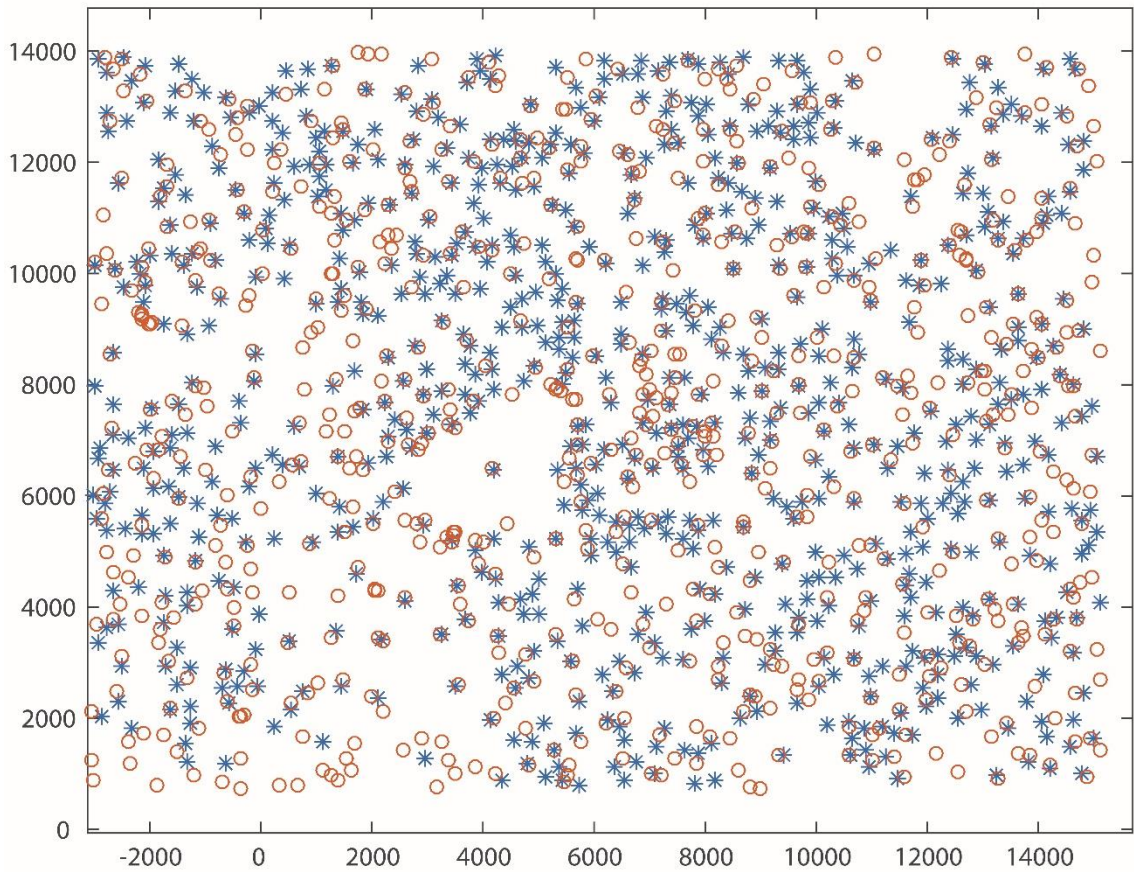
Figure 61 – Comparison of barycentre location for the sieved thin section data set and the tomography 2D data. The blue stars are the sieved thin section data; the orange circles the tomography data. X and Y axes are positions in μm.
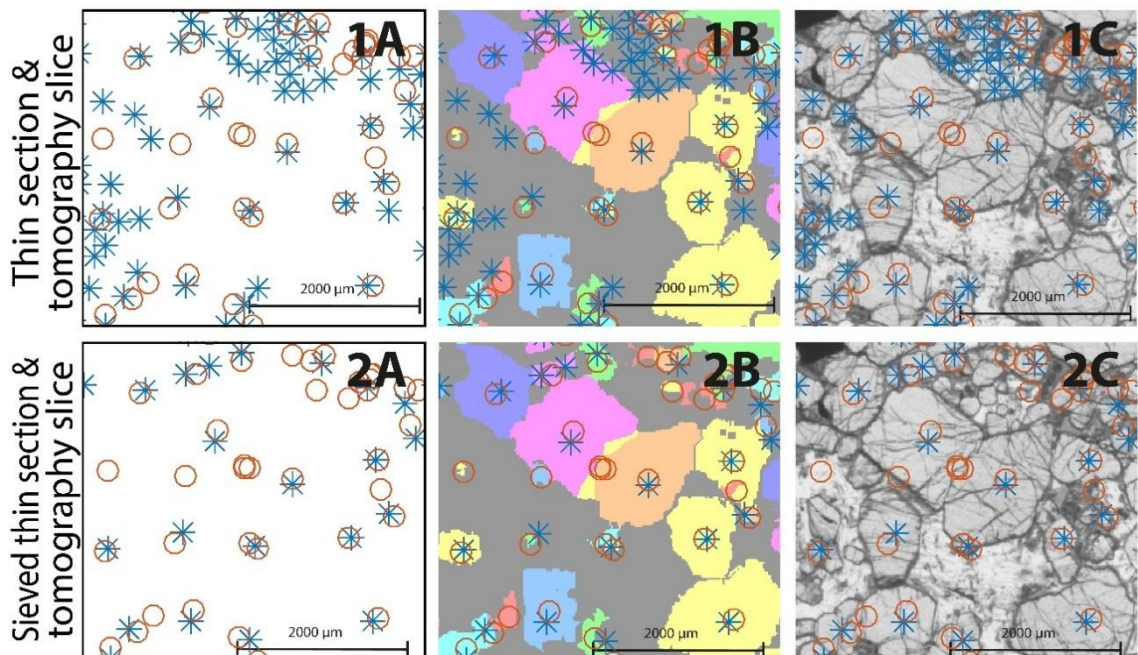
Figure 62 – Detail of barycentre location in the sieved thin section and the tomography slice looking at small particles. Row 1 depicts the thin section compared to the tomography slice and row 2, the comparison of the sieved thin section and the tomography slice.
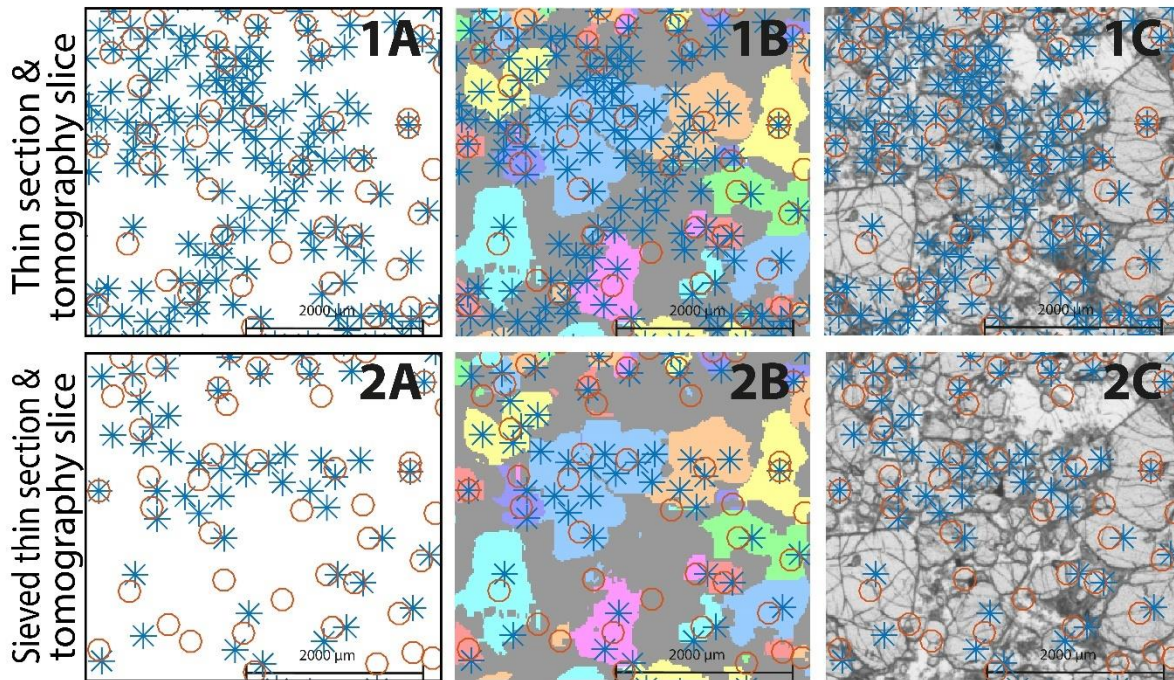
Figure 63 – Detail of barycentre location in the sieved thin section and the tomography slice.
Row 1 depicts the thin section compared to the tomography slice and row 2, the comparison
of the sieved thin section and the tomography slice.

The correlation in barycentre location in the sieved thin section and the tomography slice is qualitatively better than that of the original thin section and the tomography slice. There are still instances of under-separation of the tomography slice, where several particles in the sieved thin section correspond to one particle in the tomography slice (Figure 63). Where many particles from the thin section are represented by few in the tomography slice (blue and orange particles in centre, Figure 63, 1A, 1B and 1C), the sieving has reduced the number of particles in the thin section (blue and orange particles in centre, Figure 63, 2A, 2B and 2C). The same instances of over-separation observed in the original thin section are still visible in the sieved thin section (cf. Figure 46, 1a and 1b).

Qualitatively, the sieved thin section and the tomography slice correlate well, as illustrated by the *nncross* nearest neighbour graph (Figure 64). Generally, the arrows are very short, except for cases of over-separation, where one particle in the sieved thin section is represented by several in the tomography slice, for example, the bottom western corner (cf. Figure 46, 1a and 1b). This is largely due to the closer number of particles. The sieved thin section has 800 particles for 734 in the tomography slice. Quantitatively, however, the distance between the *nncross* nearest neighbours in the sieved thin section is close to the *nncross* distance in the original thin section data (mode: 100 µm, min-max: 0.7-

843 µm). The modal distance between the *nncross* nearest neighbours in the sieved thin section is 100

µm with a minimum at 9 µm and a maximum at 1163 µm (Figure 65).
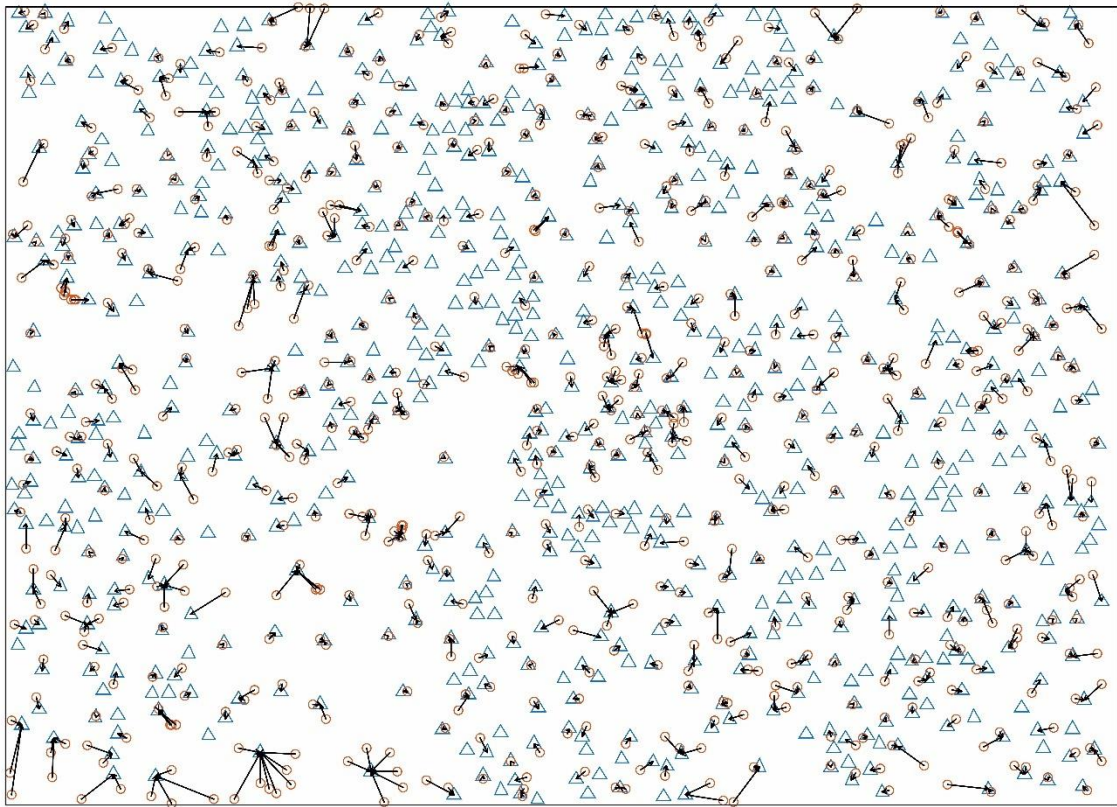
○ M2D_baryPPP   △ TSFilt_baryPPP

Figure 64 – The nncross nearest neighbour location and distance for one data set to the other. For each particle of the tomography slice (orange circles), the nearest neighbour is found in the sieved thin section data (blue triangles) and indicated by an arrow. The distance for each match is computed and is represented by the length of the arrow.
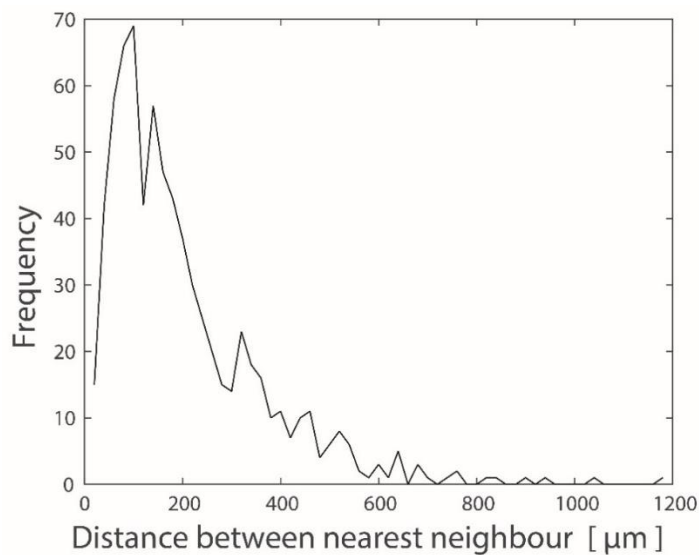
Figure 65 – Frequency histogram of the distance separating the nncross nearest neighbour particles in the thin section and tomography slice.

The barycentre location maps provide information about how close the particles are to each other but

do not include the area of the particles. For this purpose, area maps created by drawing circles of radius

proportional to the area centred in the barycentre are used (see section 3.4.2.3). The sieved thin section

particle areas are compared to the tomography slice particle areas in Figure 67.
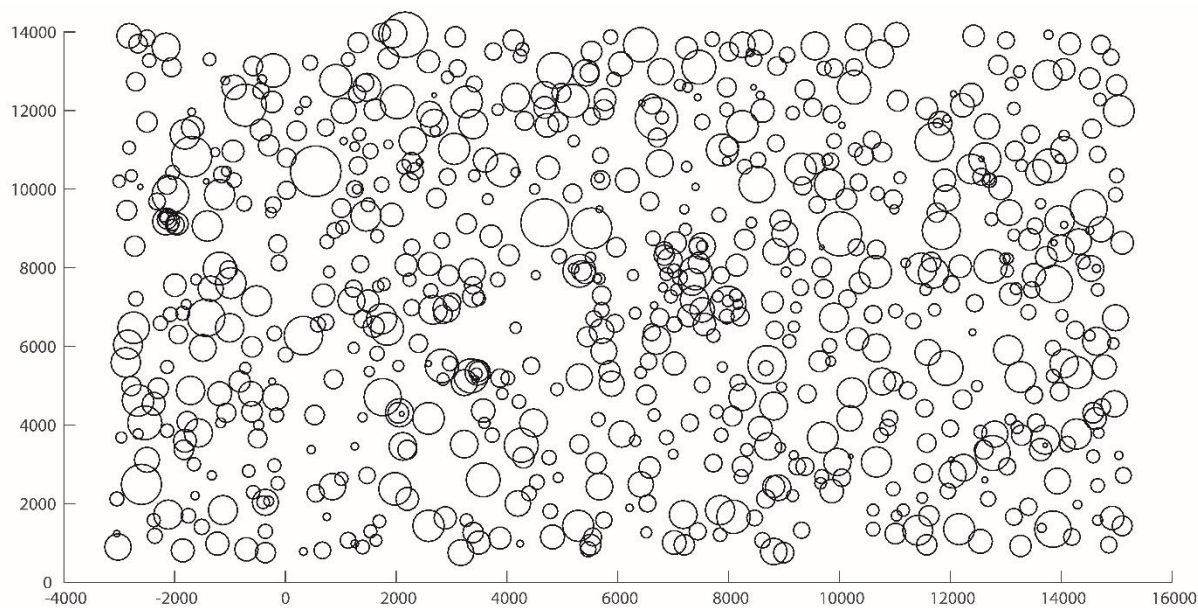
Figure 66 – Map of the distance between the nncross nearest neighbour pairs associated with the tomography data.
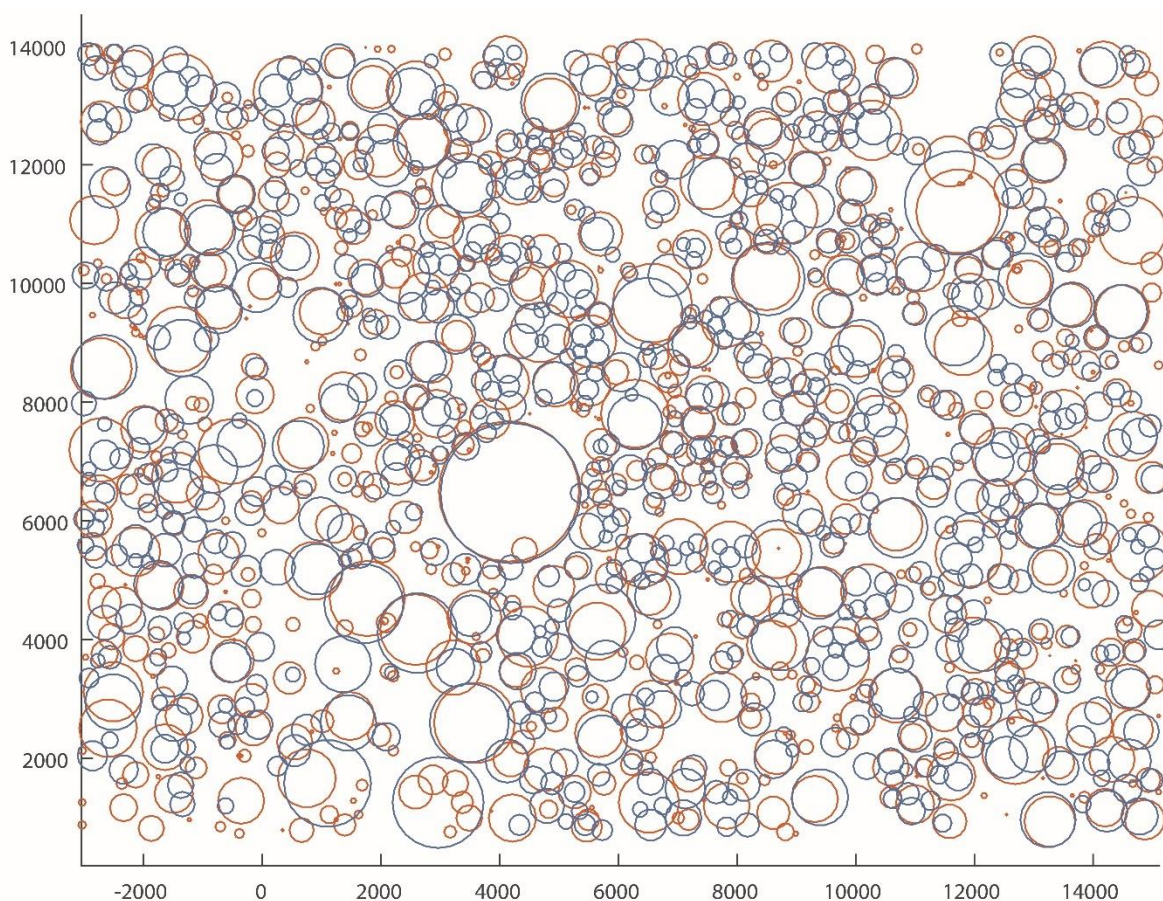
Figure 67 – Area map of the particles in both sieved thin section (blue) and tomography slice (orange). The circles are centred on the barycentre of each particle and have a radius of the area. X and Y axes are position in space and are in μm.

The overlain particle area maps show a good correlation in area for medium to large particles (Figure 67). The numerous small particles agglomerated around larger ones in the original thin section are now not observable anymore in the sieved thin section. Their absence yields a better correlation for particle area between the sieved thin section and the tomography slice. The textures of under- and over-separation are clear. Figure 68 shows at least 5 occurrences of under-separation where a collection of particles in the sieved thin section (dark blue circles) correspond to a single particle in the tomography slice (orange circles). Over-separation is less frequent; as detailed above (Figure 46, A1).
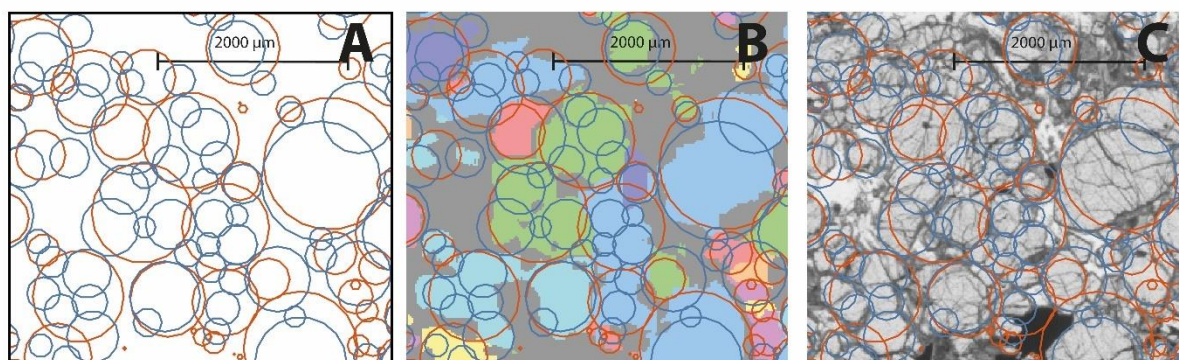
Figure 68 – Detail of particle area in the sieved thin section and the tomography slice looking at under-separation in the tomography data. A: comparison of particle area between the sieved thin section and the tomography slice; B: particle area and the tomography slice; C: particle area and the thin section scan.

4.3.4 Packing and mush structure

The pair correlation function for the sieved thin section is equal to 0 for r ≤ 100 μm. g(r) then increases rapidly to a peak of 1.3 around r = 300 μm. The undulating tail loosely tends towards 1 but remains above g(r)=1 (Figure 69). The tomography slice PCF shows an inverse trend for small particle sizes with a rapid decrease in g(r) to a local minimum of g(r)=0.8 around r = 200 μm followed by a peak of g(r)=1.12 at r = 500 μm. The peak in the tomography slice PFC is lower than the peak in the sieved thin section and is wider. The peak in the tomography slice PCF is shifted towards higher values of r. For r > 500 μm, g(r) for both samples tends towards 1 in a fluctuating tail.

The
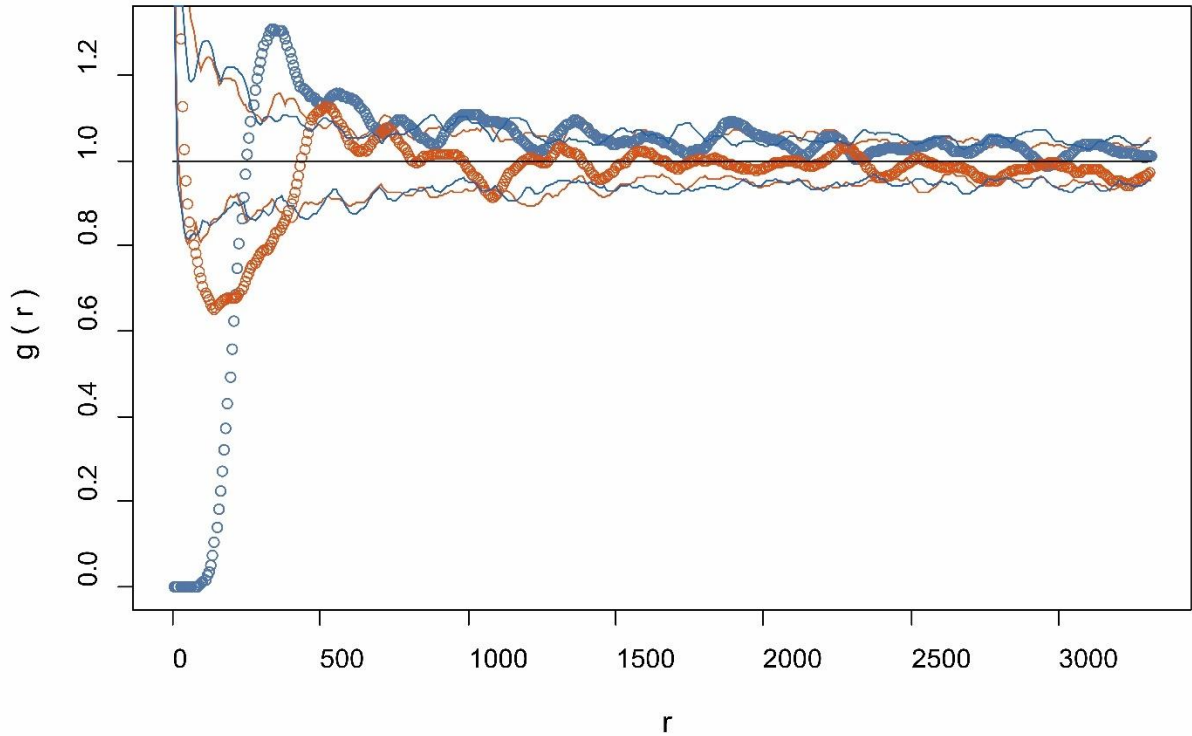
Figure 69 – Pair correlation function for the sieved thin section data (dark blue), tomography slice (orange) and their corresponding simulation envelopes. The black line represents total spatial randomness g(r)=1, above that line represents a clustering of crystals in the sample and below that line represents ordering in the sample.

fluctuations in the sieved thin section PCF, as well as the tomography slice PCF, stay within the simulation envelopes (blue and orange lines, Figure 69) for r > 1000 μm. This means that the fluctuations are not statistically significant from then on.

4.3.5 Shape

The roundness of the particles is evaluated using the shape factor, a dimensionless number function of perimeter and area. The shape factor is 1 for a perfect circle. For increasing shape factor values, the less round the particles are. Length and width are also used to describe the shape of the particles (Figure 70).

The particles in the sieved thin section are rounded to sub-rounded with shape factors of 1 to 2 with outliers at 2.5 (Figure 70, left). Most of the particles have a shape factor between 1 and 2, independent of size. The particles with shape S > 2 correspond to small particles of $7 \cdot 10^4$ μm^2 (Figure 70, left). The particles in the tomography slice have larger shape factors from 1 to 7.5 with outliers at 10 and 15. In both data sets, the larger particles are rounded. Shape factors S > 10 correspond to either elongated particles or particles affected by the cropping of the sample, giving them an elongate shape.

There is a marked correlation between length and width in the sieved thin section (Figure 70, right). The slope ranges from 0.90 to 0.55. The positive correlation means that the longer the particle the wider it is and suggests that most of the particles are similar in shape. There are few particles outside the general trend, and these can be linked to the particles with high shape factors.
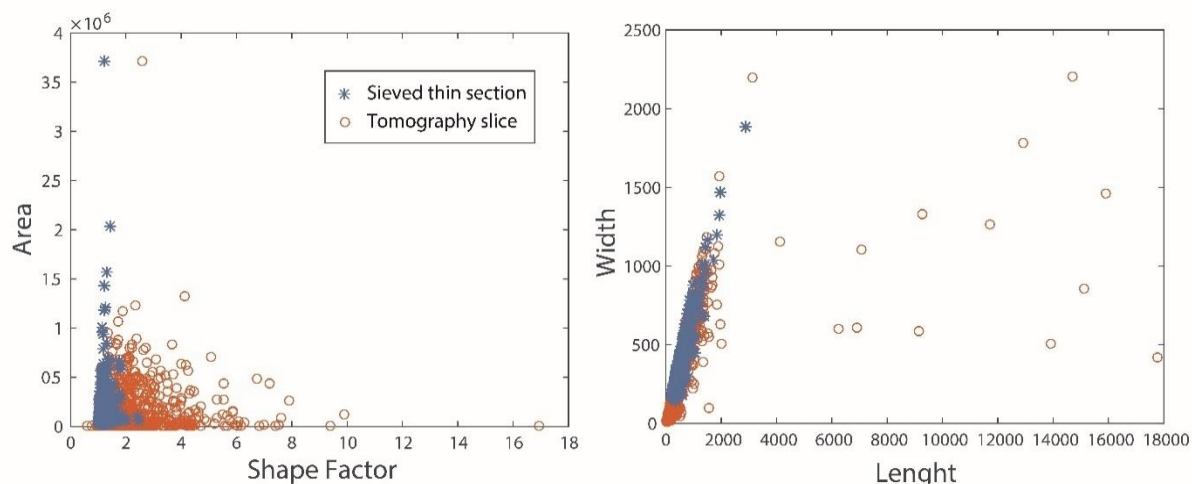
Figure 70 – Left: Shape factor for each particle plotted against area. X axis is shape factor, a dimensionless number and Y axis is area in μm². Right: Length and width of particles plotted against each other. X and Y axis are in μm.

4.3.6 Summary of comparison: sieved thin section and tomography slice

The tomography slice is closer to the sieved thin section data than the original thin section data. The sieved thin section is the closest we can come to the representing the particles in the tomography slice. The difference in total area is reduced to only 2%. The spatial distribution of the particles is similar in both data sets and the particles have similar shapes.

4.4 Comparison of 2D to 3D: tomography slice and tomography stack

The tomography slice is compared to the 3D render of the particles in the slice (tomography stack). Comparing these objects provides a true evaluation of how representative a 2D view of a 3D object is. This is a simplified system where the same object is observed in different dimensions (2D and 3D). This comparison test how different the attributes of the particles are in 2D, using the 3D as a reference.

4.4.1 Bulk statistics

The basic statistics for particle size are performed on the equivalent diameter as opposed to area as an area in 2D has no comparison in 3D. The equivalent diameter definition does not vary when adding a dimension.

The mean equivalent diameter of particles in the tomography slice is 27 % smaller than the mean equivalent diameter of particles in the stack (Table 6). The median value for the slice is also smaller (25%) than the median equivalent diameter in the stack. The mode of the equivalent diameter is 40% smaller in the slice.

Table 6: Quantitative evaluation table of equivalent diameter statistics, comparing the tomography slice to the tomography stack.

Equivalent Diameter [μm]	Mean	Median	Mode
2D slice	362	311	16
3D stack	497	443	27

The equivalent diameter histograms show similar trends for the slice and the stack (Figure 71). The tomography stack histogram starts at a frequency of 90 for the small particles (> 50 μm) whereas the slice starts with a frequency of 75 for the same size: there are more smaller particles in the stack than in the slice. The histograms are noisy, especially the stack histogram which has higher amplitude fluctuations. Particles ranging 850 μm to 1200 μm are more abundant in the stack than in the slice. For large particles (> 1200 μm), there are as many particles in the stack as in the slice.

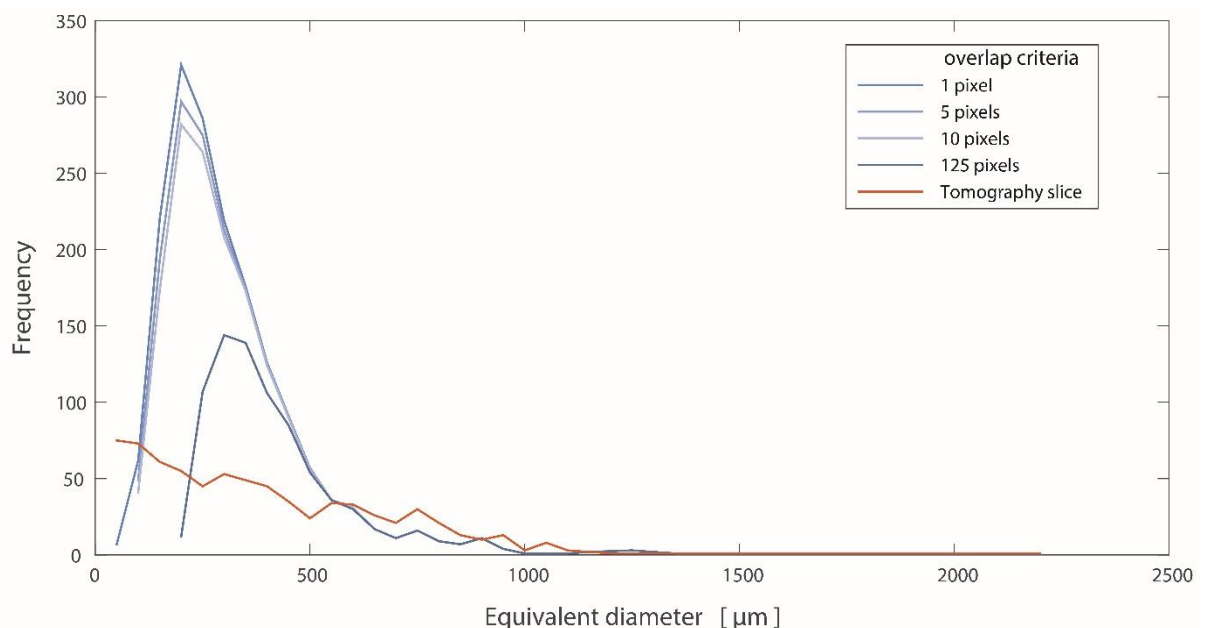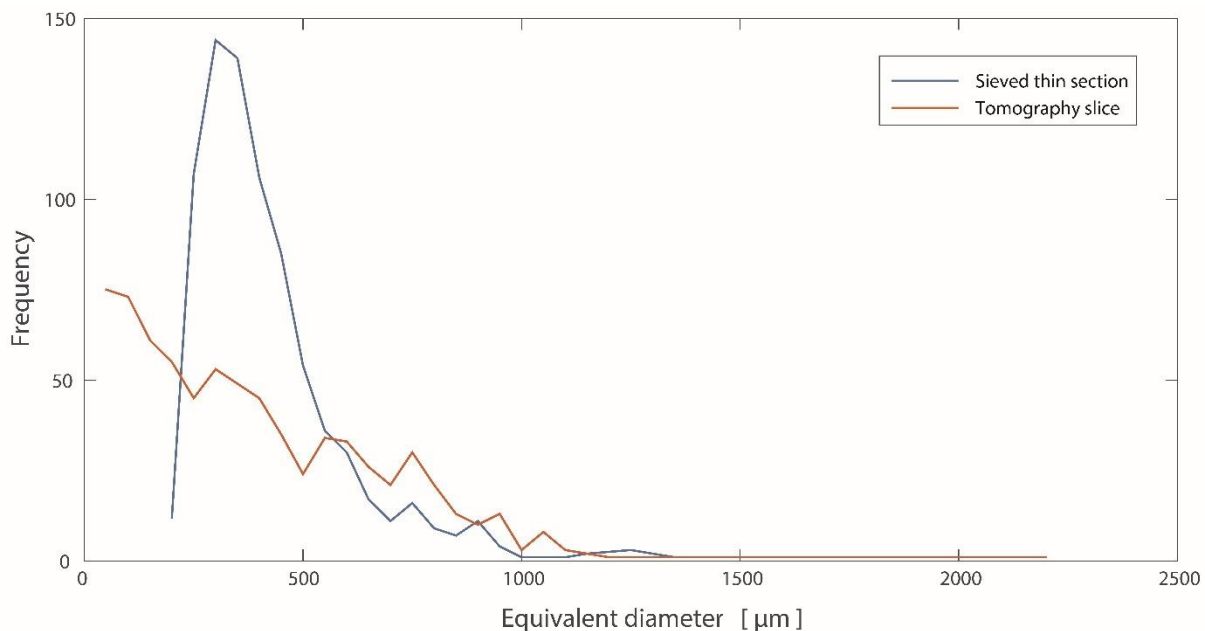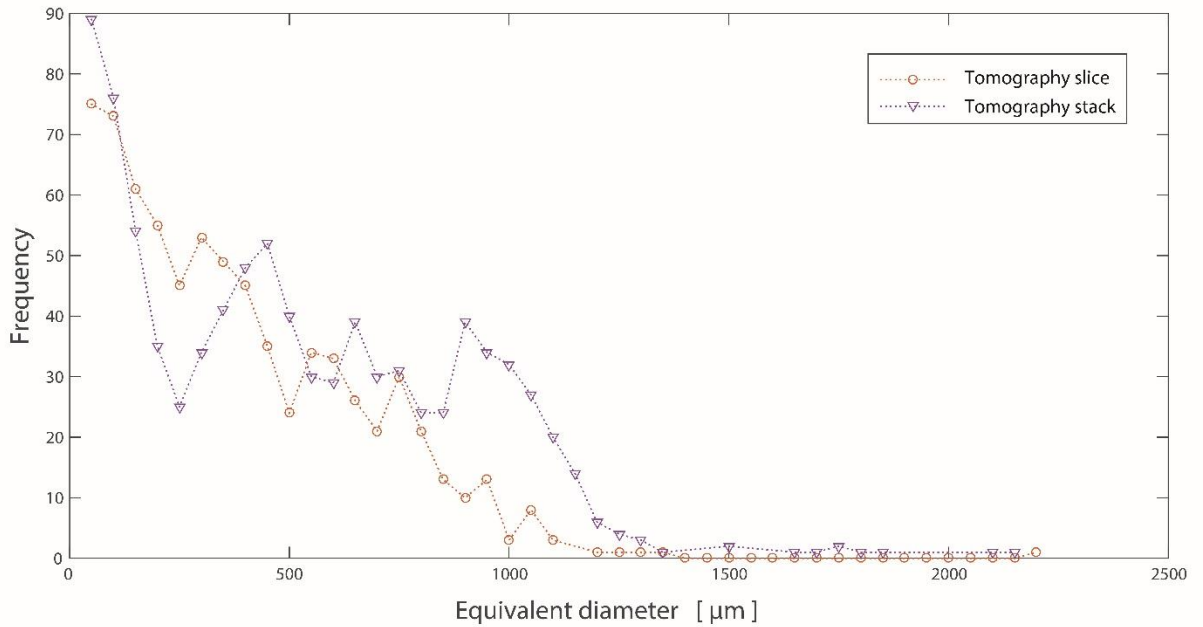*Figure 71 – Equivalent diameter histogram of particles in the tomography slice and the tomography stack. X axis is equivalent diameter in μm and Y axis is frequency. The histograms were constructed using size bins of 50 μm.*

4.4.2 Crystal size distribution

The slice and stack CSDs are globally similar, with the same kinks in the trends (Figure 72). For particles < 850 μm, the CSDs are overlapping, within error. The error bars illustrate confidence intervals of 95%. There are more particles ranging from 850 μm to 1400 μm in the stack than in the slice. The CSDs overlap again for particles larger than 1400 μm. The tomography slice does not have a continuous range of larger particles but stops at an equivalent diameter of 1400 μm with an outlier at 2200 μm. The stack has a more continuous spread of larger particles with an almost continuous distribution of sizes until 2150 μm. The 95% confidence intervals illustrated by the error bars are smaller for higher frequencies and become large for low frequencies.
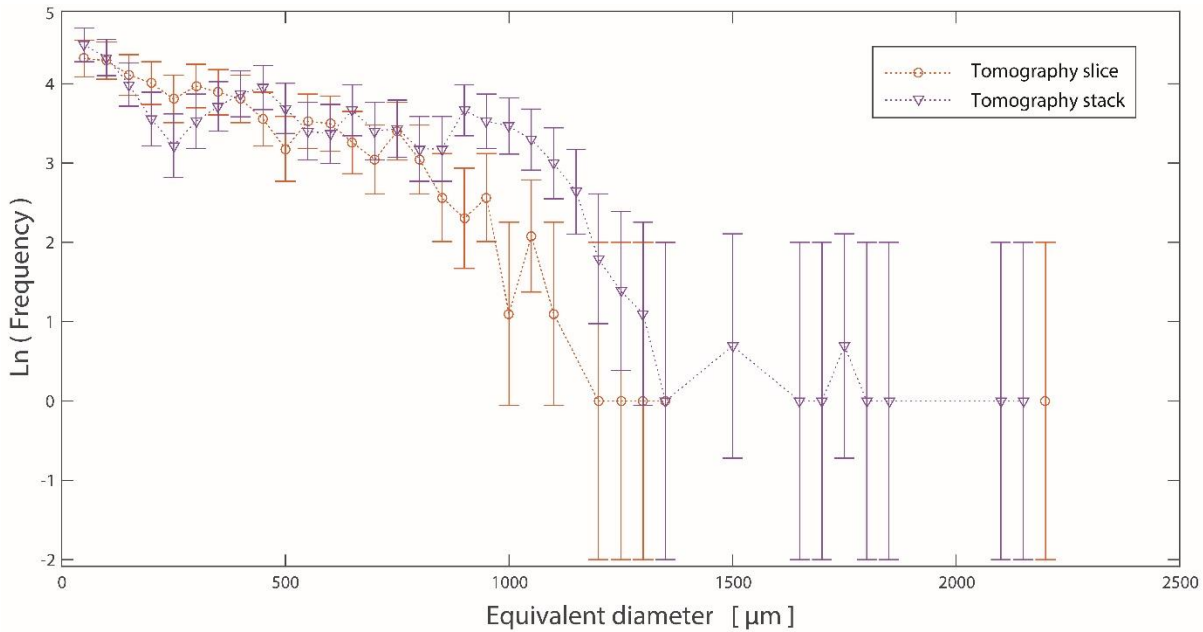
Figure 72 – Crystal size distribution of particles in the tomography slice and the tomography stack. The size of the particles was evaluated using equivalent diameter. X axis is equivalent diameter in µm and Y is the logarithm of the frequency. The error bars correspond to confidence intervals of 95%.

4.4.3   2D spatial distribution

For the tomography stack, the barycentre locations of each particle were projected on the slice to produce the barycentre map (Figure 73). There is a good correlation for the location of the barycentre of the particles. Most particles in the stack have an overlapping particle in the slice.

Quantitatively, the *nncross* nearest neighbour shows that the correlation between the stack barycentre locations and the barycentre locations in the slice is good (Figure 74), with a modal *nncross* distance of 20 µm, with a maximum of 482.4 µm and a minimum of 0 µm. In general, the barycentre locations of the particles in the stack are well represented in the slice, as the *nncross* distance is small.
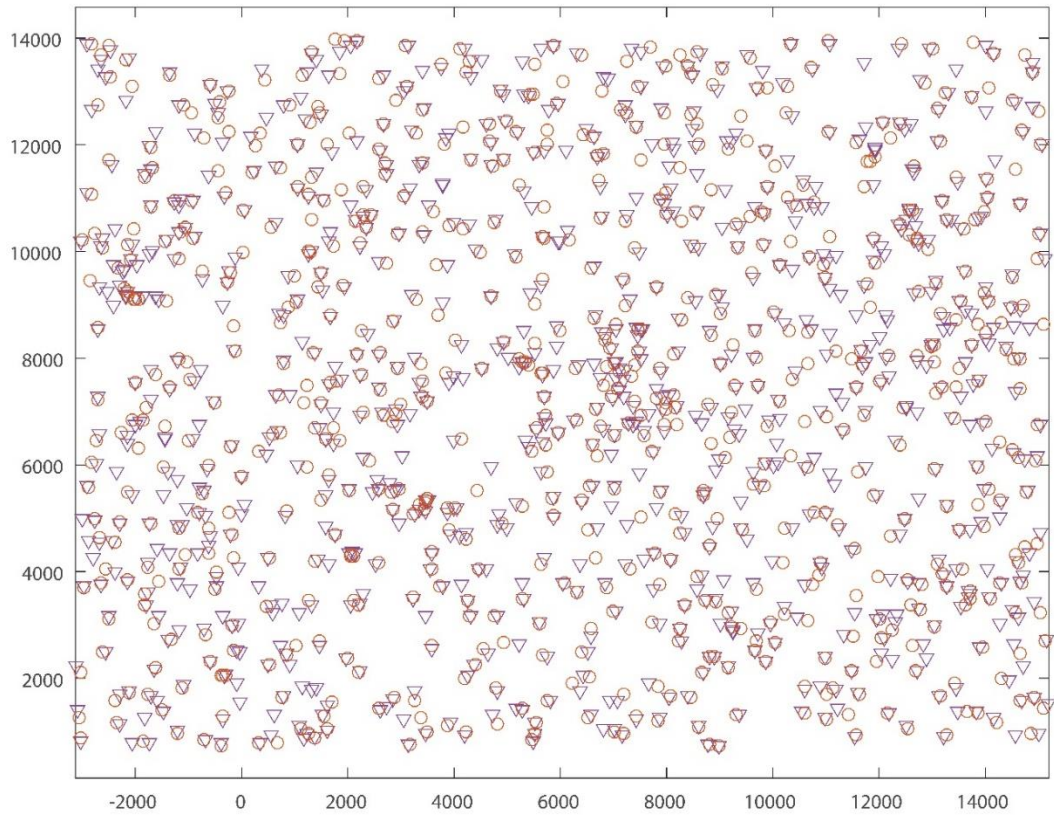
Figure 73 – Comparison of barycentre location for the tomography stack (purple triangles) and the tomography slice (orange circles). X and Y axes are positions in µm.
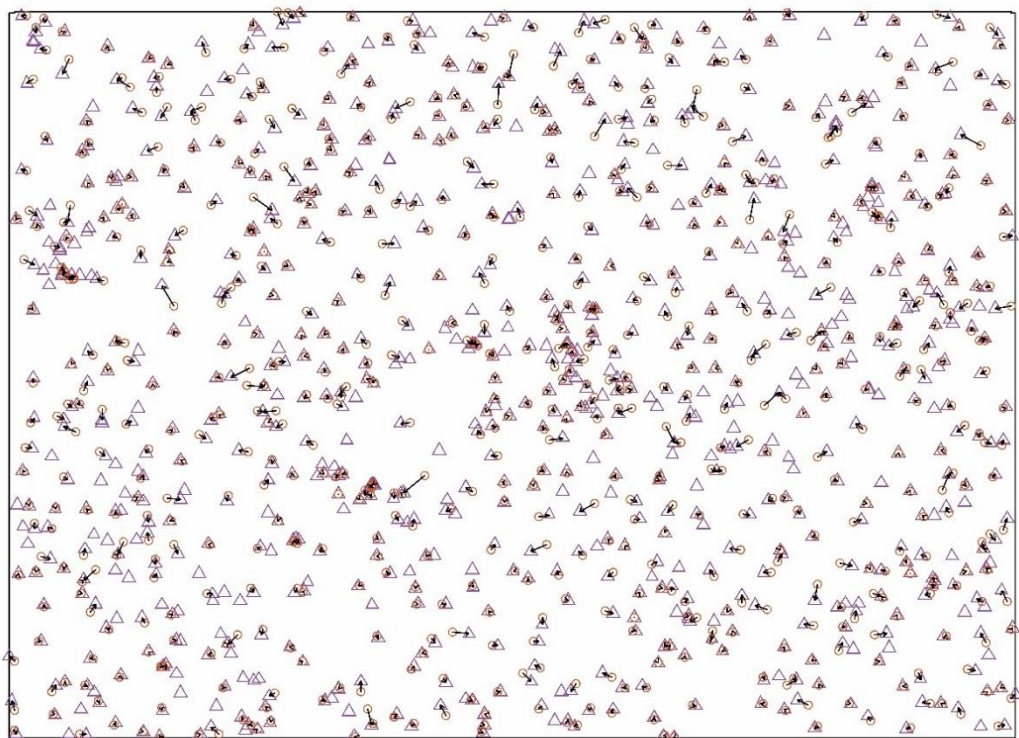
○ Tomography slice   △ 3D Tomography stack

Figure 74 – The nearest neighbour location and distance for one data set to the other. For each particle of the tomography slice (orange circles), the nearest neighbour is found in the 3D stack (purple triangles) and indicated by an arrow. The distance for each match is computed and is represented by the length of the arrow.

4.4.4　Packing and mush structure

The pair correlation function uses the position of barycentre to determine the packing structure of the mush and evaluates clustering and ordering of the particles.
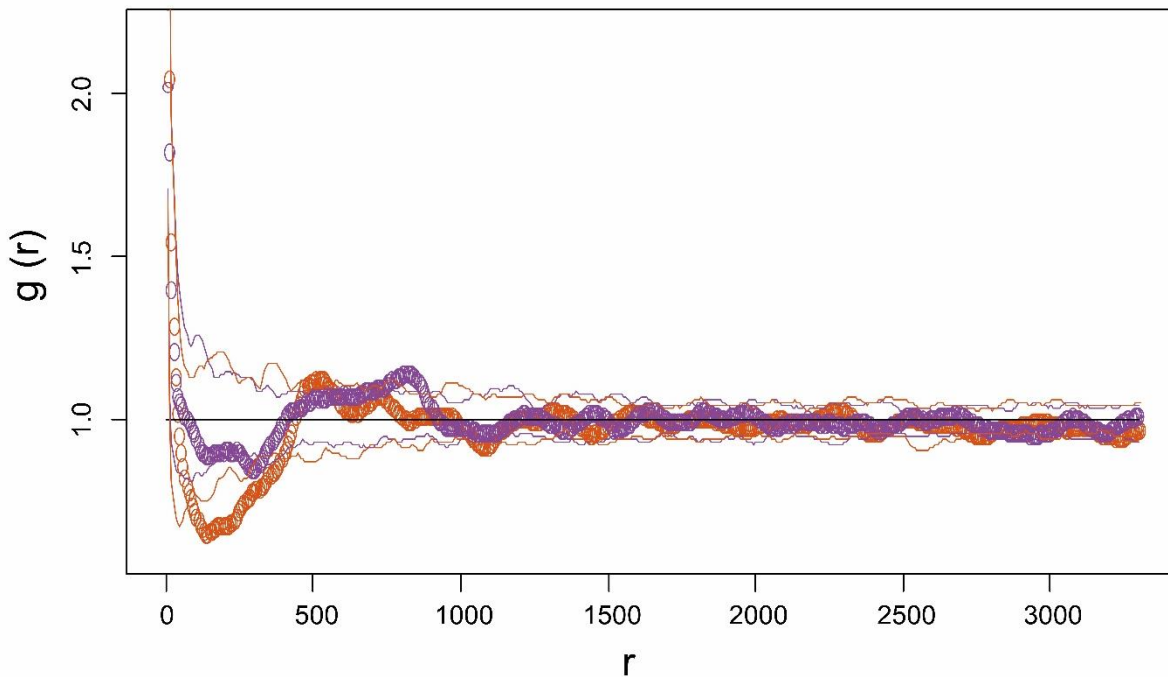
Figure 75 – Pair correlation function for the tomography stack (purple), tomography slice (orange) and their corresponding simulation envelopes. The black line represents total spatial randomness g(r)=1, above that line represents a clustering of crystals in the sample and below that line represents ordering in the sample.

The pair correlation function yields similar results for the tomography slice and 3D stack (Figure 75). Both functions tend to high g(r) for r=0, with a rapid decrease to reach a local minimum of g(r)=0.8 around r = 200 μm followed by a peak of g(r)=1.35 at r = 500 μm for the tomography slice. The 3D stack trend decreases rapidly to a minimum of g(r)=0.9 around r = 350 μm then increases to a local maximum of g(r)=1.2 at r = 800 μm. The apparent hardcore distance ranges from 200 to 400 μm for the tomography slice and from 350 to 470 μm for the stack. The PCFs then tend loosely to 1 with an undulating tail. Both pair correlation functions are outside the uncertainty envelopes, meaning that the trends observed are statistically significant; but for r > 900 μm, the trends are inside the envelopes and so are not statistically significant.

4.4.5　Shape

The shape of the particles is similar in both the tomography slice and stack (Figure 76, left). The particles are sub-rounded with shape factors ranging from 1 to 10. This is true for sizes ranging from 0 to 2200 μm for the slice as well as the stack. Both the tomography slice and stack show a spread of data towards

larger shape factor values. The anomalous shape factor values in the tomography stack range 10 t0 55, with outliers at 70, 80 and 110; the slice has a smaller spread of large shape factor values reaching 15 with outliers at 20. The large shape factor values belong to particles with an equivalent diameter smaller than 200 µm and are attributed to elongated particles. Particles on the side of the sample are cut when the data was cropped and are therefore artificially elongated.

There is a marked correlation between the length and width of the particles in the tomography slice and stack (Figure 76, right). The data is spread on a broad line with slope ranging 0.89 to 0.61. The positive correlation means that the longer the particle the wider it is as well. This is in accordance with the small shape factor values. There is a cloud of outliers that do not conform to the length-width trend in both 3D data sets. The outliers form a very broad trend with a flat slope and correspond to elongate particles (high length value and low width).

Figure 76 – Left: Shape factor for each particle plotted against area. X axis is shape factor, a dimensionless number and Y axis is area in µm². Right: Length and width of particles plotted against each other. X and Y axis are in µm.

4.4.6 Summary of slice to stack comparison

The tomography slice and stack data have similar particle size distributions. Bulk statistics yields a considerable under-estimation of particle size in the tomography slice. Particle barycentre locations in the tomography stack are close to those observed in the slice and their shapes are similar as well. Particle are round to sub-rounded in both data sets and have similar mush structures.

4.5   Comparison of 3D data sets: tomography stack and tomography volume

To evaluate how representative looking at a local volume out of a whole sample is, the 3D stack is compared to the 3D volume.

4.5.1   Bulk statistics

4.5.1.1   Tomography Volume

The mean, median and mode values for equivalent diameter and area of the particles in the tomography volume are shown in Table 7. The mean and the median of the equivalent diameter have a difference of 25%, which is explained by the influence of larger particles on the mean. The mode value is more than 90% smaller than the mean and the median. The most frequent particle size is very small.

Table 7: Quantitative evaluation of particle equivalent diameter and area in tomography data. Values are given in µm for equivalent diameter and in µm² for area

3D volume	Mean	Median	Mode
Equivalent diameter	358	266	23
Area	$1.17 \cdot 10^6$	$3.4 \cdot 10^5$	676

The equivalent diameter histogram (Figure 77) shows that the majority of the particles in the tomography data have an equivalent diameter smaller than 1200 µm. The maximum of the distribution is indicative of the mode value and corresponds to equivalent diameters of 50 µm or less. There are few particles larger than 1200 µm. There is a local maximum around 400 µm that breaks up the rapidly decreasing trend.
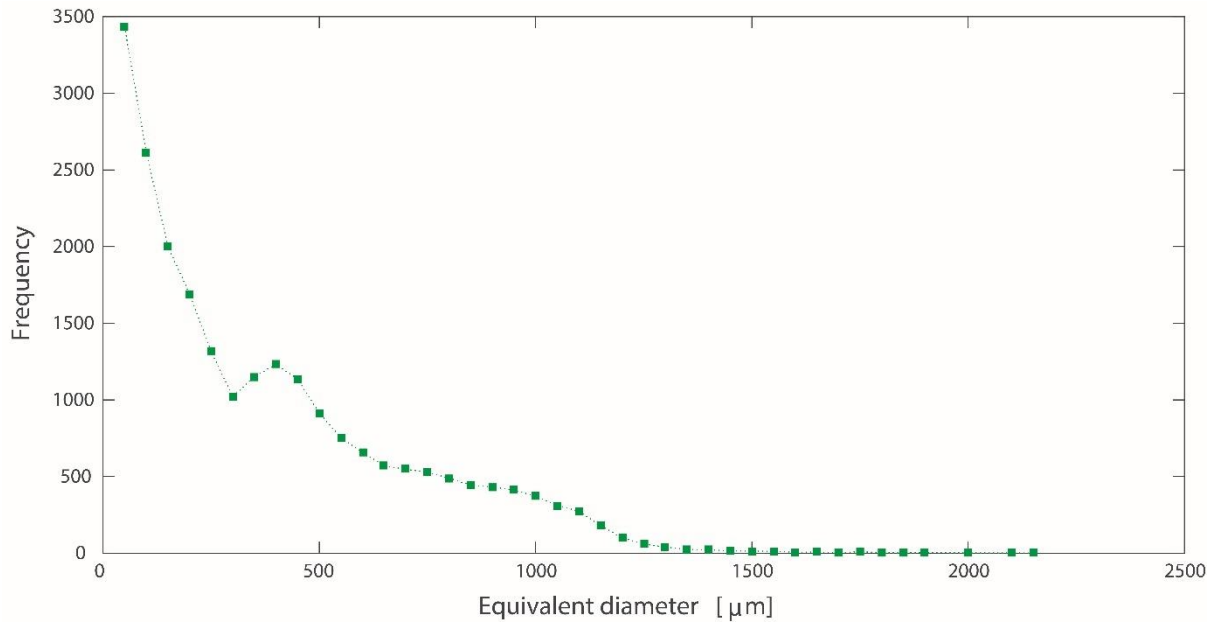
Figure 77 – Equivalent diameter histogram of particles in the tomography volume. X axis is equivalent diameter in µm and Y axis is frequency. The histogram was constructed using size bins of 50 µm.

The area histogram (Figure 78) shows a negative trend and that most of the particles have an area below 10^6 µm^2. There is a local maximum around $1.1 \cdot 10^6$ µm^2, which recalls the equivalent diameter histogram where the same feature is present. The maximum particle frequency corresponds to small areas of 5000 µm^2 or lower. This value should reflect the mode but due to the size of the bins (5000 µm^2), the values are very different. There are only few particles with an area above 10^6 µm^2.
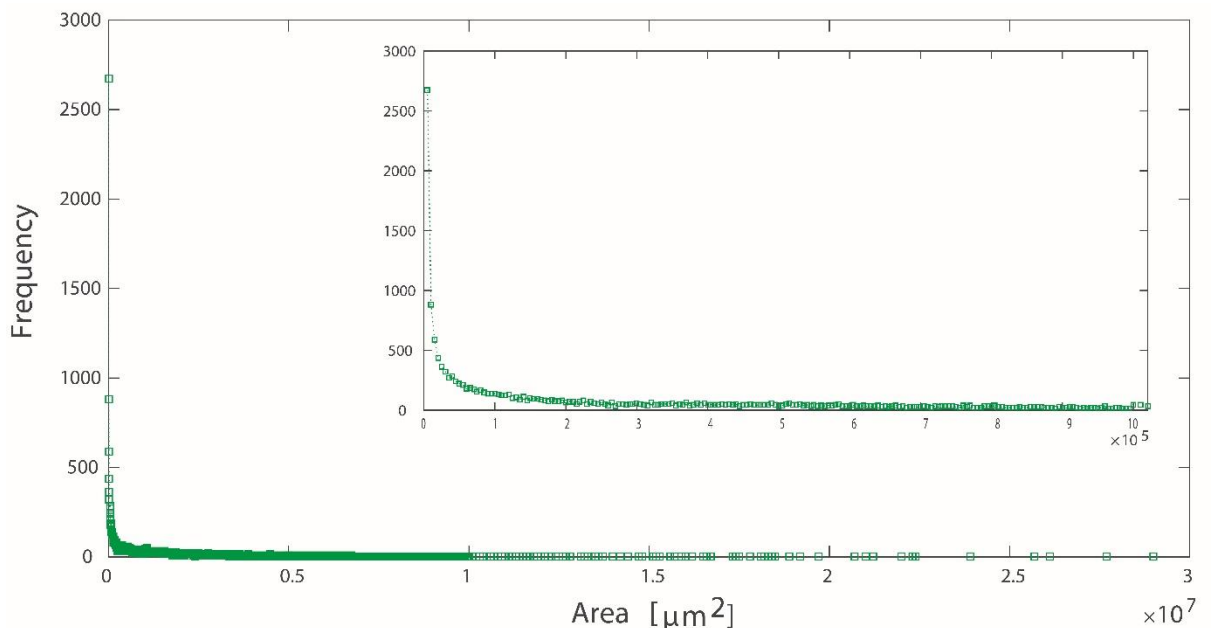
Figure 78 – Particle area histogram of tomography volume. X axis is area in µm^2 and Y axis is particle frequency. The histogram was constructed using size bins of 5000 µm^2.

4.5.1.2   Comparison of tomography stack & tomography volume

The mean equivalent diameter of the particles in the tomography stack is 28% larger than the mean of

the tomography volume (Table 8). The median particle size is also larger in the stack than the

tomography volume (40%). The mode values are very close in both data sets.

Table 8: Quantitative evaluation of particle equivalent diameter in tomography volume and stack. Values are given in µm for equivalent diameter.

Equivalent Diameter [µm]	Mean	Median	Mode
3D stacks	497	443	27
3D volume	358	266	23

Figure 79 – Equivalent diameter histogram of particles in the tomography stack and the tomography volume. X axis is equivalent diameter in µm and Y axis is relative frequency, normalised to the number of particles in the data sets. The histograms were constructed using size bins of 50 µm.

The equivalent diameter histogram shows that the distribution of particle sizes is similar in the stack

and in the volume (Figure 79). The figure plots relative particle frequency in per cent, the frequency is

normalised to the total number of particles in each data set. Both samples have a maximum relative

frequency of small particles (< 50 µm) and a low relative frequency for large particles. For particles <

400 µm, there is a higher relative abundance of particles in the tomography volume. For particles > 400

µm, there is a higher proportion of particles in the tomography stack. The stack underestimates the

number of small particles but overestimates for medium to large particles. For equivalent diameters > 1300 µm, both distributions are similar with few large particles.

The mean, median and mode values for equivalent diameter and area of the particles in the tomography volume are shown in Table 9. The mean particle area in the stack is 67% larger than for the tomography volume and the median particle area in the stack is 64% larger than for the tomography volume. The mode particle area is equal for both data sets. This means that the area statistics for the stack are strongly affected by larger particles and that the particle area statistics in the tomography stack are significantly overestimated, compared to the particle area in the tomography volume.

Table 9: Quantitative evaluation of particle area in tomography stack and volume. Values are given in $µm^2$.

Area [$µm^2$]	Mean	Median	Mode
3D stack	$2 \cdot 10^6$	$9.4 \cdot 10^5$	676
3D volume	$1.2 \cdot 10^6$	$3.4 \cdot 10^5$	676

The area histograms are not plotted as they are not visually interesting and do not provide more information than Table 9.

4.5.2 Crystal size distribution

4.5.2.1 Tomography volume

The CSD of the particles in the tomography volume resembles a very flat negative asymptote (Figure 80). The distribution shows a general decrease in frequency for increasing particle size with variations in slope. The peak in the CSD matches the mode equivalent diameter ($\leq 50\,µm$). The slope of distribution flattens out for a local maximum at 400 µm, which is followed by an increase in slope for large particles (1100 µm). Most particles have an equivalent diameter smaller than 1500 µm. For particles larger than 1500 µm, the size distribution becomes noisy, but the fluctuations are smaller than the error bars. There are few large particles. The confidence intervals at 95%, illustrated by the error bars are small for small particles and increase in size for larger particles.
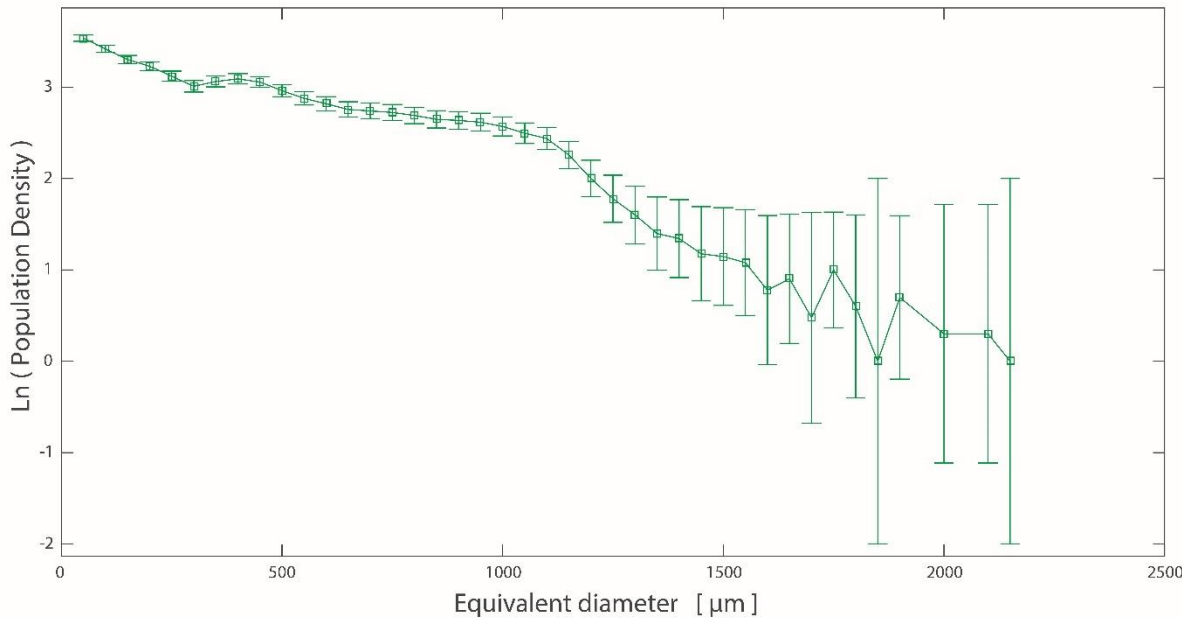
Figure 80 – Crystal size distribution particles in the tomography data. The size of the particles was evaluated using equivalent diameter. X axis is equivalent diameter in μm and Y is the logarithm of the frequency. The error bars correspond to confidence intervals of 95%.

4.5.2.2 Comparison of tomography stack & tomography volume

The 3D volume has many more particles than the 3D stack, but the size distributions follow the same trend (Figure 81). The 3D volume CSD is smoother than the CSD of the stack. For particles larger than 1350 μm, the stack CSD becomes noisy whereas the volume CSD only becomes noisy for particles larger than 1600 μm. For large particles, the CSDs of both samples become closer although there are still more larger particles in the 3D volume.
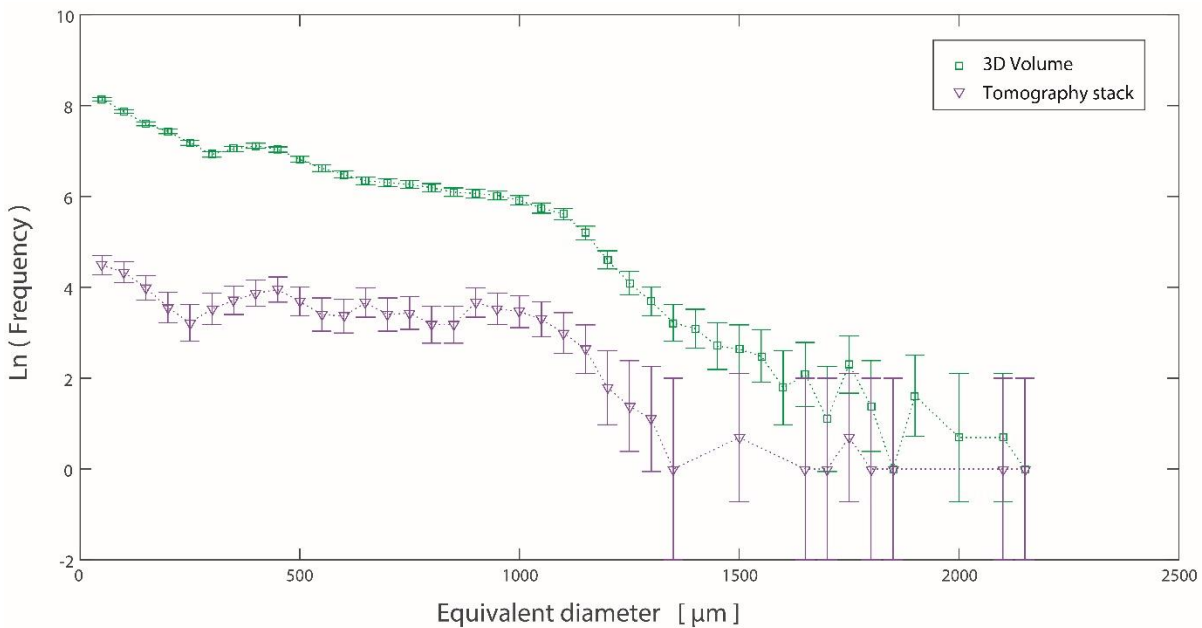
Figure 81 – Crystal size distribution of particles in the tomography stack and the tomography volume. The size of the particles was evaluated using equivalent diameter. X axis is equivalent diameter in μm and Y is the logarithm of the frequency. The error bars correspond to confidence intervals of 95%.

117

4.5.3 Packing and mush structure

4.5.3.1 Tomography volume

The 3D pair correlation function for the tomography volume starts with a narrow negative asymptote for r~0, then g(r) rapidly increases to form a wide peak of g(r)=1.4 at r=600 µm (Figure 82). The function then tends towards 1 with a negative slope. Around r=1000 µm, g(r) shows a light inflection until it crosses the spatial randomness line (g(r)=1) at r=1300 µm. This dip is a statistical artefact probably due to the resolution of the discretisation of the sample and should therefore not be considered for the interpretation (Mattfeldt & Stoyan, 2000). In theory, for high r values, the function should tend to 1 as any spatial correlation should disappear for large distances. Due to the shape of the PCF, there is no indication of the particle hardcore in the data. The trends observed are statistically significant as the tomography volume pair correlation function is outside of its uncertainty envelopes.
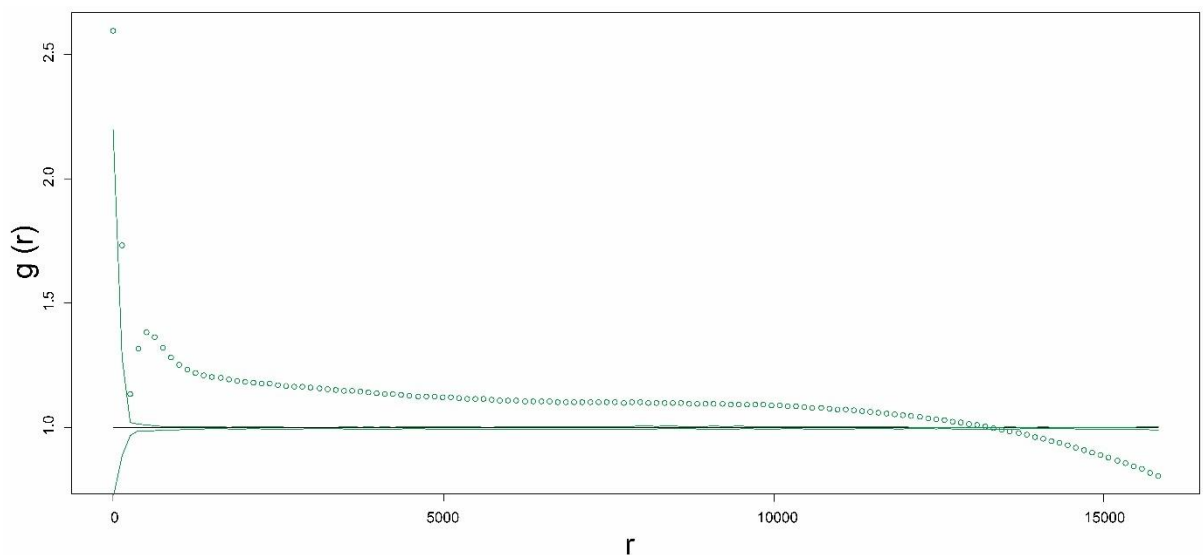
Figure 82 – Pair correlation function for the tomography volume. The function is represented by the small circles. The straight line at g(r)=1 corresponds to total spatial randomness and the lines around that line are the uncertainty envelopes. These correspond to 39 simulations of completely spatial randomness, representing, therefore, confidence intervals of 95%. X axis is the radius in µm and Y axis is the g(r) function.

4.5.3.2 Comparison of tomography stack & tomography volume

The pair correlation function for the tomography volume and the stack are similar in shape with a negative asymptote leading directly to a wide peak (Figure 83). The peak of both datasets is at r = 800 µm but the peak of the tomography stack PCF has a higher amplitude (g(r)=2) than the peak in the tomography volume data (g(r)=1.4). The stack PCF is shorter as the data set is smaller. The tomography volume pair correlation function lies outside its uncertainty envelopes meaning the trend observed is

statistically significant, however, only the peak of the tomography stack pair correlation function is only outside the simulation envelopes, so only the peak is statistically relevant.

Figure 83 – Pair correlation function for the tomography stack (purple), tomography volume (green) and their corresponding simulation envelopes. The black line represents total spatial randomness g(r)=1, above that line represents a clustering of crystals in the sample and below that line represents ordering in the sample.

## 4.5.4   Shape

4.5.4.1   Tomography volume

The particles in the tomography volume are sub-rounded to angular with shape factors of 1 to 15 with outliers reaching 50 (Figure 84, left). Most of the particles have a shape factor between 1 and 15, independent of size. The particles with shape S > 15 correspond to small particles, with diameters from 100 to 500 µm (Figure 84, left). Shape factors S > 30 correspond to either elongated particles or particles affected by the cropping of the sample, artificially giving them an elongate shape.

There is a marked correlation between length and width in the thin section (Figure 84, right). The majority of the data forms a wedge with slopes ranging from 0.74 to 0.56, and outliers are scattered below the wedge. The positive correlation means that the longer the particle the wider it is. There are few particles outside the general trend, and these can be linked to the particles with high shape factors.

Figure 84 – Left: Shape factor for each particle plotted against area. X axis is shape factor, a dimensionless number and Y axis is area in µm². Right: Length and width of particles plotted against each other. X and Y axis are in µm.

4.5.4.2   Comparison of tomography stack & tomography volume

Both data sets have similar sub-rounded particles. They both show a size-independent distribution of shapes followed by a tail of data points leading to higher shape factor values (Figure 85). The particles in the stack are rounder with shape factors ranging 1 to 10 while the tomography volume has a broader shape factor distribution (1 to 15). The tail of small particles visible in both data sets tends to high shape factors (55 for both but outliers at 80 and 120 for the tomography stack). The large shape factor values belong to particles with an equivalent diameter smaller than 200 µm and are associated with elongated particles. Particles on the side of the sample are cut when the data was cropped and are therefore artificially elongated.

A length-width correlation is observed in both 3D data sets. The data is spread on a broad line with slope ranging from 0.74 to 0.56. The positive correlation means that the longer the particle the wider it becomes. This is in accordance with the relatively small shape factor values (see above). There is a cloud of outliers that do not conform to the length-width trend in both 3D data sets. The outliers form a very broad trend with a flat slope and correspond to elongated particles (high length value and low width).
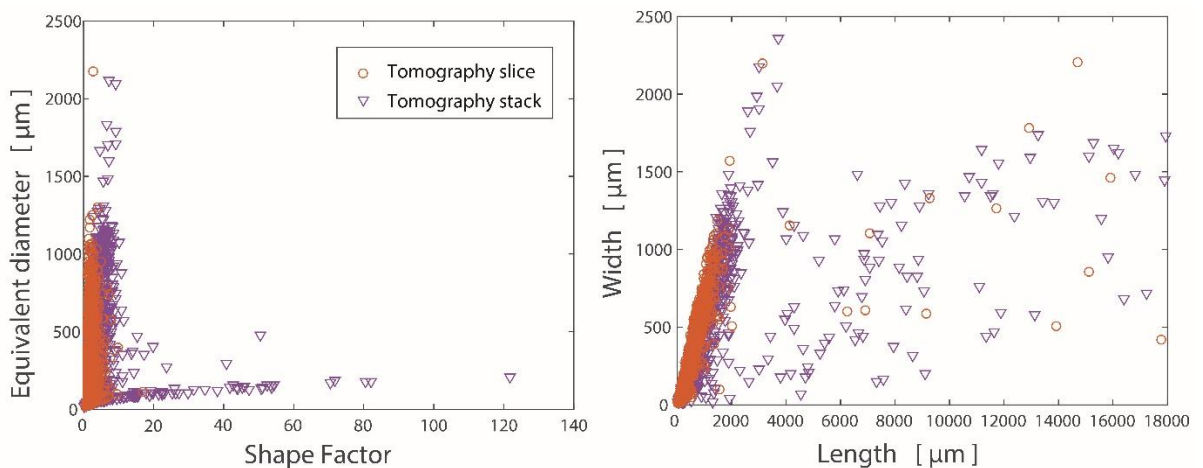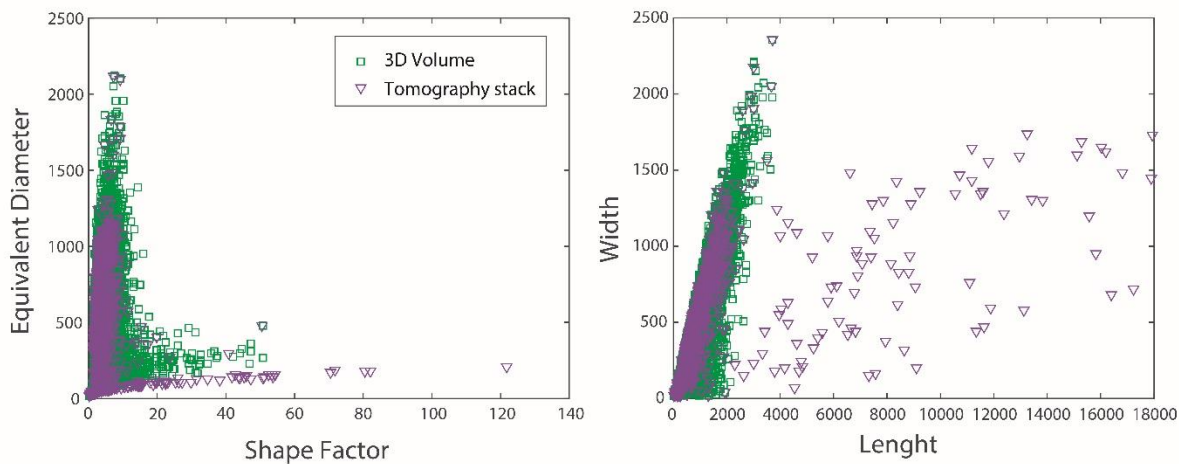
Figure 85 – Left: Shape factor for each particle plotted against area. X axis is shape factor, a dimensionless number and Y axis is area in μm². Right: Length and width of particles plotted against each other. X and Y axis are in μm.

4.5.5 Summary of stack to volume comparison

The tomography slice and stack have particles with similar attributes. However, the equivalent diameter and the area statistics of the particles in the stack are significantly overestimated compared to the tomography volume statistics (up to 67% difference). The proportion of particle size is different: proportionally, there are more large particles in the stack than in the whole volume and fewer smaller particles. The shape of the particles and the packing of the particles are well represented in the stack.

4.6 Comparison of 2D to 3D: thin section and tomography volume

The comparison of the thin section and the 3D volume is twofold: i) using the 3D prediction from the thin section, the accuracy of the tomography data processing is being evaluated; ii) to test for the pertinence of studying a thin section to understand the textures in a 3D sample.

4.6.1 Bulk statistics

The mean equivalent diameter of the thin section is smaller than that of the total 3D volume (Table 10). The median is smaller as well, but closer. The difference is of 27% for the mean and 18% for the median. The mode is 79% higher in the thin section.

Considering the sieved thin section (whose particles represent best the particles present in the tomography) in comparison with the total tomography volume helps to interpret where the differences between the thin section and the 3D volume data come from. Namely, whether the difference is due to the processing of the tomography data or is real in terms of 2D to 3D conversion.

For the sieved thin section, the statistics are closer to those of the tomography volume. The mean equivalent diameter is only slightly higher in the sieved thin section (10%) and the median is significantly higher in the sieved thin section with a difference of 24%. The mode of the sieved thin section particle size is widely overestimated, by 92%.

Table 10: Quantitative evaluation of particle equivalent diameter in the thin section, sieved thin section and 3D volume. Values are given in μm.

Equivalent Diameter [μm]	Mean	Median	Mode
Thin section	261	218	109
Sieved Thin section	399	350	~300
3D volume	358	266	23

The equivalent diameter histogram shows the thin section, as well as the sieved thin section histograms, are humped unlike the tomography volume histogram (Figure 86). This shows the difference in the mode for the three data sets. There are proportionally more small particles (0-600 μm) in the thin

section data and sieved thin section than in the tomography volume. For larger particles (> 600 μm), the histograms become similar with decreasing frequency for increasing equivalent diameter.
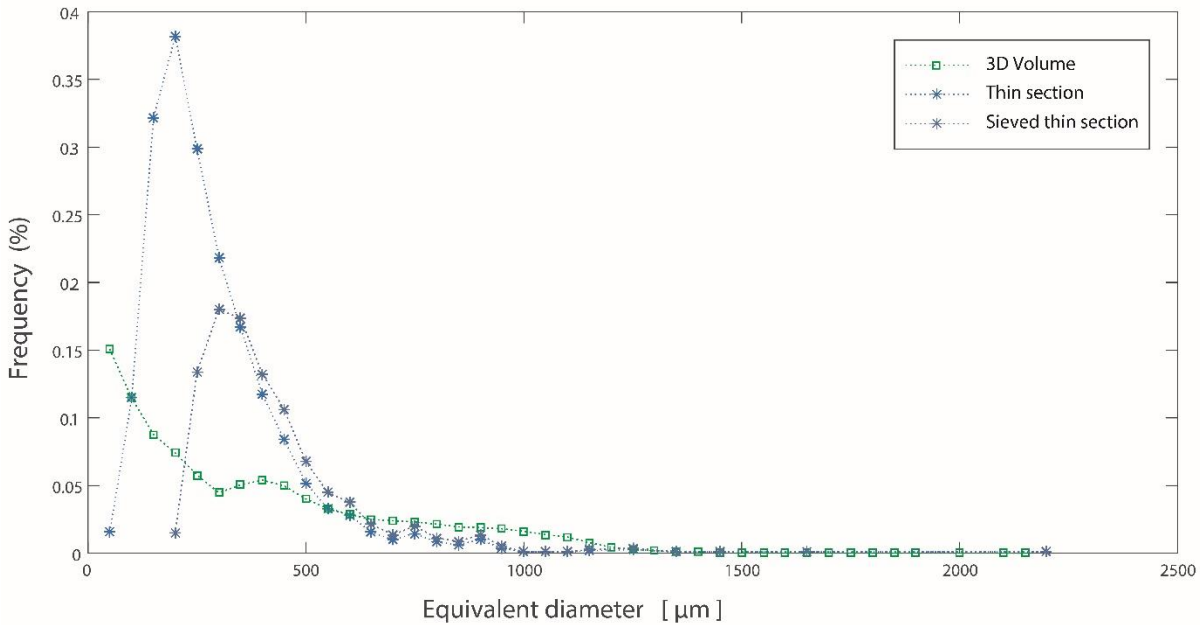
Figure 86 – Equivalent diameter histogram of particles in the thin section, the sieved thin section and the tomography volume. X axis is equivalent diameter in μm and Y axis is frequency. The histograms were constructed using size bins of 50 μm.

4.6.2 Crystal size distribution

CSD graphs provide the distribution of particle sizes in each data set. Using the stereological conversion of 2D data to generate 3D data (cf. section 3.4.1.3), the projected thin section can be compared to the 3D volume. The stereological conversion method used to generate the 3D data could have a bias. To test this, the tomography slice data is projected in 3D and the resulting CSD is compared to 3D volume CSD (Figure 87).

4.6.2.1 Testing bias on the stereological conversion

First, a baseline of the differences between the tomography slice and the 3D volume is established using an equivalent diameter proportional histogram (Figure 87, top). In general, the two histograms have a similar slope. For particles smaller than 150 μm, the tomography slice has proportionally fewer particles than the 3D volume; but for particles with an equivalent diameter between 250 μm and 850 μm, the tomography slice has more particles than the 3D volume. For particles > 900 μm, there are proportionally fewer large particles in the tomography slice.
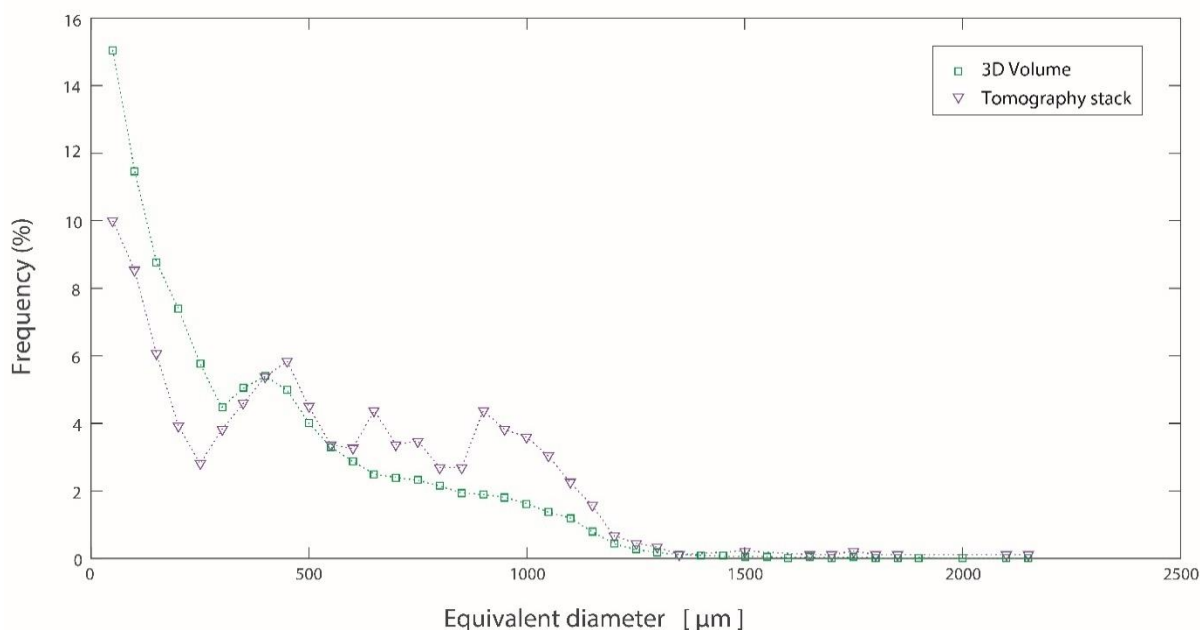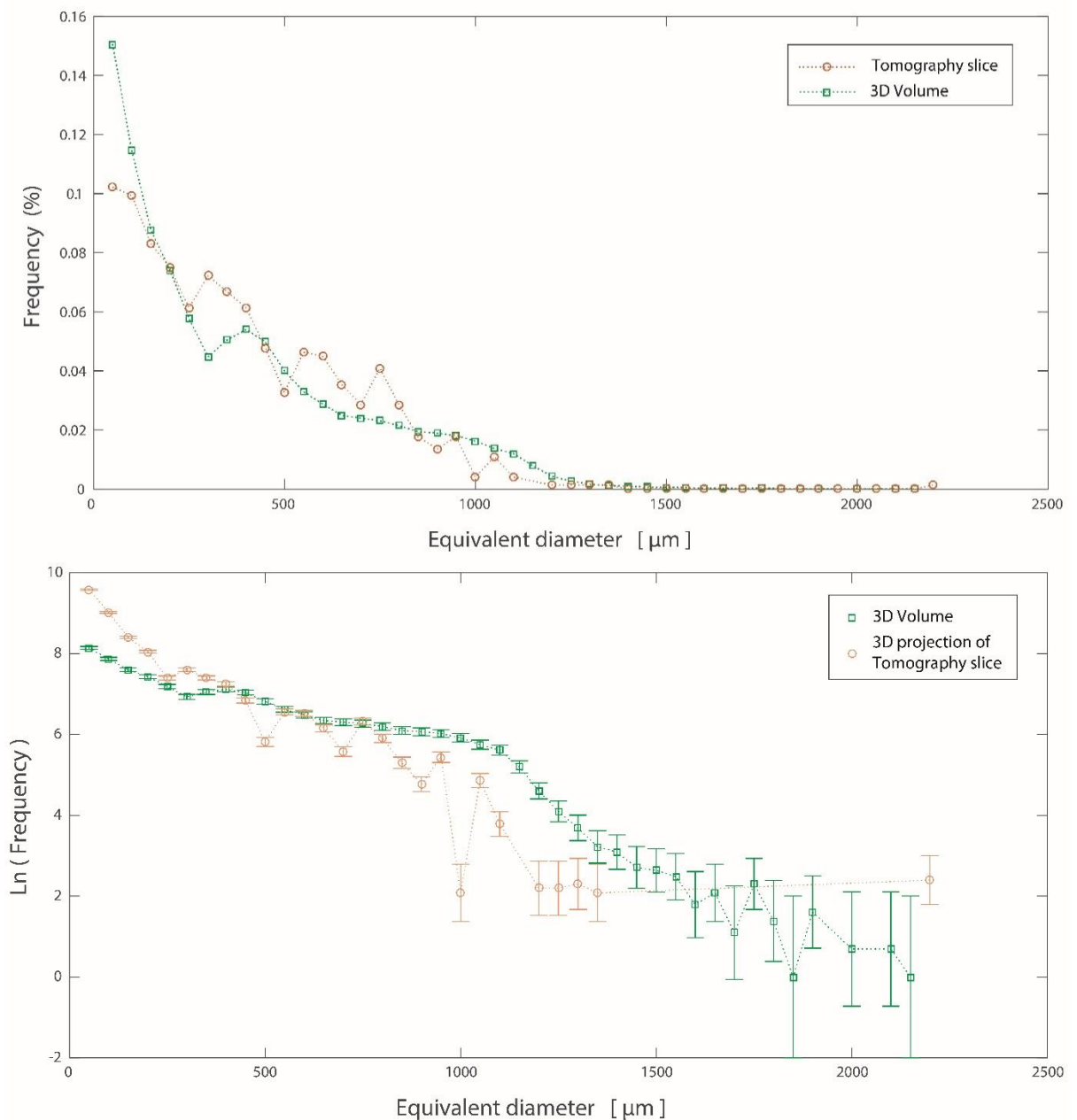
Figure 87 – Top: Equivalent diameter histogram of particles in tomography slice and the tomography volume. X axis is equivalent diameter in μm and Y axis is frequency. The histograms were constructed using size bins of 50 μm; Bottom: Crystal size distribution of particles in the tomography volume and the 3D conversion of the tomography slice data. The size of the particles was evaluated using equivalent diameter. X axis is equivalent diameter in μm and Y is the logarithm of the frequency. The error bars correspond to confidence intervals of 95%.

Knowing the difference in distribution between the tomography slice and the 3D volume, the 2D data projected in 3D compared to the real 3D data will show if the conversion has a bias. The projected tomography slice CSD is close to the 3D volume CSD (Figure 87, bottom). For small particles (<500 μm), the projected tomography slice overestimates the number of particles significantly as the tomography slice was observed to have fewer small particles than the tomography volume in the histogram (Figure 87, top). For medium to large particles ranging 500 μm to 1550 μm, the 3D projected tomography slice underestimates the number of particles. From particle sizes > 1600 μm, the CSDs are similar.

The comparison of the 3D projected tomography slice CSD with the 3D volume CSD reveals a bias in the conversion used. The number of small particles is significantly enhanced leading to an overestimation of their numbers, while the number of larger particles is much less increased. The numbers for the largest particles in the projected data are erroneous and should not be considered. This bias in the conversion has to be considered for the comparison of the thin section CSD to the 3D volume.

4.6.2.2   Thin section to 3D volume CSD comparison

The CSD of the projected thin section has a steeper slope than the 3D volume CSD (Figure 88). The projected thin section CSD starts at higher frequencies for small particles (< 150 µm) and quickly decreases in frequency as the particle size increases. This means that there are more small particles (150 µm to 550 µm) in the projected thin section than in the 3D volume. For medium to large particles (550 µm to 1450 µm), the number of particles in the 3D projected thin section is lower than in the 3D volume. The curve of the projected thin section also becomes noisy for these particle sizes. For particles >1500 µm, the CSDs are similar. The projected sieved thin section data in 3D compared to the tomography volume results in the same differences: more small particles and less medium to large particles than in the tomography volume.

Considering the observed bias on the stereological conversion method, the higher abundance of small particles in the original and sieved thin section can either be real or an artefact of the bias in the conversion. The scale of the overabundance of small particles in the thin section, however, points toward a real trend and the histogram also shows that the thin section has more small particles. The higher frequency of small particles can also be observed for the projected sieved thin section, so the trend is most likely real. This means that the particles in the tomography volume are not separated enough yet (under-separation in the tomography).
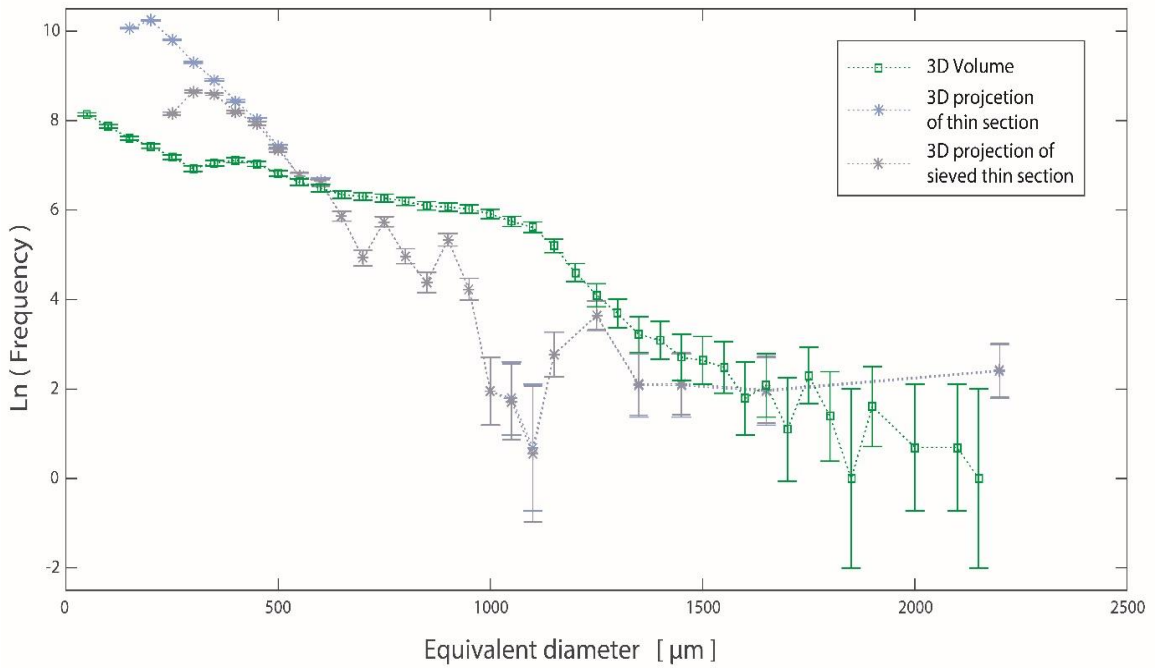
Figure 88 – Crystal size distribution of particles in the tomography volume, the 3D conversion of the thin section and the 3D conversion of the sieved thin section. The size of the particles was evaluated using equivalent diameter. X axis is equivalent diameter in µm and Y is the logarithm of the frequency. The error bars correspond to confidence intervals of 95%..

4.6.3 Packing and mush structure

Figure 89 shows the pair correlation function, with uncertainty envelopes representing 39 simulations of completely spatial randomness and thus confidence intervals of 95%.
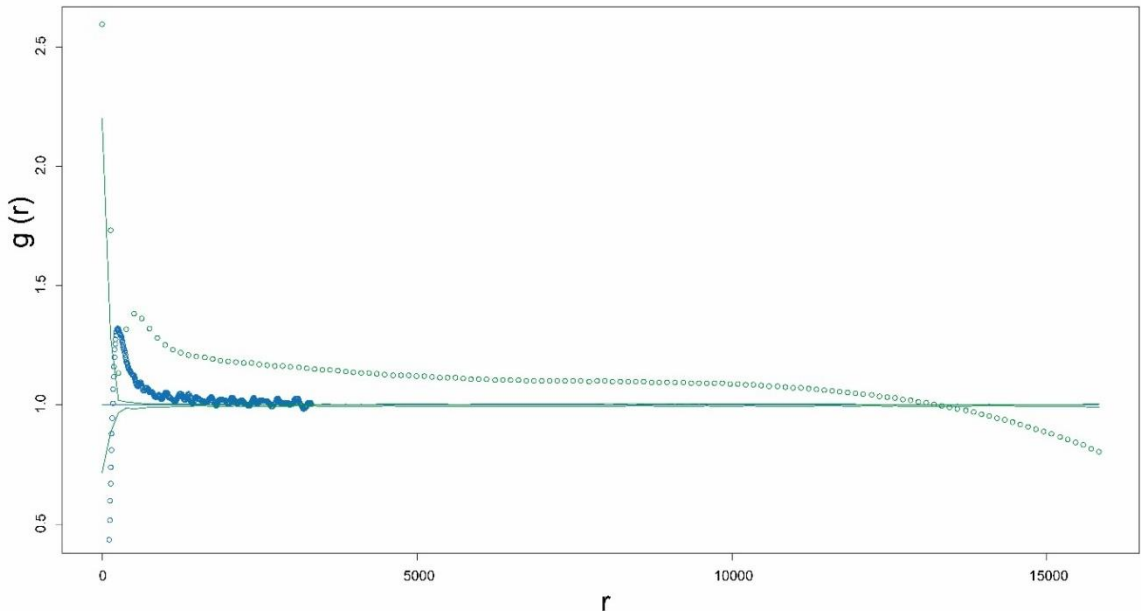
Figure 89 – Pair correlation function for the thin section (blue), tomography volume (green) and their corresponding simulation envelopes. The black line represents total spatial randomness g(r)=1, above that line represents a clustering of crystals in the sample and below that line represents ordering in the sample.
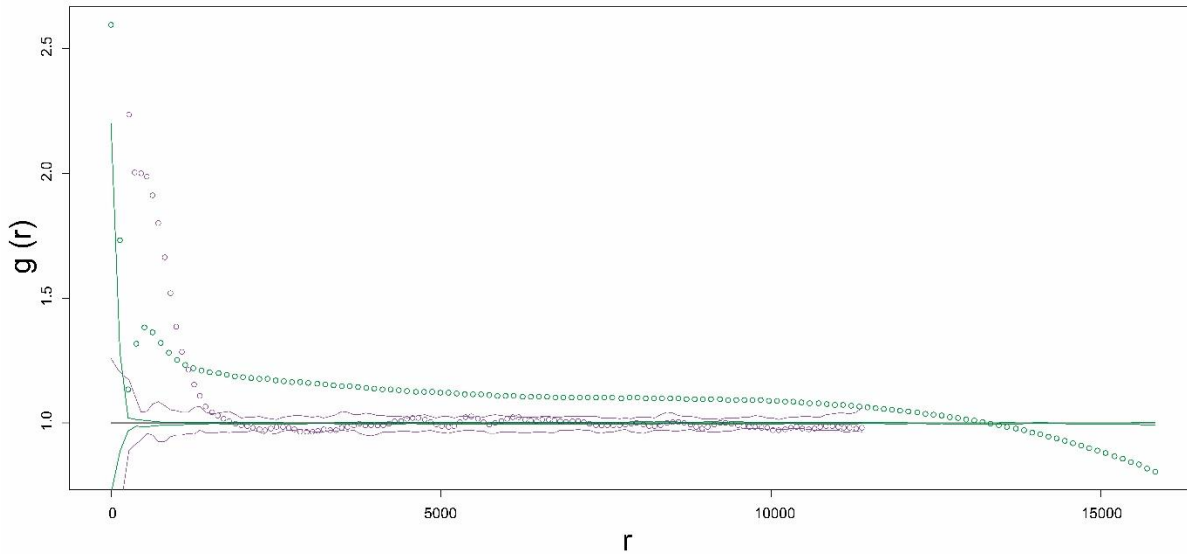
The pair correlation function for the tomography volume and the thin section have the same general shape but the thin section PCF starts at g(r) = 0 at r ~20 μm. The peak in both data sets is at a similar height but shifted in r. The thin section peak is at r = 250 μm while the tomography volume PCF peak is at r = 800 μm. The thin section PCF is considerably shorter due to its smaller size. The tomography volume and thin section pair correlation functions are outside the uncertainty envelopes meaning that both trends are statistically significant.

4.6.4   Shape

Particles are rounder in the thin section than in the 3D volume (Figure 90). The thin section has shape factor values around 1 for all sizes, whereas the 3D volume particles range from 1-12 for all sizes and have a spread of data towards larger shape factors (up to 50) for small particles (150 – 400 μm). The large shape factor values belong to particles with an equivalent diameter smaller than 500 μm and are associated with elongated particles. Particles on the side of the sample are cut when the data was cropped and are therefore artificially elongated.

The thin section and 3D volume both have a marked length-width correlation, the trend being wider for the 3D volume than the thin section. The data is spread on a broad line with slope ranging from 0.79 to 0.56. The positive correlation means that the longer the particle the wider it is as well. This is in accordance with the small shape factor values.
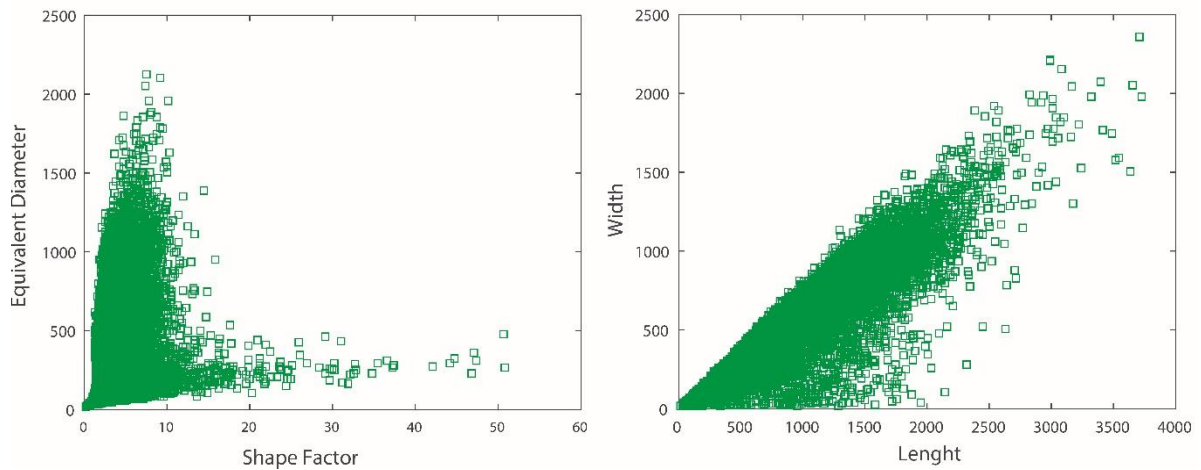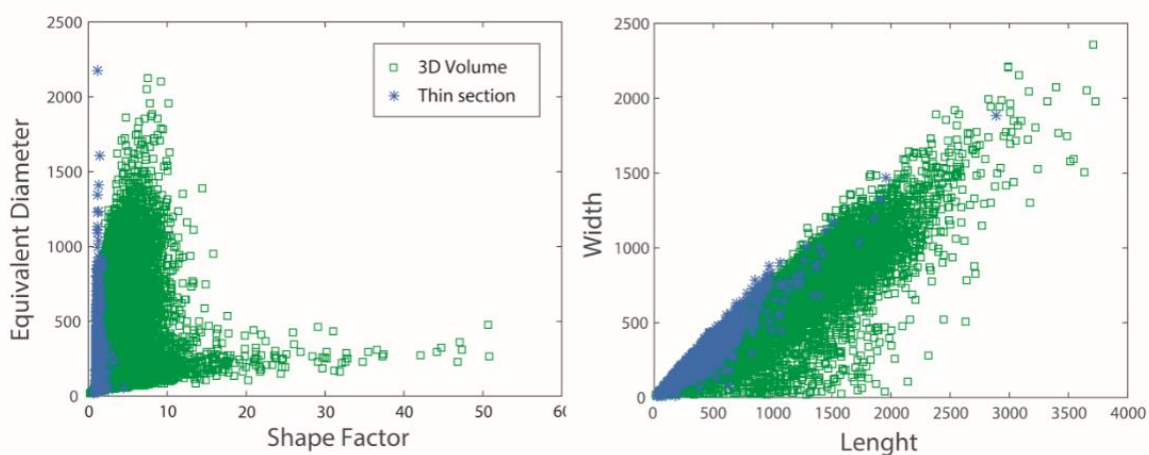

Figure 90 – Left: Shape factor for each particle plotted against area. X axis is shape factor, a dimensionless number and Y axis is area in μm². Right: Length and width of particles plotted against each other. X and Y axis are in μm.

4.6.5　Summary of thin section to volume comparison

The thin section area and equivalent diameter statistics are significantly lower than for the tomography volume but are relatively close when considering the sieved thin section. The histogram and CSD show a higher frequency of small particles in the original and sieved thin section. This is explained by under-separation of particles in the tomography volume. Particle shape are similar but more less rounded in the tomography. The pair correlation functions have different length but a similar peak.

5   Discussion

This discussion is presented in three parts to reflect the main objectives of this study: to evaluate the method for producing the 3D tomography datasets and data processing; to assess the quality and accuracy of the 3D result; and to discuss the pertinence of using tomography as a tool for igneous petrology.

5.1   Critical reflection on the methods and the impact on quality and accuracy of 3D result

The data processing of the reconstructed tomogram is essential to binarise olivine in the core, separate the binarised olivine into individual particles and then extract the dimensional measurements for the particles. Processing the tomography data is highly dependent on the image quality, spatial resolution, artefacts … (Wildenschild and Sheppard 2013). There is no optimum choice of methods and workflow, they depend on the aim of the study and the data itself. This makes the processing steps subjective and the results hard to reproduce.

5.1.1   Post-processing

The x-ray tomography acquisition had to be performed at low energies (35-70 keV) to maximise the difference in greyscale value for each of the phases as the densities of the rock-forming minerals (especially olivine and clinopyroxene) are close. Despite this, the distinction between phases remains difficult (see section 3.3.3). The drawback of this method is that the resulting greyscale 3D data is noisy. Lower energies mean generally mean a lower x-rays flux and lower transmission of x-rays in the sample. This gives the greyscale image a grainy texture (Figure 11). Projection acquisition times can be increased to improve signal-to-noise ratios, but this can mean additional drift in machine behaviour and may not increase quality significantly overall.

Other methods could be applied to increase the contrast between phases with similar linear attenuation coefficients. Monochromatic x-ray energy and phase-contrast tomography scanning can enhance the contrast and boundaries between phases respectively but both generally require a synchrotron x-ray source (Cloetens *et al.*, 1997; Lagomarsino *et al.*, 1997; Fitzgerald, 2000 Arzilli *et al.,* 2016), although lab source phase contrast extraction methods are now becoming available. For the majority of studies,

access to a synchrotron or phase contrast CT will not be possible and so most petrology focussed users are likely to have to deal with noisy, relatively low contrast data on a routine basis.

The noise in the tomography data can come directly from the x-ray source, defects in the detector or from x-ray scattering from the sample or other objects in the x-ray chamber (Leu *et al.*, 2014), and can be reduced using filters. The aim of applying filters is to smooth out the greyscale within the phases, without blurring the boundaries. All the filters available in Avizo™ are tested, and the results compared. The filtered images are judged on the smoothness of the greyscale intensity within a phase as well as the sharpness of the edges. This approach is subjective and has no quantitative aspect: the best visible result is chosen.

Preferentially, the Avizo™ in-built algorithms are used. There are many edge-enhancing algorithms available from other disciplines (e.g. Li *et al.*, 2003) that could have been used to produce an even better result than our already satisfactory filtered data, but it is a balance between the quality of the result and time spend learning and applying those skills.

Applying filters alters the data so it is essential to choose the filter according to the aim of the study. The filter needs to preserve the important structures and features of the original data. It is a "*trade-off between enhancing data quality and loss of information*" (Bartscher *et al.*, 2012). The effect of filtering is well known on the signal (SNR, Sekihara *et al.*, 1982), but little studied on dimensional tomography measurements (e.g. Kruth *et al.*, 2011). Filters may also introduce a bias in the data that is not visible, even if the greyscale histogram seems better (Armstrong *et al.*, 2012). Filtering tomography data alters the raw data and can lead to smooth surfaces, data loss (Iassonov *et al.*, 2009) and errors in the dimensional measurements, especially geometry of particles of interest (Bartscher *et al.*, 2012). Uncertainty will be introduced to all quantitative analysis on filtered data but must be balanced against the uncertainty introduced by the machine noise if filtration is not applied. The influence of filtration on the results presented here has not been quantitatively assessed, but the noise level on the raw data was such that segmentation of the olivine would not have been possible without it. This is likely to be the case for most dense geological samples whether all greyscale gradients are across planar phase

boundaries (as generally the case here), at gradational or blurred boundaries (fine scale mineral intergrowth or grain boundary alteration) or within grains (compositional gradients).

5.1.2   Segmentation

In general, segmentation processes are not known for their consistency and reproducibility. The majority of tools available for segmentation require an input from the user, making them highly subjective. The quality of the result will depend largely on the quality of the tomogram – the spatial resolution of the greyscale image and noise levels. The resolution of the tomogram is optimised before acquisition of the scan, accounting for longer acquisition times for a better resolution. The noise can be controlled by filters (section 3.3.2) and the quality of the filtering will strongly influence the segmentation.

This project aims to provide a useful assessment to the average CT user, with no detailed knowledge of algorithm development to implementation and only limited time to spend on data processing. Thus the focus was on in-built Avizo™ segmentation algorithms and modules, modules also available widely in other commercial and publicly available packages.

Manual segmentation is widely used in processing geological datasets and usually requires a user selected value targeting certain greyscale values. The oxide and plagioclase segmentation could have been performed adequately using manual methods, but the application will always be strongly biased by the user (Wildenschild and Sheppard 2013). Instead, the *auto-threshold* algorithm was used. This histogram-based segmentation tool (discussed in detail in section 3.3.3) requires manual input of two greyscale values between which the algorithm computes the value of the threshold using the local greyscale environment to define the position of the phase boundary, thereby reducing the user bias. Automated methods should be used wherever possible. Even when using automated algorithms, the "best result" remains subjective as the quality of the result was judged by the user before continuing the processing and the quality threshold for any two users would always be different.

The use of a *watershed*-based segmentation on the indistinct and unsharp boundaries between olivine and clinopyroxene gave the best visual result as this segmentation tool is generally more robust to noise and low gradients (Leu *et al.*, 2014). The method requires the selection of "markers" prior to the

segmentation. These markers are selected manually and act as seeds for the region-growing watershed. These need to be present in every phase present and representative of the greyscale variability of the target phase. The manual selection introduces a user bias and subjectivity (Iassonov *et al.*, 2009).

Although reduced to the minimum, the subjectivity and user bias in the data processing makes the segmentation process unique and very hard to reproduce. They introduce uncertainty in the binarized phase geometry, which can have a significant impact on the dimensional measurements (e.g. Leu *et al.*, 2014).

5.1.3   Separation

Separation is often referred to as segmentation in the literature, making no distinction between the binarisation of volumes and the act of breaking up those binarised volumes into individual objects. In fact, very few studies progress to the separation phase in tomography data processing. A lot of studies are in material science where the authors use XRCT for accurate dimensional metrology (e.g. Schmidt *et al.*, 2010; Hiller *et al.*, 2012) and for studying flow through porous media (e.g. Iassonov *et al.*, 2009, Wildenschild and Sheppard 2013, Leu *et al.*, 2014). For many of these applications, separation of the segmented objects is unnecessary, therefore the quantification of the uncertainties on dimensional measurements of separated tomographic objects is not well constrained.

The quality of the separation depends on the quality of the segmentation performed beforehand (Ando *et al.*, 2012; Wiebicke *et al.*, 2017). The separation module is largely influenced by the geometry of the binarised object. Generally, if the shape of the target object is irregular, or if the geometry has many surface asperities non-physical and illogical separations will occur (Ando et al., 2012; Figure 15). The separation is good on isolated particles with few contacts (Jerram & Higgins, 2007), but for an aggressive separation, large particles can be arbitrarily and incorrectly split into pieces (Figure 15). This occurs when the volume density of the seed/markers for the watershed is too high, or the geometry of the particles interacts with the algorithm parameters to force an unnatural separation. For isolated particles, this can be avoided to a certain extent by using more conservative separations and higher marker extents.

The particle size variability in the sample, in this case, does not help as the small olivine clumps cannot be separated without breaking the larger particles and vice versa, which leads to either over-separated or under-separated olivine clumps. Performing the separation in size bins is the best solution to remedy this problem.

Olivine clumps with annealed boundaries are poorly separated (Figure 15). The clumps are often separated into non-logical entities – for geologic materials – due to the way the separation algorithms work (cf. Figure 13 and Figure 14). Without prior knowledge of the shape of the particles, both separation algorithms cannot separate clumps accurately (cf. Figure 13, D; Figure 14, F). Prior knowledge of the triple points, the junction of three particle boundaries, would potentially improve the quality of the separation greatly.

In a petrographic study, where shape of the particles is important, the separation as critical as the segmentation, because it controls the shape and number of particles, and thereby the accuracy of their dimensional measurements (barycentre location, size, area, perimeter, shape factor, …; Ando *et al.*, 2012). If not performed properly, the separation can introduce big errors in particle metrology.

The built-in separation algorithms used here are not optimised for the material. Target particles are closely clumped and their geometries are variable. However, compared to other geological samples the current dataset is considered relatively simple and the crystals in question close to spherical. The separation algorithms were initially developed for separating spherical objects with little contact (e.g. Jerram & Higgins, 2007). They produce better results on a less dense population of particles, and where contacts are consistent and where negative curvature on the grain surface is always caused by the contact between particles.

Other methods developed for granular materials necessitate prior knowledge of the shape of the particles. The separation then fits these into the segmented volume as best as possible (e.g.Weis and Schröter, 2017, Reimann *et al.*, 2017). The limit to this separation method is the prior knowledge of a uniform particle shape. The application of shape-based separation on a natural granular sample, like the Tugtutoq peridotite, is however beyond current implementation. A geometry-based (rather than size)

separation algorithm would be better suited for application to geological materials and could implement machine-learning style algorithms for training on a registered thin section or XRCT slice data.

Another option would be to correlate the tomography scan with x-ray crystal diffraction (3D EBSD) to provide crystallographic orientation information for each mineral (e.g. McDonald *et al.*, 2015). With this information, the segmented olivine could be easily separated along the changes in crystal lattice orientation. The accuracy of the separation result would be improved, and segmentation could also be improved. However, access to EBSD at synchrotron facilities and the rare UK based lab source is unlikely for many petrology projects, scan times are long, and interpretation of the data is non-trivial.

The segmentation and separation steps in the data processing workflow are the source of most of the errors in the dimensional measurements. The methods used are subjective and prone to unavoidable user bias. Quantitative studies on the effect of these errors on the final data output are rare, but it has been estimated that applying a threshold segmentation to binarise features of interest in XRCT can have as many as 11% of the voxels wrongly labelled (Kerckhofs *et al.*, 2008).

5.1.4 Registration of thin section

When comparing several data sets, registration is an important part of data processing. The thin section data needs to be placed correctly with regard to the tomography volume and to optimise the results, the thin section registration in the tomography volume must be as precise as possible.

Automatic registration methods in Avizo™ struggle with 2D-3D registration and, although this is under development by ThermoFisher, applications of the existing method in Avizo™ yield incorrect results even when using the normalised mutual information method designed for datasets of different modalities. The registration was done manually and while the thin section was positioned as well as possible, there may be some unquantified uncertainty. However, any error would be systematic in the barycentre location comparison. Since such a pattern is not visible in the data, any error associated with the registration would be much smaller than the uncertainties introduced by the segmentation or separation.

5.1.5 Thin section segmentation

The outline of the olivine crystals in the thin section was drawn by hand using ImageJ, a simple and effective image processing software. The drawing tool is easy to use but is highly influenced by the quality of the thin section scan. The selection line goes around the pixels making the selection angular and artificial and could influence perimeter, area and shape measurements. The thin section was scanned at high quality (pixel size is 3.7 x 3.7 μm^2). The borders of olivine crystals in the thin section are sometimes wider than one pixel, often 2 but up to 4 pixels wide. The maximum boundary width corresponds to 14.8 μm (pixel size is 3.7 x 3.7 μm^2). The wide crystal boundaries are a visual effect linked to the thickness of the thin section (30 μm), the curvature of the crystal surface creates a broader crystal boarder in the thin section, due to the projection of the sloping interface of the crystals. These crystals are more difficult to segment and can introduce errors on area, size and shape and size measurements. The effect on the particles is noticeable: the most common size in the distribution is 109 μm across, so a 4-pixel boundary would represent 14% of the size. The boundary proportion is significant, but the 4-pixel boundary is present on only a few crystals, and these are generally large. The resolution of the scan is better than that of the tomography (11.9 x 11.9 x 11.9 μm^3) so errors incurred by the drawing tool are considered negligible.

5.2 Quality and accuracy of the tomography data

5.2.1 Qualitative assessment

Overlaying the processed segmented and separated particles onto the tomography greyscale data show that while the particles are close to the raw data (Figure 91, top), there are consistent differences. The shape of the particles is generally consistent although they are systematically smaller than the olivine in the raw data. At some point during the processing, the olivine segmentation must have been overly eroded. The data loss is most probably due to an erosion step that was not properly reversed during the separation. The real olivine grain boundaries are sometimes visually obvious due to the internal gradient in the olivine crystals and very different from the separated processed data. The separated particles often have unrealistic shapes (Figure 92, B). Some particles, however, are well separated and are broken up where one would expect them to be. The thin section particles overlain over the raw tomography data shows a good correlation (Figure 91, bottom). Almost all the olivine in the tomography is accounted for in the thin section and the few differences can be explained by small errors in the registration or the thickness of the thin section with includes more crystals than the slice (no thickness).

There is a significant number of particles in the thin section that are not present in the tomography slice (Figure 93). The blue surface in Figure 93 is the segmented olivine in the tomography and below are the thin section particles. Any that are not covered by the blue surface are not present in the processed tomography data. There are particles in the thin section that are not well represented in the tomography slice and there is also an entire olivine size fraction missing in the tomography data (Figure 94, B). The difference is due to the tomography data processing, during the segmentation and the multi-stage separation. The segmentation process is a potential source for large errors, especially as the olivine was so difficult to segment from the clinopyroxene. As the separation was performed in several stages, the particles were eroded and dilated again, but if the erosion level is considerable, small particles may disappear entirely and the dilation would not have brought them back.
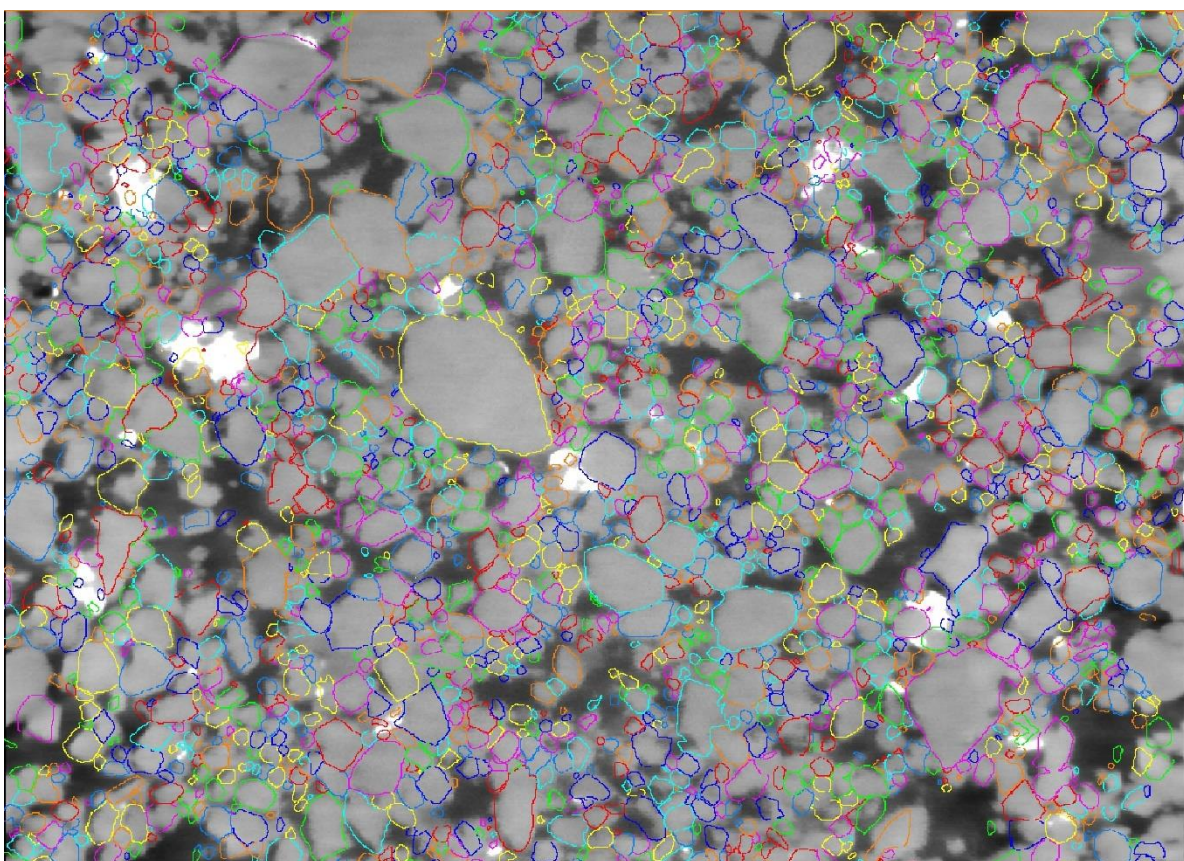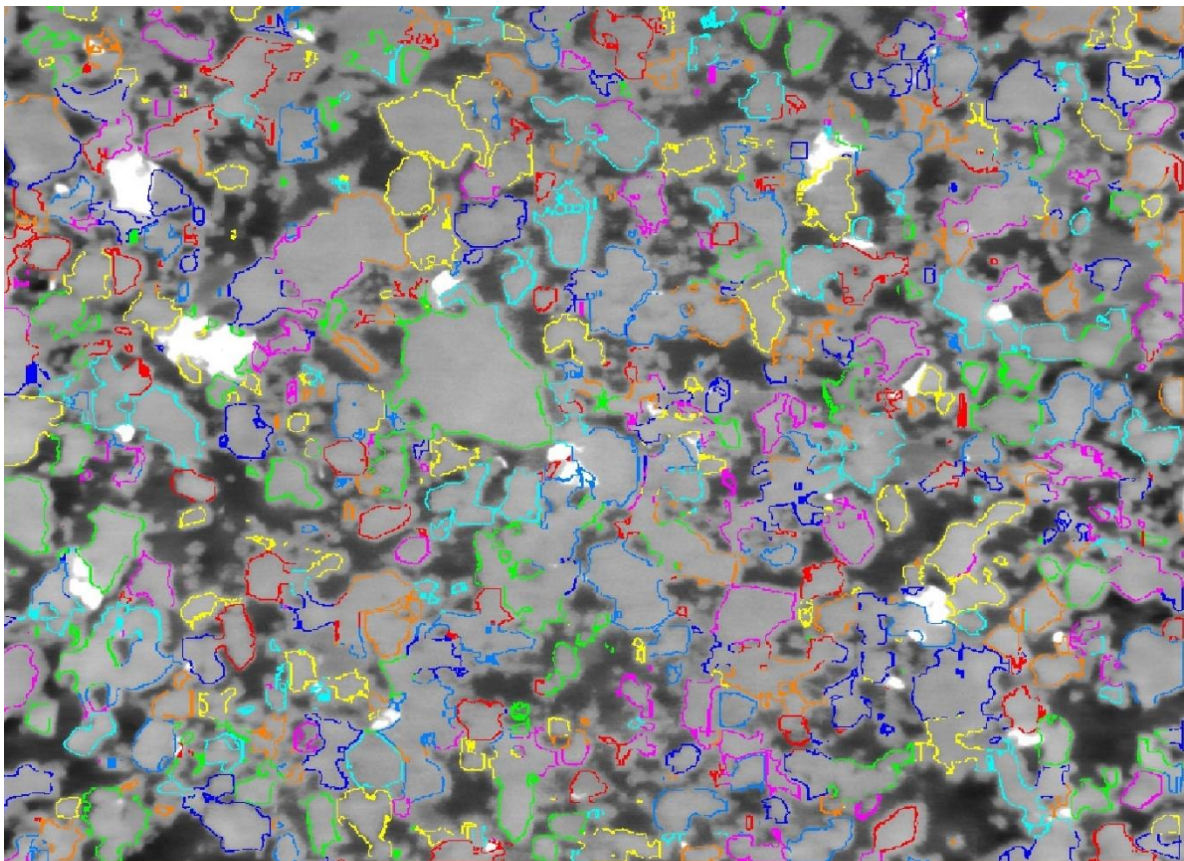
Figure 91 – Top: Outline of tomography slice particles over the raw tomography data. The change in outline means there is a change in particle. The contrast is pushed to the limit to visualise olivine better. Bottom: Particle outline in the thin section soon to be over the raw greyscale data.
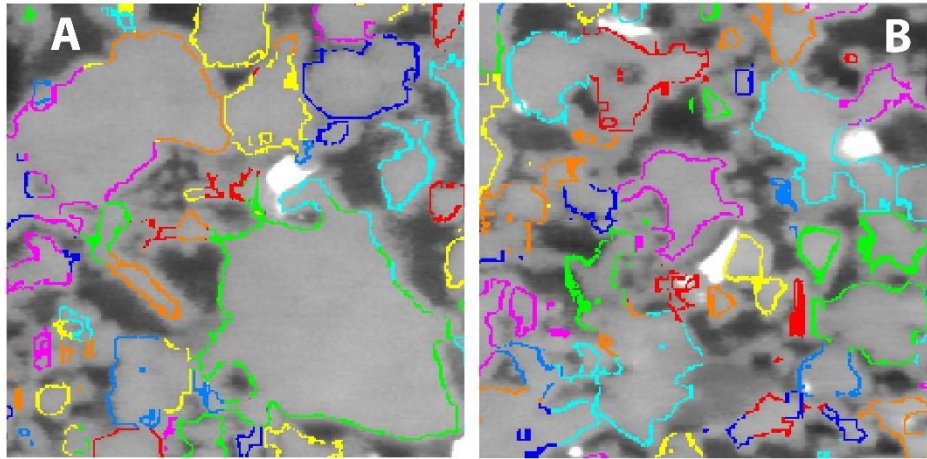
Figure 92 – Detail of separated tomography particles over raw tomography data. A: realistic separations for example, the long orange particle, the orange and the adjacent pink or the dark blue one; B: unrealistic separations, not like the usual sub-rounded olivine.
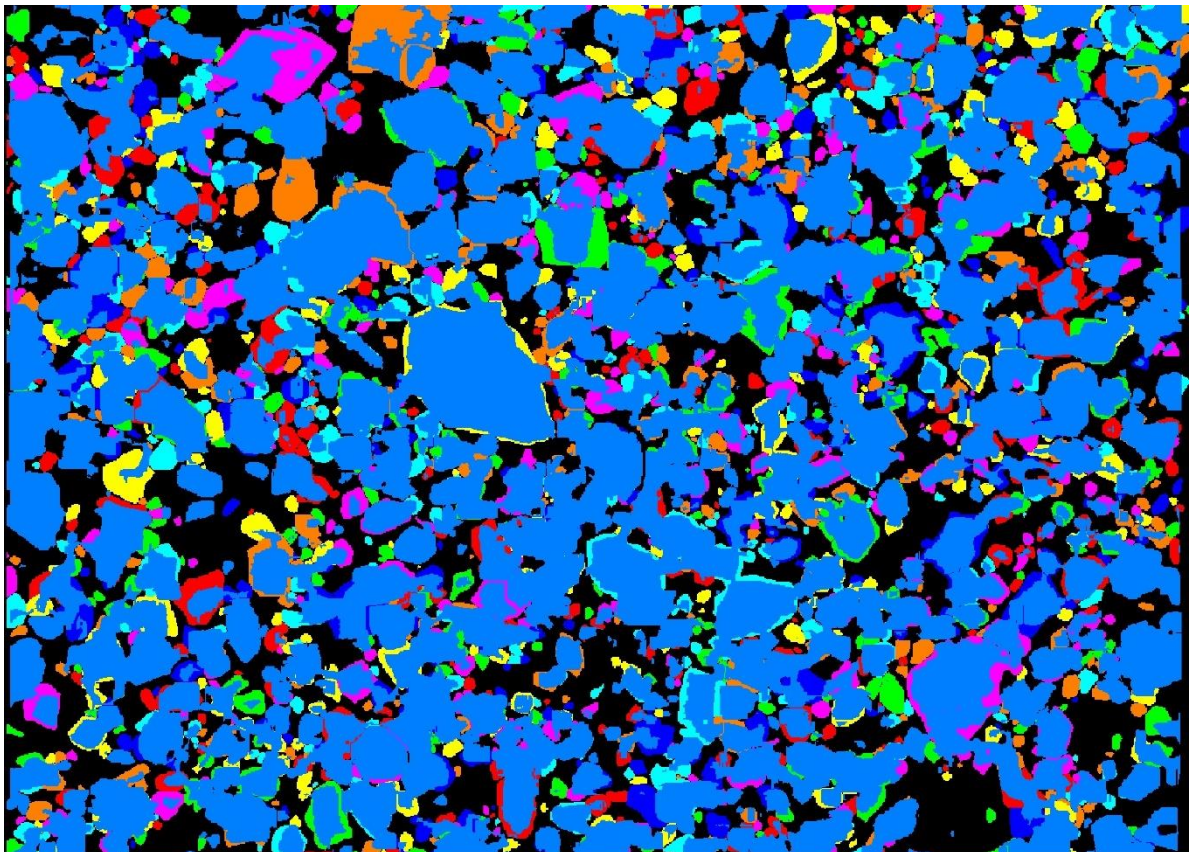
Figure 93 – Segmented olivine in the tomography slice over the separated particles in the thin section to illustrate the missing particles in the tomography data.

The particles that are only partially represented in the tomography are either particles that only represents the centre of an olivine crystal (Figure 94, B) or particles where only one side is represented in the tomography data (Figure 94, A). The former is likely a discrepancy due to the erosion and subsequent dilation of the particles where they are not restored to their original shape. In the case of the latter, where a side of a particle is represented in the tomography data but the other is not, is most

138

likely attributed to the internal gradient in the olivine crystals in the greyscale data. The source of the shadow is probably compositional differences in the olivine.
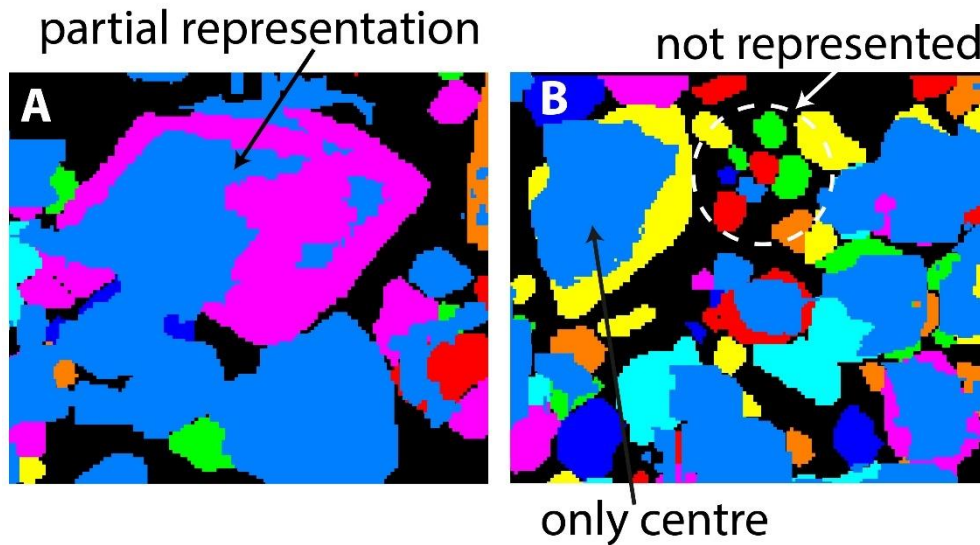
Figure 94 – Detail of the segmented olivine in the tomography slice over the separated particles in the thin section showing the partially represented particles and the missing particles in the tomography data.

The thickness of the thin section could be another explanation for the missing particles in the tomography data. While the thin section is 30 μm thick, the tomography slice is only 1 pixel thick. By transparency, olivine crystals that are not cut by the "top" of the thin section appear in the thin section segmentation but not in the tomography slice due to its lack of thickness.

The boundaries of olivine in the raw data are not sharp, sometimes there is even a gradual transition between two adjacent minerals (e.g. Figure 92, A). The greyscale gradient is likely an artefact of the tomography acquisition and how the tomography data is discretized into voxels. For voxels that are positioned just on the border between two phases of different greyscale levels, the voxel can only have one greyscale value and is assigned an average value (Ketcham & Carlson, 2001) Wide crystals boundaries are also observed in the thin section due to alteration of the olivine, which could also potentially lead to blurry crystal boundaries in the tomography data.

The presence of biotite and apatite was observed in the thin section but not in the tomography volume. The density of biotite has is on average 3.09 g/cm^3 and apatite is between 3.17 – 3.23 g/cm^3. These

values are close to the density of olivine ($3.3 - 3.4$ g/cm^3)[2] which would give them a similar attenuation coefficient, thus similar greyscale values. They could be confused for olivine in the tomography data which is a potential source of error impacting the area and the shape factor. The modal abundance of apatite and biotite is very low (1-3%), therefore the error generated is negligible compared to other sources of error (see section 5.1.1).

The qualitative differences observed between the particles in the thin section and the tomography have an impact on the dimensional metrology of the particles (numerically discussed later, section 5.2.2). The differences affect the area and perimeter of the particles in the tomography; if the perimeter is affected, the shape is as well. The barycentre coordinates are also going to be slightly wrong. In short, the segmentation and separation are crucial to the quality and accuracy of the tomography data and in this work, generate qualitative differences between the particles in the thin section and in the tomography.

5.2.2   Quantitative analysis

3.1.1.1 In 2D data

Interpreting the comparison between the thin section data and the tomography slice provides insight on the quality of the tomography scan in 2D compared to the "reference thin section", the structures, textures and size distribution visible in the thin section.

The first big difference observed is the number of grains with 2099 for the thin section compared to 735 for the tomography slice. This makes it difficult to compare the two objects, although they both have the same dimensions. Such difference in particles number raises the questions of the missing particles in the tomography data. As shown in the results, there is 24% of the area missing in the tomography slice (Table 1), even though the mean particle size is around 50% bigger in the tomography slice. In accordance with the qualitative observations above, there is no systematic loss of particles of all sizes in the tomography, but rather a distinct size fraction missing. The differences observed in the equivalent diameter histogram (Figure 31) implies that there is a very different separation process for each data set. The shift in the particle size mode between the thin section (small to medium-sized particles) and

---

[2] Source of mineral density:
https://dawn.jpl.nasa.gov/DawnClassrooms/3_instrument/pdfs/Mineral_Standards.pdf

the tomography slice (very small particles, ≤ 50 μm) implies an excess of small particles which can be explained by a too severe separation, where the particles are broken up too much. The abundance of small to medium particles (100 to 500 μm) in the thin section that is not represented in the tomography data and there are more medium-sized particles (500 to 1050 μm) in the tomography slice. These differences are due to the presence of clumps (i.e. medium-sized particles in the tomography slice) that are not separated enough, which leads to a deficiency in small to medium-sized particles.

These interpretations, however, do not take into account the missing 24% of the total area of the tomography. Therefore, the sieved thin section data sets were created to compare the attributes of only the particles that are in both the tomography slice and thin section.

The sieved thin section (125-pixel^2 area overlap sieved thin section data) is closest to the tomography slice values. This is not a surprising result, as the due to the overlap criteria, any particle below 125 pixels, equivalent to an area of 27813 μm^2, is taken out of the data set, which is where there was the most difference between the thin section and the tomography slice. Furthermore, the 125-pixel overlap thin section is not absurd as a 125-pixel area has an uncertainty of only 5% whereas any smaller area has a bigger uncertainty. Comparing the 125-pixel sieved thin section to the tomography can now provide insight into particle size distribution without having to speculate about the missing particles.

The particles in the tomography are still not separated enough when compared to the sieved thin section data. There are more small to medium-sized particles in the sieved thin section and more medium-sized particles in the tomography slice. The same conclusion as with the original thin section is reached: the clumps in the tomography data are not separated enough. The spatial distribution of the particles graphically confirms the under-separation in the tomography slice (Figure 44). The area map shows that the under-separation is characteristic of clumps of olivine crystals. This phenomenon can be linked back to the difficulties the separation algorithm has with separating clumped objects.

The pair correlation of the mush is different for the thin section data and the tomography slice, although both data sets are clustered (g(r)>1). The higher amplitude of the peak in the sieved thin section PCF suggests more clustering in the sieved thin section than in the tomography slice. The negative

asymptote for low r values in the tomography data is an artefact due to limited number of small particles.

The variability in shape and size in both sieved thin section and tomography means that they are multi-disperse systems (Sahagian *et al.*, 1989). The tomography processing does affect the shape of the particles, making them less round but they still retain their length-width correlation.

There are significant differences between the thin section data and the tomography slice, the most striking being the missing particle size fraction. Comparison with the sieved thin section provides the source of the differences: they are due to the error on the segmentation and separation.

3.1.1.1 Tomography 2D to 3D

The comparison of the tomography slice and the tomography stack is essentially comparing the same particles but from two points of view: one is in 2D (slice) and the other in 3D (stack). This provides insight on how the attributes of the particles change when considered in 2D and 3D.

The mean, median and mode values of the equivalent diameter are underestimated in the tomography slice. The difference ranges from 25 to 40 %, which is significant. This is normal, however, as a slice through a collection of 3-dimensional objects does not slice through the barycentre of each particle, thereby not taking their real equivalent diameter, but an apparent value. For irregular geometries, the maximum equivalent diameter may not even be in the same plane as the slice.

The difference observed in the particle size statistics is also visible in the equivalent diameter histogram with a higher frequency of large particles in the tomography stack. The stack also shows a higher abundance of small particles in the stack. This is considered not possible as the size of the particles is generally underestimated in 2D. This can, however, be explained by the difference in particle number between the stack and the slice. There are 157 extra particles in the stack and must account for the overabundance of small particles in the stack. The presence of the superfluous particles is due to the acquisition method of the stack. The CSDs of both data sets correlate well and reinforce the higher abundance of larger particles in the stack.

There is a slight difference in barycentre location from the slice to the stack. This is explained by the same phenomenon as above. A slice through a collection of 3D objects cannot cut through the

barycentre of each object. Barycentre location in the tomography slice is calculated using the geometry of the resulting 2D particle and does not take into account the geometry of the whole particle as the barycentre computation of the stack does. A rounded particle will not have a big shift in barycentre location between the 2D and 3D, but an elongate particle could create a significant shift. The *nncross* function yields distance between *nncross* nearest neighbours no larger than 482 μm and a mode value of 20 μm. A pixel being 11.9 x 11.9 μm^2, this corresponds to a very good correlation for barycentre location between the slice and the stack in the tomography.

The mush structure is almost identical in the tomography slice and the stack. Both PCFs even have the same hard-core distance. The shape of the particle is not affected by the whether the particles are described in 2D or 3D.

Summary of interpretation: 2D to 3D in the tomography

Apart from the particle size statistics, the attributes of particles observed in either 2D or 3D do not vary significantly. Barycentre location difference is negligible and the shape factor is not affected. The 2D version underestimates the size of the particles, a difference that can reach up to 40% of the real size. The extra information provided by the 3D is a more precise size distribution of the particles (as predicted by Holness, 1997), which is former essential for interpreting the formation history of the sample using CSD (e.g. Marsh, 1988; Cashman & Marsh, 1988); and the exact location of the barycentre of each particle, which is of little use.

5.2.2.1 In 3D on a local volume?

Comparing the tomography stack to the total tomography volume evaluates how representative the stack is of the total volume.

The overestimation of mean, median and mode in the stack is significant (up to 40% difference). The distribution reveals that the difference is largely due to the deficit in small particles and the excess of medium-to-large particles. Ideally, if the stack were perfectly representative of the total volume, the CSDs would be the same except for an upward shift of the total volume CSD. This is partially the case because the CSDs join up for large particles. The stack is therefore only partially representative of the

total volume. There is an excess of large particles in the stack. This is pure chance as the thin section was made without prior knowledge of the textures of the sample.

The mush in the stack and the volume have similar packing structures, though the stack has a higher peak which translates as a higher degree of packing. Either, locally where the stack is, the structure is more organised and the packing is more efficient; or it is an artefact due to the difference in volume. The shape of the particles in the stack is representative of particle shape in the total volume.

The stack is partially representative of the total volume except for an overabundance of large particles. This explains the overestimations of particle size and area statistics.

3.1.1.2 Thin section compared to 3D tomography volume

The accuracy of the tomography data processing is evaluated in this section by comparing the tomography volume data to the thin section by means of basic statistics. The tomography data is compared to the thin section and the sieved thin section, because, as the sieved thin section represents best the particles in the tomography slice, the sieved data determines if the source of the differences is due to the 2D-3D conversion or in the data processing.

The statistics on particle size have a significant difference (18-24%), but it is not very high. The most surprising is the difference in mode (79%). This is explained by the missing size fraction in the tomography (see Figure 93 and Figure 94, B). The statistics are closer for the comparison to the sieved thin section; the mode is ignored here as the sieving process artificially shifts the mode to higher values. The difference in equivalent diameter is due to the data processing as well as the 2D to 3D conversion.

The structure of the mush in the thin section and in the tomography volume is difficult to compare as they are so different in sample size, and there is no way of judging the source of the differences. The PCFs are however similar in aspect, though not on the same scale which could hint that both data sets have a similar structure or that the tomography volume is so much larger than the thin section that the difference in structure is compensated by the larger number of particles.

The shape of the particles is similar although the particles are rounder in the thin section. This is purely an issue with the segmentation and separation process, discussed ad nauseam in section 5.1.

5.3 Pertinence of tomography

5.3.1 How efficient is looking in 2D for understanding a 3D object?

The question of whether it is useful to acquire 3D data of a geological object when the standard method is to use thin sections is not easy to answer. The answer would be simple if one could obtain perfect 3D data, which no uncertainty on the data due to the acquisition method. The method introduces a third dimension, and so the question here is not so much whether the 3D data is useful but whether the method is good enough for it to be useful. To add an extra layer to the problem, the 2D data cannot be simply compared to the 3D data but have to be projected into a 3D data set, which introduced yet another set of potential bias and uncertainties.

The CSD of the 3D conversion of the thin section data and the tomography volume is used to discuss the pertinence of the tomography 3D data. A bias for small particles is observed in the stereological conversion, where the number of small particles in the 3D conversion is overestimated by the conversion. The bias does not seem to affect the medium particles so much and has an even smaller effect on the large particles, except for the very largest, after the break in slope, where the 3D projected data is erroneous. The bias is an artefact of the stereological conversion.

The CSDs show that there are more small particles in the thin section than in the tomography volume and slightly less medium-sized ones in the thin section. This is attributed to an under-separation of the particles in the tomography. Apart from these small differences, which are not quantified due to the unquantified bias in the conversion, the thin section CSD resembles remarkably well the tomography CSD.

The shape of the thin section CSD could lead to a different interpretation of the crystallisation history due to its almost log-normal shape (Eberl, 1998). The shape indicates that the crystals in the mush underwent continuous growth but with a decaying nucleation rate whereas the negative asymptote of the tomography volume CSD points to crystals that grew in a mush with a constant nucleation rate (Eberl, 1998). The slope of the thin section CSD is steeper than the slope of the tomography volume CSD, meaning that the particles in the thin section have a slower growth rate (e.g. Cashman and Marsh, 1988, Higgins, 2000).

There are differences in the interpretation of the CSDs which means that the 3D data can bring more information than just the thin section. The question arises of the source of these differences, however: whether they are real, due to the lack of perspective in the thin section, or an artefact of the tomography data treatment. The differences may be real but the uncertainty on the tomography data is too high. The segmentation and separation, as observed qualitatively, are a source of significant error. The sample is not adapted to the method. The segmentation of the very similar attenuation coefficients is challenging and the separation of clumped crystals is near impossible (Jerram & Higgins, 2007). A volcanic sample would maybe be more appropriate as the crystals are surrounded by groundmass and less in contact with each other. The density contrasts also would need to be higher to reduce the amount of error in the processing of the tomography data. A cumulate solidified from a more permeable mush with cumulate crystals that are barely in contact would also work, depending on the mineralogy. The method would also be well adapted to studying the spatial distribution of oxides or sulphides in a dense cumulate.

5.3.2   With more time, how could we have improved the x-ray data?

The tomography data treatment presented here took the better part of nine months. There are still many uncertainties on the data, some that could be changed with more time.

The first manipulation to add would be to find the missing particles in the tomography. These would improve the quality of the processed tomography data and with them, the tomography data would represent the thin section much better. This would take away any doubt as to the source of the differences between the 2D and 3D data: it would entirely be due to 2D to 3D conversion. We know that they were picked up by the tomography scan but lost in processing during the segmentation and separation steps.

The separation of the tomography particles is not satisfactory considering the particles represent sub-rounded olivine crystals. Ideally, the separation would be redone on a more complete tomography data using a more sophisticated separation algorithm where the shape and size ratios can be input to better constrain the shape of the separated objects. This kind of machine learning separation algorithm would

ideally be able to accommodate several types of shapes such as parallelepiped that represent plagioclase.

Another ideal separation method would be to obtain a tomography scan of the sample with x-ray diffraction. This yields the crystallographic orientation of the crystals in 3D. A better segmentation coupled with the orientation of each individual crystals would improve the uncertainty on the tomography data considerably. The separation would take place along the change of crystallographic orientation and would represent the real shape of the olivine crystals in the core.

6   Outlook of this work

There are multiple possible future applications of this work.

As we know that the peridotite was emplaced by gravity-driven slurries down the side of the dyke, we can compare the tomography processed data from this project with numerical models of hindered settling. Prof. J McElwaine modelled 3D settling of spheres (personal communication), giving the coordinates of the location of different sized spheres from which the packing structure can be deduced. This model could be used, with spheres representing the olivine crystals within the peridotite and therefore would represent the packing structure of the mush. Comparisons of the tomography data and the numerical model could potentially validate the inferred emplacement mechanism and settling velocities.

The traditional use of thin sections to describe igneous rocks is based on the assumption that the thin sections are representative of the entire sample. This assumption is rarely challenged by petrologist, but the use of tomography data, providing complete, detailed 3D vision of a sample, bypass this assumption. Using the tomography data, a sampling campaign could be used to determine the representative elemental volume – the smallest volume which represents the whole sample (Bear, 1972)

The methods of data processing used in this study would be well suited for use imaging phenocrysts in volcanic rocks. This is due to the density contrasts between different minerals and the groundmass which leads to a higher contrast in attenuation coefficients and therefore a lower error in the

segmentation of the phenocrysts. Also, as the phenocrysts commonly have minimal contact with each other, the error on their separation would also be reduced.

7 Conclusion

The x-ray tomography scan of a rock sample is the ideal method to observe structures and the distribution of features in a 3D volume. The crystal size distribution is more precise, the spatial distribution of crystals can be properly understood as well as the clustering of minerals throughout the sample. Through this method, the structure of a mush can be properly characterised.

The tomography is however not well applicable to intrusive igneous rocks. The crystals of interest are all in contact and increase the error on the 3D result. Due to the low contrast in greyscale between the different mineral phases in the peridotite, the data processing is subjective and the reproducibility is poor. These issues lead to large unquantifiable errors in the tomography data.

Applied to volcanic rocks, where crystals or bubbles are dispersed in a groundmass, the attenuation coefficient difference would be greater between the phases and would decrease significantly the subjectivity as the data processing could be almost entirely automated. The crystals would be in minimal contact to each other decreasing the error on the dimensional metrology of the crystals.

8   References

A. Baddeley, E. Rubak and R.Turner, 2015. Spatial Point Patterns: Methodology and Applications with R. Chapman and Hall, *CRC Press*

Andò, E., Viggiani, G., Hall, S. and Desrues, J., 2012. Experimental micro-mechanics of granular media studied by X-ray tomography: recent results and challenges. *Géotechnique Letters*, *3*(3), pp.142-146.

Anenburg, M., Burnham, A.D. and Mavrogenes, J.A., 2018. REE Redistribution Textures in Altered Fluorapatite: Symplectites, Veins, and Phosphate-Silicate-Carbonate Assemblages from the Nolans Bore P-REE-Th Deposit, Northern Territory, Australia. *The Canadian Mineralogist*, pp.17-38.

Armienti, P., Pareschi, M.T., Innocenti, F. and Pompilio, M., 1994. Effects of magma storage and ascent on the kinetics of crystal growth. *Contributions to Mineralogy and Petrology*, *115*(4), pp.402-414.

Armstrong, R.T., Porter, M.L. and Wildenschild, D., 2012. Linking pore-scale interfacial curvature to column-scale capillary pressure. *Advances in Water Resources*, *46*, pp.55-62.

Arzilli, F., Polacci, M., Landi, P., Giordano, D., Baker, D.R. and Mancini, L., 2016. A novel protocol for resolving feldspar crystals in synchrotron X-ray microtomographic images of crystallized natural magmas and synthetic analogs. *American Mineralogist*, *101*(10), pp.2301-2311.

Baronnet ,A., 1982. Ostwald ripening in solutions. The case of calcite and mica. *Estudios Geol 38*, pp.185-198

Bartscher, M., Staude, A., Ehrig, K. and Ramsey, A., 2012. The influence of data filtering on dimensional measurements with CT, *World Conference on Non Destructive Testing (WCNDT), Durban, South Africa*.

Bear, J., 1972. Dynamics of flow in porous media, *American Elsevier*, p. 764.

Bell, B.R., Williamson, I.T. and Trewin, N.H., 2002. Tertiary igneous activity, *The Geology of Scotland*

Beucher, S. and Lantuejoul, C., 1979. International Workshop on Image Processing: Real-time Edge and Motion Detection/Estimation, *CCET*

Blumenfeld, R., Edwards, S.F. and Ball, R.C., 2005. Granular matter and the marginal rigidity state. *Journal of Physics: Condensed Matter*, *17*(24), p.S2481.

Boorman, S., Boudreau, A. and Kruger, F.J., 2004. The Lower Zone–Critical Zone transition of the Bushveld Complex: a quantitative textural study. *Journal of Petrology*, *45*(6), pp.1209-1235.

Campbell, I.H., 1978. Some problems with the cumulus theory. *Lithos*, *11*(4), pp.311-323.

Carlson, W.D. and Denison, C., 1992. Mechanisms of porphyroblast crystallization: results from high-resolution computed X-ray tomography. *Science*, *257*(5074), pp.1236-1239.

Carlson, W.D., 1989. The significance of intergranular diffusion to the mechanisms and kinetics of porphyroblast crystallization. *Contributions to Mineralogy and Petrology*, *103*(1), pp.1-24.

Cashman, K.V. and Ferry, J.M., 1988. Crystal size distribution (CSD) in rocks and the kinetics and dynamics of crystallization. *Contributions to Mineralogy and Petrology*, *99*(4), pp.401-415.

Cashman, K.V. and Marsh, B.D., 1988. Crystal size distribution (CSD) in rocks and the kinetics and dynamics of crystallization II: Makaopuhi lava lake. *Contributions to Mineralogy and Petrology*, *99*(3), pp.292-305.

Cashman, K.V., 1988. Crystallization of Mount St. Helens 1980–1986 dacite: a quantitative textural approach. *Bulletin of Volcanology*, *50*(3), pp.194-209.

Cloetens, P., Pateyron-Salomé, M., Buffiere, J.Y., Peix, G., Baruchel, J., Peyrin, F. and Schlenker, M., 1997. Observation of microstructure and damage in materials by phase sensitive radiography and tomography. *Journal of Applied Physics*, *81*(9), pp.5878-5886.

Couch, S., Sparks, R.S.J. and Carroll, M.R., 2001. Mineral disequilibrium in lavas explained by convective self-mixing in open magma chambers. *Nature*, *411*(6841), p.1037.

Cressie, N. and Wikle, C.K., 2011. Statistics for spatio-temporal data, *Hoboken*

Daniel, C.G. and Spear, F.S., 1999. The clustered nucleation and growth processes of garnet in regional metamorphic rocks from north-west Connecticut, USA. *Journal of Metamorphic Geology*, *17*(5), pp.503-520.

DENISON, C., Carlson, W.D. and Ketcham, R.A., 1997. Three-dimensional quantitative textural analysis of metamorphic rocks using high-resolution computed X-ray tomography: Part I. Methods and techniques. *Journal of Metamorphic Geology*, *15*(1), pp.29-44.

Diggle, P.J., 1983. Statistical analysis of spatial point patterns, *Academic Press New York*

Dobson, K.J., Harrison, S.T., Lin, Q., Ní Bhreasail, A., Fagan-Endres, M.A., Neethling, S.J., Lee, P.D. and Cilliers, J.J., 2017. Insights into ferric leaching of low-grade metal sulfide-containing ores in an unsaturated ore bed using X-ray computed tomography. *Minerals*, *7*(5), p.85.

Eberl, D.D., Drits, V.A. and Srodon, J., 1998. Deducing growth mechanisms for minerals from the shapes of crystal size distributions. *American journal of Science*, *298*(6), pp.499-533.

Emeleus, C.H., 1997, Geology of Rum and the adjacent islands. *Memoir of the British Geological Survey, Sheet 60 (Scotland)4*, pp.371-407.

Emeleus, C.H. and Gyopari, M.C., 1992. British Tertiary volcanic province, *Chapman and Hall for the joint Natire Cnservation Committee*, pp. 259

Emeleus, C.H. and Troll, V.R., 2014. The Rum Igneous Centre, Scotland. *Mineralogical Magazine*, *78*(4), pp.805-839.

Emeleus, C.H. and Upton, B.G.J., 1976. The Gardar period in southern Greenland. *Geology of Greenland*, *152*, p.181.

Ersoy, O., Şen, E., Aydar, E., Tatar, İ. and Çelik, H.H., 2010. Surface area and volume measurements of volcanic ash particles using micro-computed tomography (micro-CT): a comparison with scanning electron microscope (SEM) stereoscopic imaging and geometric considerations. *Journal of Volcanology and Geothermal Research*, *196*(3-4), pp.281-286.

Farr, R.S., Honour, V.C. and Holness, M.B., 2017. Mean grain diameters from thin sections: matching the average to the problem. *Mineralogical Magazine*, *81*(3), pp.515-530.

Fitzgerald, R., 2000. Phase-sensitive x-ray imaging. *Phys. Today*, *53*(7), pp.23-26.

Godel, B., 2013. High-resolution X-ray computed tomography and its application to ore deposits: From data acquisition to quantitative three-dimensional measurements with case studies from Ni-Cu-PGE deposits. *Economic Geology*, *108*(8), pp.2005-2019.

Gualda, G.A., 2006. Crystal size distributions derived from 3D datasets: Sample size versus uncertainties. *Journal of Petrology*, *47*(6), pp.1245-1254.

Hamilton, M.A., Pearson, D.G., Thompson, R.N., Kelley, S.P. and Emeleus, C.H., 1998. Rapid eruption of Skye lavas inferred from precise U–Pb and Ar–Ar dating of the Rum and Cuillin plutonic complexes. *Nature*, *394*(6690), p.260.

Hanna, R.D. and Ketcham, R.A., 2017. X-ray computed tomography of planetary materials: A primer and review of recent studies. *Chemie der Erde-Geochemistry*, *77*(4), pp.547-572.

Hepworth, L.N., O'driscoll, B., Gertisser, R., Daly, J.S. and Emeleus, C.H., 2017. Incremental Construction of the Unit 10 Peridotite, Rum Eastern Layered Intrusion, NW Scotland. *Journal of Petrology*, *58*(1), pp.137-166.

Hepworth, L.N., O'driscoll, B., Gertisser, R., Daly, J.S. and Emeleus, C.H., 2018. Linking In Situ Crystallization and Magma Replenishment via Sill Intrusion in the Rum Western Layered Intrusion, NW Scotland. *Journal of Petrology*, *59*(8), pp.1605-1642.

Higgins, M.D. and Roberge, J., 2003. Crystal size distribution of plagioclase and amphibole from Soufriere Hills Volcano, Montserrat: evidence for dynamic crystallization–textural coarsening cycles. *Journal of Petrology*, *44*(8), pp.1401-1411.

Higgins, M.D., 1996. Magma dynamics beneath Kameni volcano, Thera, Greece, as revealed by crystal size and shape measurements. *Journal of Volcanology and Geothermal Research*, *70*(1-2), pp.37-48.

Higgins, M.D., 1998. Origin of anorthosite by textural coarsening: quantitative measurements of a natural sequence of textural development. *Journal of Petrology*, *39*(7), pp.1307-1323.

Higgins, M.D., 2000. Measurement of crystal size distributions. *American Mineralogist*, *85*(9), pp.1105-1116

Higgins, M.D., 2002. A crystal size-distribution study of the Kiglapait layered mafic intrusion, Labrador, Canada: evidence for textural coarsening. *Contributions to mineralogy and petrology*, *144*(3), pp.314-330.

Higgins, M.D., 2002. Closure in crystal size distributions (CSD), verification of CSD calculations, and the significance of CSD fans. *American Mineralogist*, *87*(1), pp.171-175.

Higgins, M.D., 2006. *Quantitative textural measurements in igneous and metamorphic petrology*. Cambridge University Press.

Hiller, J., Maisl, M. and Reindl, L.M., 2012. Physical characterization and performance evaluation of an x-ray micro-computed tomography system for dimensional metrology applications. *Measurement Science and Technology*, *23*(8), p.085404.

Holness, M.B. and Winpenny, B.E.N., 2009. The Unit 12 allivalite, Eastern Layered Intrusion, Isle of Rum: a textural and geochemical study of an open-system magma chamber. *Geological Magazine*, *146*(3), pp.437-450.

Holness, M.B., 1997. Geochemical self-organization of olivine-grade contact metamorphosed chert nodules in dolomite marble, Kilchrist, Skye. *Journal of Metamorphic Geology*, *15*(6), pp.765-775.

Holness, M.B., Hallworth, M.A., Woods, A. and Sides, R.E., 2006. Infiltration metasomatism of cumulates by intrusive magma replenishment: the Wavy Horizon, Isle of Rum, Scotland. *Journal of Petrology*, *48*(3), pp.563-587.

Hughes, E.C., Neave, D.A., Dobson, K.J., Withers, P.J. and Edmonds, M., 2017. How to fragment peralkaline rhyolites: Observations on pumice using combined multi-scale 2D and 3D imaging. *Journal of Volcanology and Geothermal Research*, *336*, pp.179-191.

Iassonov, P., Gebrenegus, T. and Tuller, M., 2009. Segmentation of X-ray computed tomography images of porous materials: A crucial step for characterization and quantitative analysis of pore structures. *Water Resources Research*, *45*(9).

Irvine, T.N., 1987. Layering and related structures in the Duke Island and Skaergaard intrusions: similarities, differences, and origins. In *Origins of igneous layering* (pp. 185-245). Springer, Dordrecht.

Jerram, D.A. and Higgins, M.D., 2007. 3D analysis of rock textures: quantifying igneous microstructures. *Elements*, *3*(4), pp.239-245.

Jerram, D.A., Cheadle, M.J. and Philpotts, A.R., 2003. Quantifying the building blocks of igneous rocks: are clustered crystal frameworks the foundation?. *Journal of Petrology*, *44*(11), pp.2033-2051.

Jerram, D.A., Cheadle, M.J., Hunter, R.H. and Elliott, M.T., 1996. The spatial distribution of grains and crystals in rocks. *Contributions to Mineralogy and Petrology*, *125*(1), pp.60-74.

Jerram, D.A., Davis, G.R., Mock, A., Charrier, A. and Marsh, B.D., 2010. Quantifying 3D crystal populations, packing and layering in shallow intrusions: a case study from the Basement Sill, Dry Valleys, Antarctica. *Geosphere*, *6*(5), pp.537-548.

Jerram, D.A., Davis, G.R., Mock, A., Charrier, A. and Marsh, B.D., 2010. Quantifying 3D crystal populations, packing and layering in shallow intrusions: a case study from the Basement Sill, Dry Valleys, Antarctica. *Geosphere*, *6*(5), pp.537-548.

Jerram, D.A., Mock, A., Davis, G.R., Field, M. and Brown, R.J., 2009. 3D crystal size distributions: A case study on quantifying olivine populations in kimberlites. *Lithos*, *112*, pp.223-235.

Jones, T.J., McNamara, K., Eychenne, J., Rust, A.C., Cashman, K.V., Scheu, B. and Edwards, R., 2016. Primary and secondary fragmentation of crystal-bearing intermediate magma. *Journal of Volcanology and Geothermal Research*, *327*, pp.70-83.

Jovanović, Z., Khan, F., Enzmann, F. and Kersten, M., 2013. Simultaneous segmentation and beam-hardening correction in computed microtomography of rock cores. *Computers & geosciences*, *56*, pp.142-150.

Kapur, J.N., Sahoo, P.K. and Wong, A.K., 1985. A new method for gray-level picture thresholding using the entropy of the histogram. *Computer vision, graphics, and image processing*, *29*(3), pp.273-285.

Kegel, W.K. and van Blaaderen, A., 2000. Direct observation of dynamical heterogeneities in colloidal hard-sphere suspensions. *Science*, *287*(5451), pp.290-293.

Kent, R.W., 1995. Magnesian basalts from the Hebrides, Scotland: chemical composition and relationship to the Iceland plume. *Journal of the Geological Society*, *152*(6), pp.979-983.

Kerckhofs, G., Schrooten, J., Van Cleynenbreugel, T., Lomov, S.V. and Wevers, M., 2008. Validation of x-ray microfocus computed tomography as an imaging tool for porous structures. *Review of Scientific Instruments*, *79*(1), p.013711.

Ketcham, R.A. and Carlson, W.D., 2001. Acquisition, optimization and interpretation of X-ray computed tomographic imagery: applications to the geosciences. *Computers & Geosciences*, *27*(4), pp.381-400.

Kretz, R., 1966. Grain-size distribution for certain metamorphic minerals in relation to nucleation and growth. *The Journal of Geology*, *74*(2), pp.147-173.

Kretz, R., 1969. On the spatial distribution of crystals in rocks. *Lithos*, *2*(1), pp.39-65.

Kretz, R., 2006. Shape, size, spatial distribution and composition of garnet crystals in highly deformed gneiss of the Otter Lake area, Québec, and a model for garnet crystallization. *Journal of Metamorphic Geology*, *24*(6), pp.431-449.

Kruth, J.P., Bartscher, M., Carmignato, S., Schmitt, R., De Chiffre, L. and Weckenmann, A., 2011. Computed tomography for dimensional metrology. *CIRP Annals-Manufacturing Technology*, *60*(2), pp.821-842.

Lagomarsino, S., Cedola, A., Cloetens, P., Di Fonzo, S., Jark, W., Soullie, G. and Riekel, C., 1997. Phase contrast hard x-ray microscopy with submicron resolution. *Applied physics letters*, *71*(18), pp.2557-2559.

Lane, A.C., 1902. Studies of the grain of igneous intrusions. *Geol. Soc. Am. Bull*, *14*, pp.369-84.

Leu, L., Berg, S., Enzmann, F., Armstrong, R.T. and Kersten, M., 2014. Fast X-ray micro-tomography of multiphase flow in berea sandstone: A sensitivity study on image processing. *Transport in Porous Media*, *105*(2), pp.451-469.

Li, H.Y., Chen, N.H., Wang, C.R., Shu, Y.H. and Wang, P.C., 2003. Use of 3-dimensional computed tomography scan to evaluate upper airway patency for patients undergoing sleep-disordered breathing surgery. *Otolaryngology—Head and Neck Surgery*, *129*(4), pp.336-342.

Lochmann, K., Oger, L. and Stoyan, D., 2006. Statistical analysis of random sphere packings with variable radius distribution. *Solid State Sciences*, *8*(12), pp.1397-1413.

Maire, E. and Withers, P.J., 2014. Quantitative X-ray tomography. *International materials reviews*, *59*(1), pp.1-43.

Mangan, M.T., 1990. Crystal size distribution systematics and the determination of magma storage times: the 1959 eruption of Kilauea volcano, Hawaii. *Journal of Volcanology and Geothermal Research*, *44*(3-4), pp.295-302.

Marsh, B.D. and Higgins, M.D., 2002. Inherited correlation in crystal size distribution: Comment. *Geology*, *30*(3), pp.284-285.

Marsh, B.D., 1988. Crystal size distribution (CSD) in rocks and the kinetics and dynamics of crystallization. *Contributions to Mineralogy and Petrology*, *99*(3), pp.277-291.

Marsh, B.D., 1998. On the interpretation of crystal size distributions in magmatic systems. *Journal of Petrology*, *39*(4), pp.553-599.

McDonald, S.A., Reischig, P., Holzner, C., Lauridsen, E.M., Withers, P.J., Merkle, A.P. and Feser, M., 2015. Non-destructive mapping of grain orientations in 3D by laboratory X-ray microscopy. *Scientific reports*, *5*, p.14665.

Mock, A. and Jerram, D.A., 2005. Crystal size distributions (CSD) in three dimensions: insights from the 3D reconstruction of a highly porphyritic rhyolite. *Journal of Petrology*, *46*(8), pp.1525-1541.

Murphy, M.D., Sparks, R.S.J., Barclay, J., Carroll, M.R. and Brewer, T.S., 2000. Remobilization of andesite magma by intrusion of mafic magma at the Soufriere Hills Volcano, Montserrat, West Indies. *Journal of petrology*, *41*(1), pp.21-42.

Pankhurst, M.J., Dobson, K.J., Morgan, D.J., Loughlin, S.C., Thordarson, T., Lee, P.D. and Courtois, L., 2014. Monitoring the magmas fuelling volcanic eruptions in near-real-time using X-ray micro-computed tomography. *Journal of Petrology*, *55*(3), pp.671-684.

Pankhurst, M.J., Vo, N.T., Butcher, A.R., Long, H., Wang, H., Nonni, S., Harvey, J., Guðfinnsson, G., Fowler, R., Atwood, R. and Walshaw, R., 2018. Quantitative measurement of olivine composition in three dimensions using helical-scan X-ray micro-tomography. *American Mineralogist: Journal of Earth and Planetary Materials*, *103*(11), pp.1800-1811.

Perona, P. and Malik, J., 1990. Scale-space and edge detection using anisotropic diffusion. *IEEE Transactions on pattern analysis and machine intelligence*, *12*(7), pp.629-639.

Polacci, M., de'Michieli Vitturi, M., Arzilli, F., Burton, M., Caricchi, L., Carr, B., Cerminara, M., Cimarelli, C., Clarke, A., Colucci, S. and Costa, A., 2017. From magma ascent to ash generation: investigating volcanic conduit processes by integrating experiments, numerical modeling, and observations. *Annals of Geophysics*, *60*(6).

Pun, T., 1981. Entropic thresholding, a new approach. *Computer graphics and image processing*, *16*(3), pp.210-239.

Randolph, A.D. and Larson, M.A., Theory of Particulate Processes (Academic, New York, 1988). *Google Scholar*.

Reimann, J., Vicente, J., Brun, E., Ferrero, C., Gan, Y. and Rack, A., 2017. X-ray tomography investigations of mono-sized sphere packing structures in cylindrical containers. *Powder Technology*, *318*, pp.471-483.

Renner, R. and Palacz, Z., 1987. Basaltic replenishment of the Rhum magma chamber: evidence from unit 14. *Journal of the Geological Society*, *144*(6), pp.961-970.

Rudge, J.F., Holness, M.B. and Smith, G.C., 2008. Quantitative textural analysis of packings of elongate crystals. *Contributions to Mineralogy and Petrology*, *156*(4), pp.413-429.

Sahagian, D.L. and Proussevitch, A.A., 1998. 3D particle size distributions from 2D observations: stereology for natural applications. *Journal of Volcanology and Geothermal Research*, *84*(3-4), pp.173-196.

Sahagian, D.L., Anderson, A.T. and Ward, B., 1989. Bubble coalescence in basalt flows: comparison of a numerical model with natural examples. *Bulletin of Volcanology*, *52*(1), pp.49-56.

Saunders, A.D., Fitton, J.G., Kerr, A.C., Norry, M.J. and Kent, R.W., 1997. The north Atlantic igneous province. *Large igneous provinces: Continental, oceanic, and planetary flood volcanism*, *100*, pp.45-93.

Schmitt, R. and Niggemann, C., 2010. Uncertainty in measurement for x-ray-computed tomography using calibrated work pieces. *Measurement Science and Technology*, *21*(5), p.054008.

Sekihara, K., Kohno, H. and Yamamoto, S., 1982. Theoretical prediction of X-ray CT image quality using contrast-detail diagrams. *IEEE Transactions on Nuclear Science*, *29*(6), pp.2115-2121.

Sparks, S.R., Sigurdsson, H. and Wilson, L., 1977. Magma mixing: a mechanism for triggering acid explosive eruptions. *Nature*, *267*(5609), p.315.

Špillar, V. and Dolejš, D., 2015. Heterogeneous nucleation as the predominant mode of crystallization in natural magmas: numerical model and implications for crystal–melt interaction. *Contributions to Mineralogy and Petrology*, *169*(1), p.4.

Stoyan, D. and Stoyan, H., 1994. *Fractals, random shapes, and point fields: methods of geometrical statistics* (Vol. 302). John Wiley & Sons Inc.

Stoyan, D. and Stoyan, H., 1996. Estimating pair correlation functions of planar cluster processes. *Biometrical Journal*, *38*(3), pp.259-271.

Stoyan, D., Kendall, W.S. and Mecke, J., 1986. *Introduction to Stochastic Geometry*. Wiley.

Taddeucci, J., Pompilio, M. and Scarlato, P., 2004. Conduit processes during the July–August 2001 explosive activity of Mt. Etna (Italy): inferences from glass chemistry and crystal size distribution of ash particles. *Journal of Volcanology and Geothermal Research*, *137*(1-3), pp.33-54.

Upton, B.G. and Thomas, J.E., 1980. The Tugtutoq younger giant dyke complex, South Greenland: Fractional crystallization of transitional olivine basalt magma. *Journal of Petrology*, *21*(1), pp.167-198.

Upton, B.G., 2013. Tectono-magmatic evolution of the younger Gardar southern rift, South Greenland. *Geological Survey of Denmark and Greenland Bulletin*, *29*(unknown), pp.001-124.

Upton, B.G.J. and Blundell, D.J., 1978. The Gardar igneous province: evidence for Proterozoic continental rifting. In *Petrology and geochemistry of continental rifts* (pp. 163-172). Springer, Dordrecht.

Upton, B.G.J., 1964. *The Geology of Tugtutôq and Neighbouring Islands, South Greenland: Part III: Olivine Gabbros, Syeno-gabbros and Anorthosites: Part IV: The Nepheline Syenites of the Hviddal Composite Dyke*. Grønlands Geologiske Undersøgelse.

Upton, B.G.J., 1987. Gabbroic, syenogabbroic and syenitic cumulates of the Tugtutoq younger Giant Dyke Complex, south Greenland. In *Origins of igneous layering* (pp. 93-123). Springer, Dordrecht.

Vincent, L. and Soille, P., 1991. Watersheds in digital spaces: an efficient algorithm based on immersion simulations. *IEEE Transactions on Pattern Analysis & Machine Intelligence*, (6), pp.583-598.

Wagner, C., 1961. Theorie der alterung von niederschlägen durch umlösen (Ostwald-reifung). *Zeitschrift für Elektrochemie, Berichte der Bunsengesellschaft für physikalische Chemie*, *65*(7-8), pp.581-591.

Wang, L., Lyons, J., Kanehl, P. and Gatti, R., 1997. Influences of watershed land use on habitat quality and biotic integrity in Wisconsin streams. *Fisheries*, *22*(6), pp.6-12.

Weis, S. and Schröter, M., 2017. Analyzing X-ray tomographies of granular packings. *Review of Scientific Instruments*, *88*(5), p.051809.

Wickham, H., 2016. plyr: Tools for Splitting, Applying and Combining Data. R package version 1.8. 4.

Wiebicke, M., Andò, E., Herle, I. and Viggiani, G., 2017. On the metrology of interparticle contacts in sand from x-ray tomography images. *Measurement Science and Technology*, *28*(12), p.124007.

Wildenschild, D. and Sheppard, A.P., 2013. X-ray imaging and analysis techniques for quantifying pore-scale structure and processes in subsurface porous medium systems. *Advances in Water Resources*, *51*, pp.217-246.

Youssef, S., Rosenberg, E., Gland, N., Bekri, S. and Vizika, O., 2007. Quantitative 3D characterisation of the pore space of real rocks: improved μ-CT resolution and pore extraction methodology. *Int. Sym. of the Society of Core Analysts*.

Zolensky, M., Mikouchi, T., Fries, M., Bodnar, R., Jenniskens, P., Yin, Q.Z., Hagiya, K., Ohsumi, K., Komatsu, M., Colbert, M. and Hanna, R., 2014. Mineralogy and petrography of C asteroid regolith: The Sutter's Mill CM meteorite. *Meteoritics & Planetary Science*, *49*(11), pp.1997-2016.